CALSPAN UB RESEARCH CENTER

(NASA-CR-190164) HEAT TRANSFER AND PRESSURE MEASUREMENTS AND COMPARISON WITH PREDICTION FOR THE SSME TWO-STAGE TURBINE Interim Report (Calspan-Buffalo Univ. Research Center) 120 p

N92-22590

CSCL 21H G3/20

Unclas
0079970

HEAT TRANSFER AND PRESSURE MEASUREMENTS AND COMPARISON WITH PREDICTION FOR THE SSME TWO-STAGE TURBINE

By
M.G. Dunn and J. Kim
Calspan-UB Research Center
Buffalo, NY 14225

CUBRC Report No. 6401

March, 1992

Prepared for:

NASA LEWIS RESEARCH CENTER
21000 BROOKPARK RD.
CLEVELAND, OH 44135

ABSTRACT

Time averaged Stanton number and surface-pressure distributions are reported for the first-stage vane row, the first stage blade row, and the second stage vane row of the Rocketdyne Space Shuttle Main Engine two-stage fuel-side turbine. Unsteady pressure envelope measurements for the first blade are also reported. These measurements were made at 10%, 50%, and 90% span on both the pressure and suction surfaces of the first stage components. Additional Stanton number measurements were made on the first stage blade platform, blade tip, and shroud, and at 50% span on the second vane. A shock tube was used as a short duration source of heated and pressurized air to which the turbine was subjected. Platinum thin-film heat flux gages were used to obtain the heat-flux measurements, while miniature silicon-diaphragm flush-mounted pressure transducers were used to obtain the pressure measurements. The first stage vane Stanton number distributions are compared with predictions obtained using a version of STAN5 and a quasi-3D Navier-Stokes solution. This same quasi-3D N-S code was also used to obtain predictions for the first blade and the second vane.

ACKNOWLEDGEMENTS

This research was performed by the Calspan UB Research Center under support of the NASA Lewis Research Center, Cleveland, OH, Grant No. NAG3-581. The authors gratefully acknowledge the contributions made to the success of this program by the contract monitors K.C. Civinskas and Dr. R. Gaugler of the NASA Lewis Research Center. Thanks are also extended to R. J. Boyle and K.C. Civinskas for performing the predictions to the data upon which we heavily depended. This work would have not been possible without the contributions of the many Calspan engineers and technicians, especially John R. Moselle, Robert M. Meyer, Shirley J. Sweet, Jeffrey L. Barton, and Robert M. Field.

TABLE OF CONTENTS

LIST OF FIGURES

LIST OF TABLES

SECTION 1

INTRODUCTION

The results described in this document are a summary of the work performed under support of NASA Lewis Research Center Grant No. NAG3-581. This program was initiated in 1986 with the purpose of providing fundamental data that could be used to validate predictive codes that would be used to predict the heat transfer distributions and pressure loadings for the SSME fuel-side turbopump. Prior to the time that a full scale pump became available, the Garrett TFE 731-2HP turbine was used to develop techniques for obtaining the basic data of interest and for investigating the applicability of various predictive techniques. The results of this effort have been reported in Dunn, 1986, Dunn et al., 1986, Rae et al., 1988, Taulbee, Tran, and Dunn, 1988, Dunn, et al., 1989, Dunn, 1990, Tran and Taulbee, 1991, and George, Rae and Woodward, 1991. Once the SSME turbine stage became available, all attention focused on that machine with the purpose of: (a) providing experimental information for code validation to the turbopump consortium, and (b) to provide comparison data for a blowdown test rig at Marshall Space Flight Center which uses the same multi-stage turbine. The program was structured so that time-averaged, time-resolved, and phase-averaged data were to be obtained.

The results of several previous measurement programs that utilized many of the same diagnostic techniques as used here, but for different turbine stages, have been reported in Dunn and Stoddard, 1979 (Garrett TFE 731-2); Dunn and Hause, 1982 (Garrett TFE 731-2); Dunn, Rae, and Holt, 1984 (Garrett TFE 731-2); Dunn, Martin, and Stanek (Air Force LART), 1986; Dunn and Chupp, 1988 (Teledyne 702); Dunn and Chupp, 1989 (Teledyne 702); and Dunn, Bennett, Delaney, and Rao, 1990 (Allison Test Turbine). The short-duration facility used for the experiments reported here is the same one used to obtain the results reported in Dunn, Bennett, Delaney, and Rao, 1990.

The flow and heat transfer that occur in a turbine stage (or stages) represent one of the most complicated environments seen in any practical machine: the flow is unsteady (especially in the rotor), can be transonic, is generally three-dimensional, and is subjected to strong body forces. Despite these problems, satisfactory designs and expansions of operating envelopes have been achieved over the years due to the development of a sound analytical understanding of the flow and heat-transfer mechanics that define performance and to advances in materials and manufacturing processes. The analytical developments were made possible by a series of approximations, in which the level of detail retained in the modeling was sufficient to reveal important physical effects, while still allowing solutions to be found by available analytical/numerical methods.

The major milestones in the development of these methods have been the approximations that flow through each blade row is steady in coordinates fixed to the blades, that three-dimensionality can be handled by treating a series of two-dimensional flows in hub-to-shroud and blade-to-blade surfaces, and that the effects of viscosity can be estimated by non-interacting boundary-layer calculations and by loss models to account for secondary flow.

This technology base is surrounded by many analyses and numerical codes which can treat the flow on higher levels of approximation, and which are used from time to time to provide refined estimates of the flowfield and heat transfer, typically near a design point. Three-dimensional and unsteady flow effects are two areas where recently developed computational tools can provide useful information on the flow conditions, at least for the first stage of a multistage turbine. However, in the second and subsequent stages, these effects become more pronounced. The current state-of-the-art analyses can predict reasonably well the second stage vane pressure distribution but the predicted heat-flux levels on the second vane are not as good as desired as illustrated by Blair, Dring, and Joslyn, 1988. These analyses are probably not adequate for the second rotor row, but experimental data have not been generally available for comparison with the prediction.

The results presented in this report contribute heat-flux data for the midspan region of the second stage vane.

Unsteadiness and three-dimensionality are direct consequences of the interaction of blades moving through vane wakes and the impact of multiple blade rows. The environment associated with the SSME fuel side turbine lends itself to a multistage analysis. Until very recently, such an analysis would have been envisioned as a complete, time-accurate, fully three-dimensional description of the flowfield. Some first steps toward the calculation of such flows can be seen in the work of Rai, 1987 and Rai and Madavan, 1988, but it is clear that the computational costs of this approach could very quickly become prohibitive. An alternative to the Rai approach is that described by Hah, 1984. Metzger, Dunn, and Hah, 1990(a), used a flowfield defined using the calculated technique described in Hah, 1984 to perform turbine tip and shroud heat-transfer predictions for a Garrett TFE 731 HP turbine stage. These predictions were shown to compare favorable with experimental results. Another approach to the problem is the one proposed by Giles, 1988, which has also been applied to turbine data obtained in a short-duration facility for a Rolls-Royce turbine by Abhari, Guenette, Epstein, and Giles, 1991.

Another approach to the problem is that described by Rao and Delaney, 1990, which until the present time, has only been applied to a single stage. The method proposed by these authors solves the quasi-three-dimensional Euler/Navier-Stokes equations using the explicit hopscotch scheme. The full stage computation is performed by coupling vane and blade solutions on overlapping O-type grids. In Dunn, Bennett, Delaney, and Rao, 1990, comparisons are given between the predictions of Rao and Delaney, 1990, and experimental data that were obtained for a full-stage turbine using the same experimental techniques described in this paper. Comparisons are presented for the time-averaged surface pressure, the unsteady envelope of the surface pressure, and the phase-resolved surface pressure near the trailing edge of the vane and on the blade. The agreement between the predictions and the measurements was found to be very good.

Detailed heat-flux data of the same type mentioned above were also obtained and will be presented in the open literature in the near future.

An alternate approach that is receiving current attention is based on a formulation of the passage-averaged equations of Adamczyk, 1985 and 1986, which until now have been used only as an analysis tool. It is apparent that this technique holds promise as the basis of a design method whose physical basis is considerably advanced beyond the current state of the art, and whose numerical implementation is simple enough to achieve without the need for excessive hours of supercomputer time. The formulation of closure models necessary to exploit Adamczyk's formulation relies on the availability of time-resolved flowfield data. Some of this information can be obtained from the work of Dring and Joslyn, 1986, who have probed the flow field within and around a one-and-one-half stage rotating turbine.

Civinskas, Boyle, and McConnaughey, 1988, have previously presented an analysis of the first stage blade of the turbine used here. The predictions presented here are a continuation of that work. The Navier-Stokes analysis of heat transfer was done using a modified version of the quasi-3D thin layer code developed by Chima, 1986. The modifications are explained in Boyle, 1991. An additional change for the purposes of this paper has been to incorporate the transition model of Mayle, 1991 for the first vane and the intermittency model of Mayle and Dullenkopf, 1989, 1990, for the first blade and the second vane. In addition to the quasi-3D Navier-Stokes analysis, the STAN5 (Crawford and Kays, 1976) boundary layer analysis, as modified by Gaugler, 1981 was used. Both the Navier-Stokes and boundary analyses used the MERIDL hub-to-shroud analysis of Katsanis and McNally, 1977 to determine the stream tube variation at appropriate spanwise locations. The edge conditions for the STAN5 boundary layer analysis were obtained using the TSONIC analysis of Katsanis, 1969.

The rotor blade tip of a gas turbine engine moves in close proximity to the outer stationary shroud. Typically, the gap between blade tip and shroud is kept as small as possible in order to reduce losses. Active control of the gap is difficult and, even under the best of conditions, does not reduce the gap to zero. It would not be desirable to reduce this tip gap too much because during transient engine excursions a rotor rub might occur which may be more detrimental to the engine than the tip losses are to the performance. It is common practice for the turbine tip gap to be on the order of 1% to 1.5% of the blade height. The leakage flow is driven by the higher pressure on the blade pressure surface forcing fluid through the gap towards the suction surface and can result in relatively large heat transfer levels on the blade tip and on the blade suction surface in the vicinity of 90% to 100% span near the trailing edge. Heat transfer levels on the stationary shroud are also relatively large by comparison to blade midspan levels, but not as large as on the tip.

Many authors have studied the flow in the tip gap region: e.g., Allen and Kofskey, 1955; Booth, Dodge and Hepworth, 1982; Mayle and Metzger, 1982; Wadia and Booth, 1982; Bindon, 1986; Moore and Tilson, 1988; and Metzger and Rued, 1989. Heat-transfer measurements on the moving blades and the stationary shroud have been made by Dunn, Rae and Holt, 1984(a) and 1984(b), Dunn, Martin and Stanek, 1986, Dunn, 1989 and by Epstein, 1985 on the stationary shroud. Metzger, Dunn and Hah, 1990 applied the results of a three-dimensional Navier-Stokes solution (technique described in Hah, 1984) obtained for the actual experimental conditions and turbine (Garrett TFE 731-2-HP) to exercise a simple model of the tip flow and estimate the local heat flux levels for comparison with the experimental results.

In the remainder of this report, Section 2 provides a description of the experimental technique, the turbine flow path, and the instrumentation. Section 3 presents the experimental results and a comparison with predictions. Section 4 presents an estimate of the turbine efficiency based on the measured heat-flux distributions and the flowpath measurements. The appendicies provide information regarding the airfoil coordinates, the instrumentation locations, along with a tabular listing of the data.

SECTION 2

DESCRIPTION OF THE EXPERIMENTAL TECHNIQUE, THE TURBINE FLOW PATH, AND THE INSTRUMENTATION

2.1 The Experimental Technique

The measurements are performed utilizing a shock-tunnel to produce a short-duration source of heated and pressurized gas that passes through the turbine. Air has been selected as the test gas for these experiments. A schematic of the experimental apparatus illustrating the shock tube, an expansion nozzle, a large dump tank and a device that houses the turbine stage and provides the flow path geometry is shown in Figure 2.1.1. The shock tube has a 0.47-m (18.5-inch) diameter by 12.2-m (40-feet) long driver tube and 0.47-m (18.5-inch) diameter by 18.3-m (60-feet) long driven tube. The driver tube was designed to be sufficiently long so that the wave system reflected from the endwall (at the left-hand end of the sketch) would not terminate the test time prematurely. At the flow conditions to be run for these measurements, the test time is very long for a shock tunnel facility being on the order of 40 milliseconds.

In order to initiate an experiment, the test section is evacuated while the driver, the double diaphragm section, and the driven tube are pressurized to predetermined values. Pressure values are selected to duplicate the design flow conditions. The flow function $\dot{w}\sqrt{\theta}/\delta$, wall-to-total temperature ratio (T_W/T_0), stage pressure ratios, and corrected speed are duplicated. The shock-tunnel facility has the advantage that the value of T_0 can be set at almost any desired value in the range of 800 °R to 3500 °R (Shock tubes obviously can operate at higher T_0 values than 3500 °R, but at the expense of test time. Test time is a parameter that one does not sacrifice easily), and the test gas can be selected to duplicate the desired specific heat ratio. The pressure ratio across the turbine is established by the throat area of the flow control nozzle located at the exit end of the device housing the turbine. It is desirable to locate this throat as close to the turbine exit

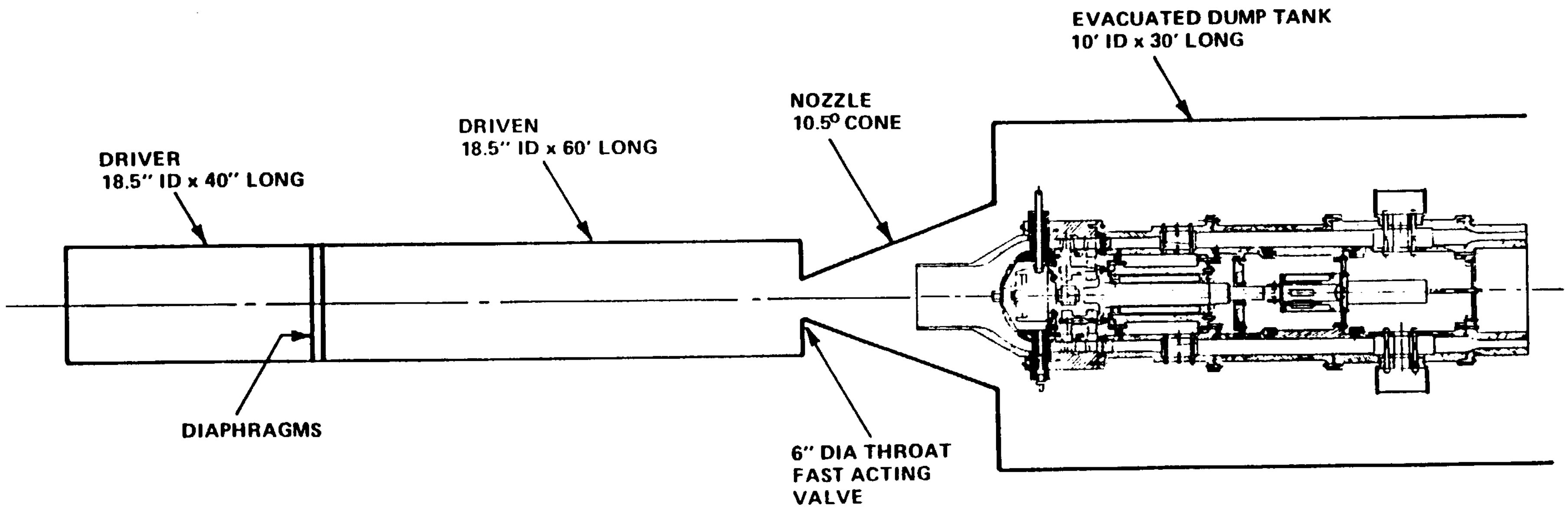

Figure 2.1.1 SKETCH OF THE SSME TURBINE STAGE LOCATED IN THE SHOCK-TUNNEL

as is practical to reduce the time required to fill the cavity between the rotor exit and the choke. The model (shown later in Figure 2.3.1) is currently being redesigned to move the throat closer to the turbine exit. Simple one-dimensional calculations provide a good first estimate of the necessary exit area. Another characteristic of this facility is that the total pressure (or the Reynolds number) at the entrance to the vane row can be changed by moving the inlet to the device housing the turbine axially in the expanding nozzle flow so as to intercept the flow at a different freestream Mach number. If this doesn't provide sufficient range, then the reflected-shock pressure can be increased or the total temperature can be decreased in order to increase the Reynolds number, which was the approach taken in these tests.

Figure 2.1.2 is a photograph of the facility illustrating many of the components described in the preceding paragraph. Figure 2.1.3 is a wave diagram for the shock tube. The gas that subsequently passes through the turbine has been processed by both the incident and the reflected shock shown in Figure 2.1.3. The reflected-shock reservoir gas is expanded in the primary nozzle which has the effect of increasing the flow velocity, decreasing the total pressure and maintaining the total temperature at the reservoir value. The device housing the turbine will not pass all of the weight flow available in the primary nozzle, so the inlet must be carefully located in order to avoid a hammer shock. That is, there must be sufficient flow area for a normal shock to establish outside the inlet and for the remainder of the flow not passed through the turbine to pass between the lip of the inlet and the nozzle wall. If the inlet is placed too far into the nozzle, the nozzle flow will be blocked and very large short-duration forces will be exerted on the device with potentially disastrous effects. The flow downstream of the inlet normal shock is subsonic at a pressure determined by the shock strength at the particular pick-off location in the expansion.

2.2 The SSME Turbine

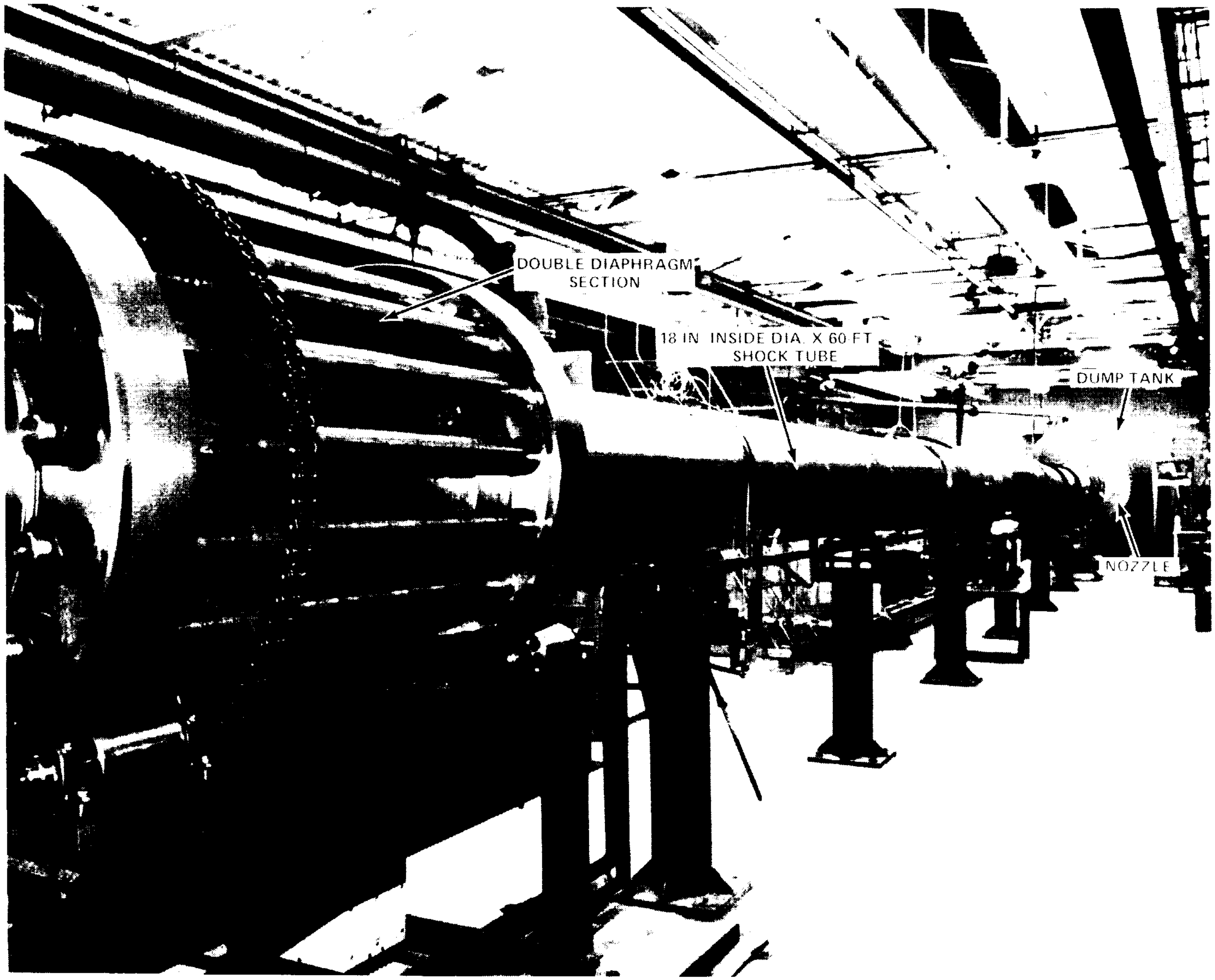

Figure 2.1.2 PHOTOGRAPH OF CALSPAN'S SHOCK-TUNNEL FACILITY FOR TURBINE RESEARCH

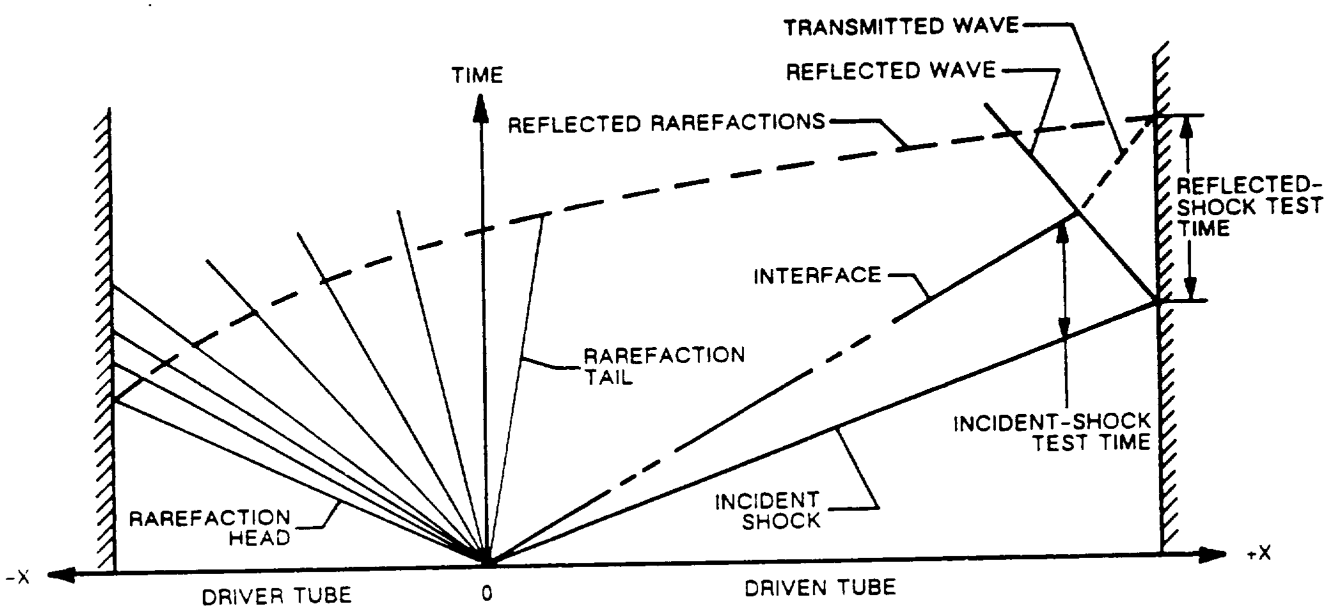

Figure 2.1.3 SKETCH OF A TYPICAL SHOCK-TUBE WAVE DIAGRAM

Photographs of the first stage vane row (41 vanes), the first stage rotor row (63 blades), and the second stage vane row (39 vanes) are shown on Figures 2.2.1-2.2.5. The second stage rotor (not shown) has 59 blades. The tip/shroud clearance for the first stage rotor at the design speed condition is ~0.015 inches or 1.6% of blade height. Figures 2.2.1 and 2.2.2 show photographs of the front and rear view of the first-stage vane row illustrating a cut-back (which was accounted for in the analysis to be described later) of the vane near the hub endwall trailing edge. It can be seen that the surface finish of the vane row is much smoother than it is for the blades. An enlarged photograph of the blade surface qualitatively illustrating the surface roughness on the blade is shown on Figure 2.2.6. The surface roughness for this blade has been measured* and a typical profilometer scan of the blade surface is given in Figure 2.2.7. The results shown in this figure suggest an rms roughness of about 150,000 Å which was used in the analysis of the heat-transfer data. Figures 2.2.4 and 2.2.5 are photographs of the second vane illustrating a surface finish comparable to the first vane and the absence of a cut-back at the trailing edge. The vane and blade coordinates are listed in the Appendix in section A.1.

2.3 The Turbine Flow Path

Figure 2.3.1 is a drawing of the turbine stage illustrating the extent to which the flowpath of the SSME hardware has been reproduced. The preburner dome and bolt, the 13 struts upstream of the first-stage vane, the 12 flow straighteners, and 6 struts downstream of the second rotor have been included. At the exit of the model is a flow choke which is used to control both the mass flow through the turbine as well as the turbine exit pressure. The choke area computed using a one-dimensional approximation to the flow yielded exit areas very close to those required.

* Roughness measurements were performed at the United Technologies Research Center and supplied to CUBRC courtesy of M. Blair. Figure 4(b) has been reproduced here with permission of M. Blair.

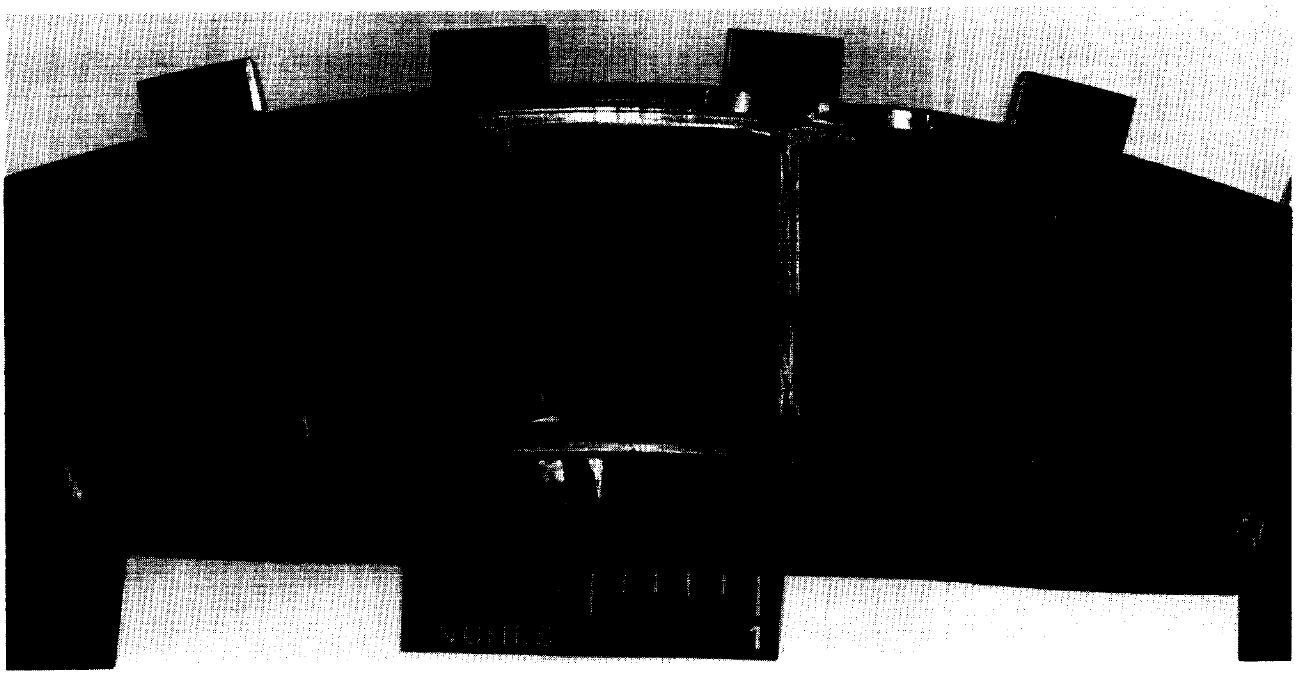

Figure 2.2.1 PHOTOGRAPH OF SSME FUEL-SIDE TURBINE FIRST STAGE VANE, FRONT VIEW

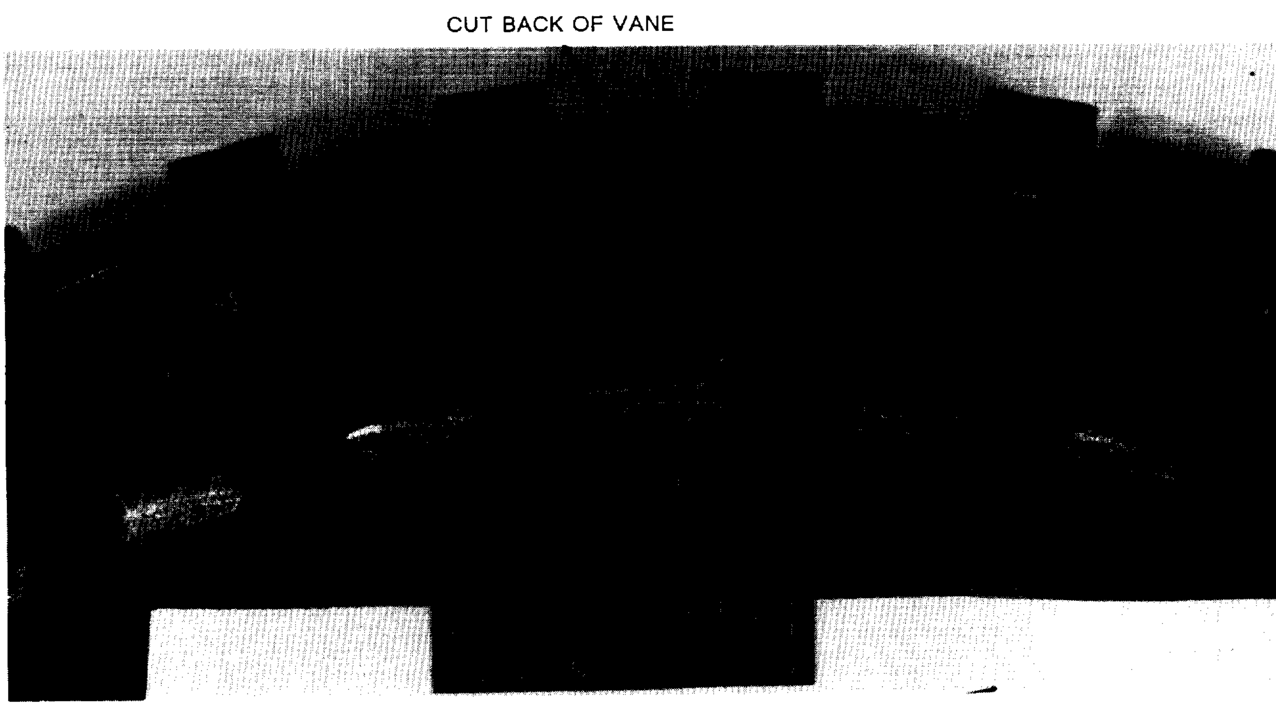

Figure 2.2.2 PHOTOGRAPH OF SSME FUEL-SIDE TURBINE FIRST STAGE VANE, REAR VIEW

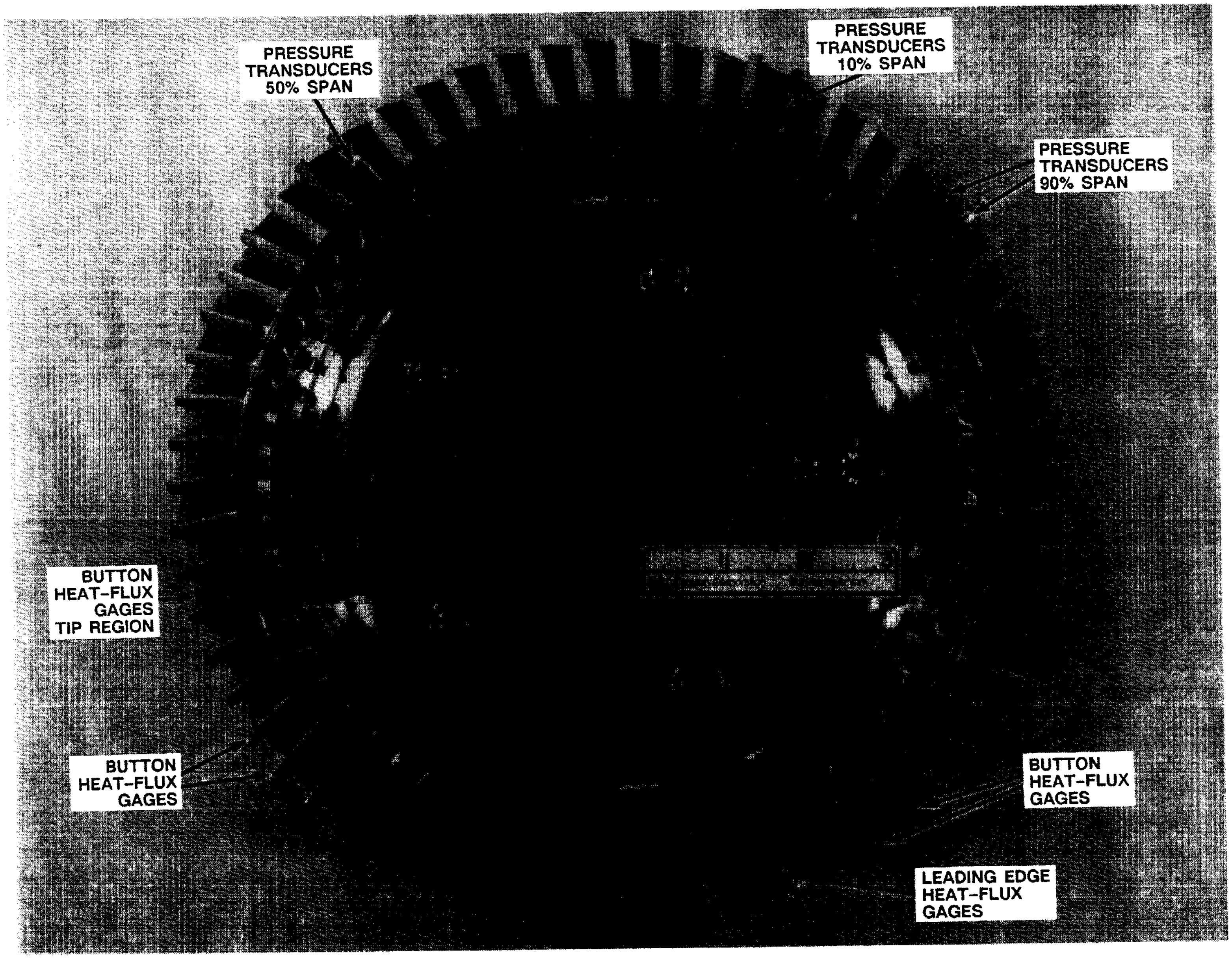

Figure 2.2.3 PHOTOGRAPH OF SSME FUEL-SIDE TURBINE FIRST STAGE ROTOR, FRONT VIEW

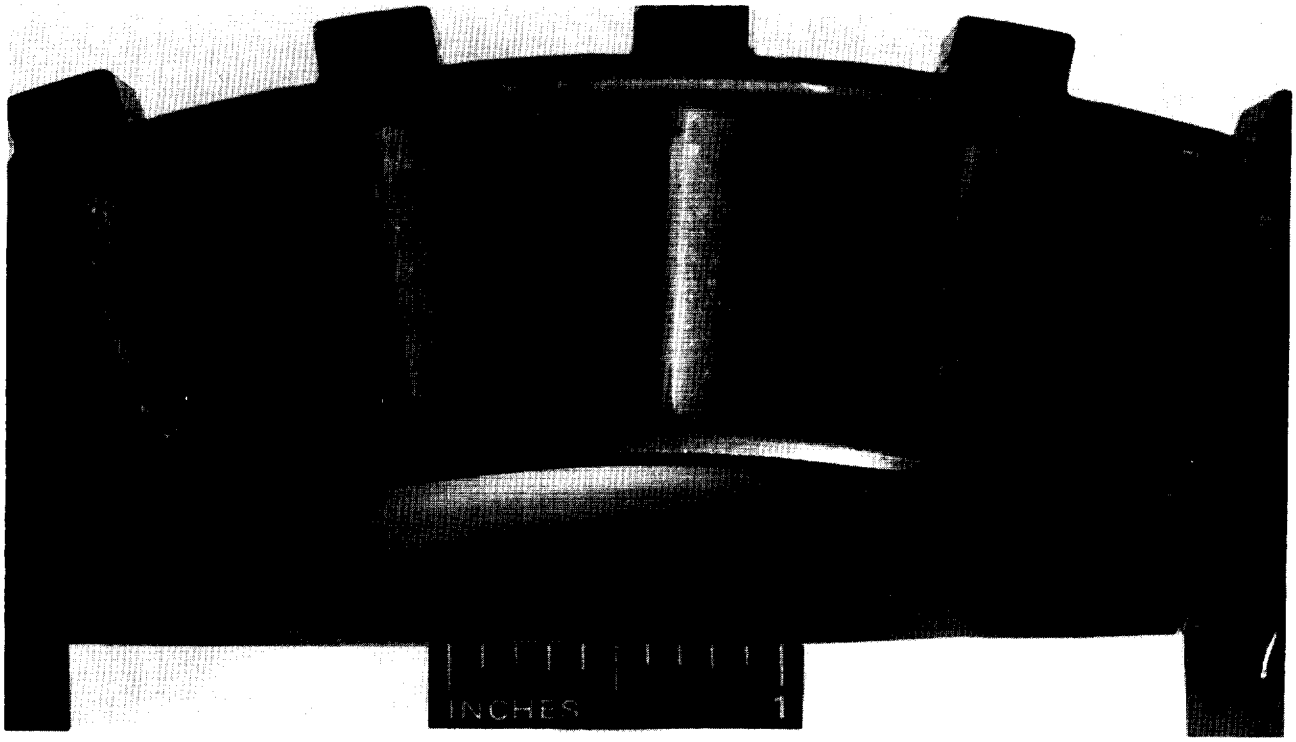

Figure 2.2.4 PHOTOGRAPH OF SSME FUEL-SIDE TURBINE SECOND STAGE VANE, FRONT VIEW

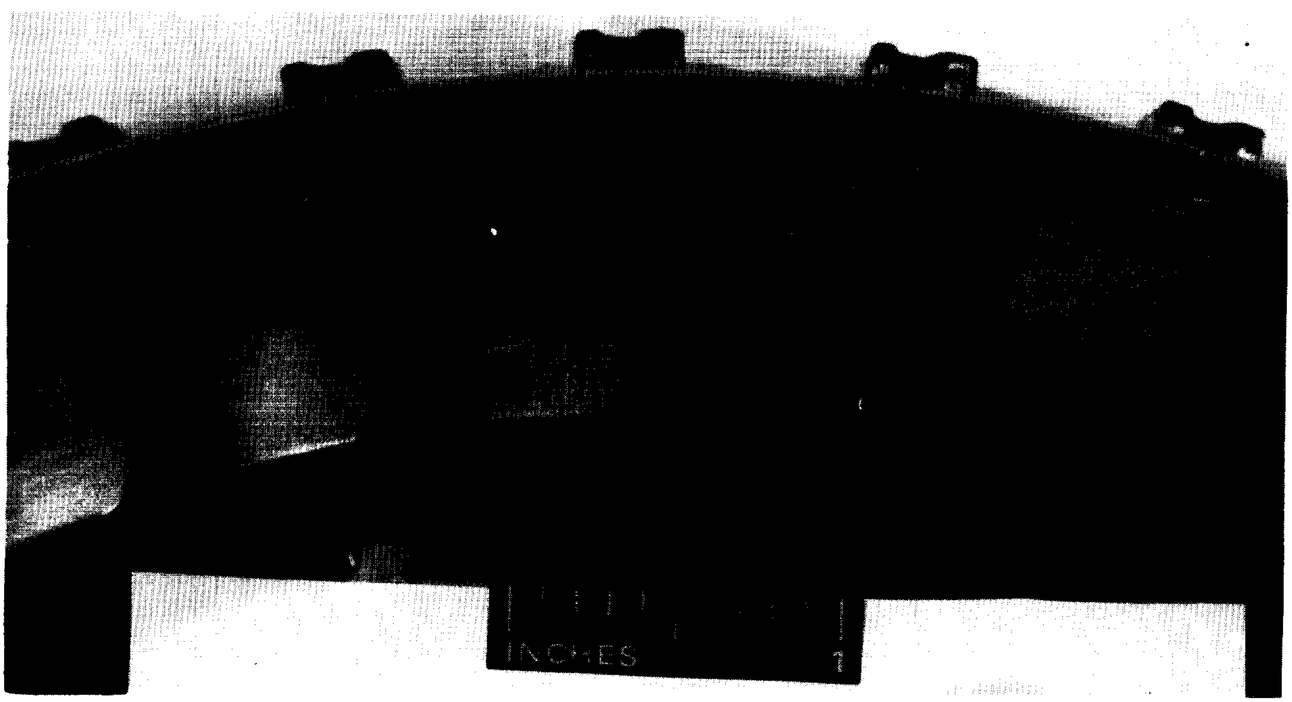

Figure 2.2.5 PHOTOGRAPH OF SSME FUEL-SIDE TURBINE SECOND STAGE VANE, REAR VIEW

Figure 2.2.6 ENLARGED PHOTOGRAPH OF FIRST BLADE SURFACE ROUGHNESS

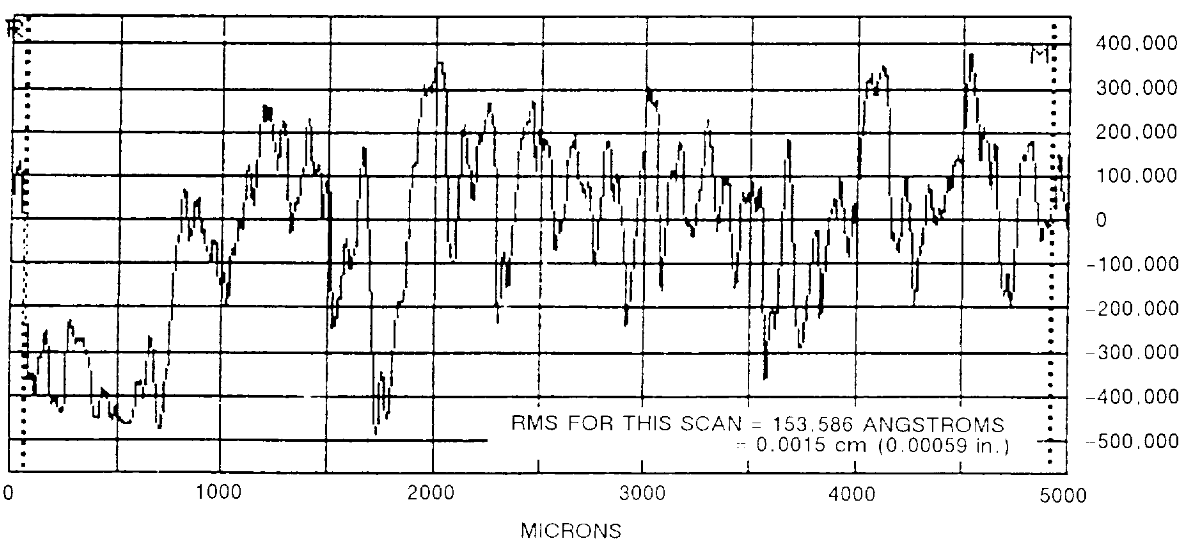

Figure 2.2.7 PROFILOMETER SCAN OF BLADE SURFACE

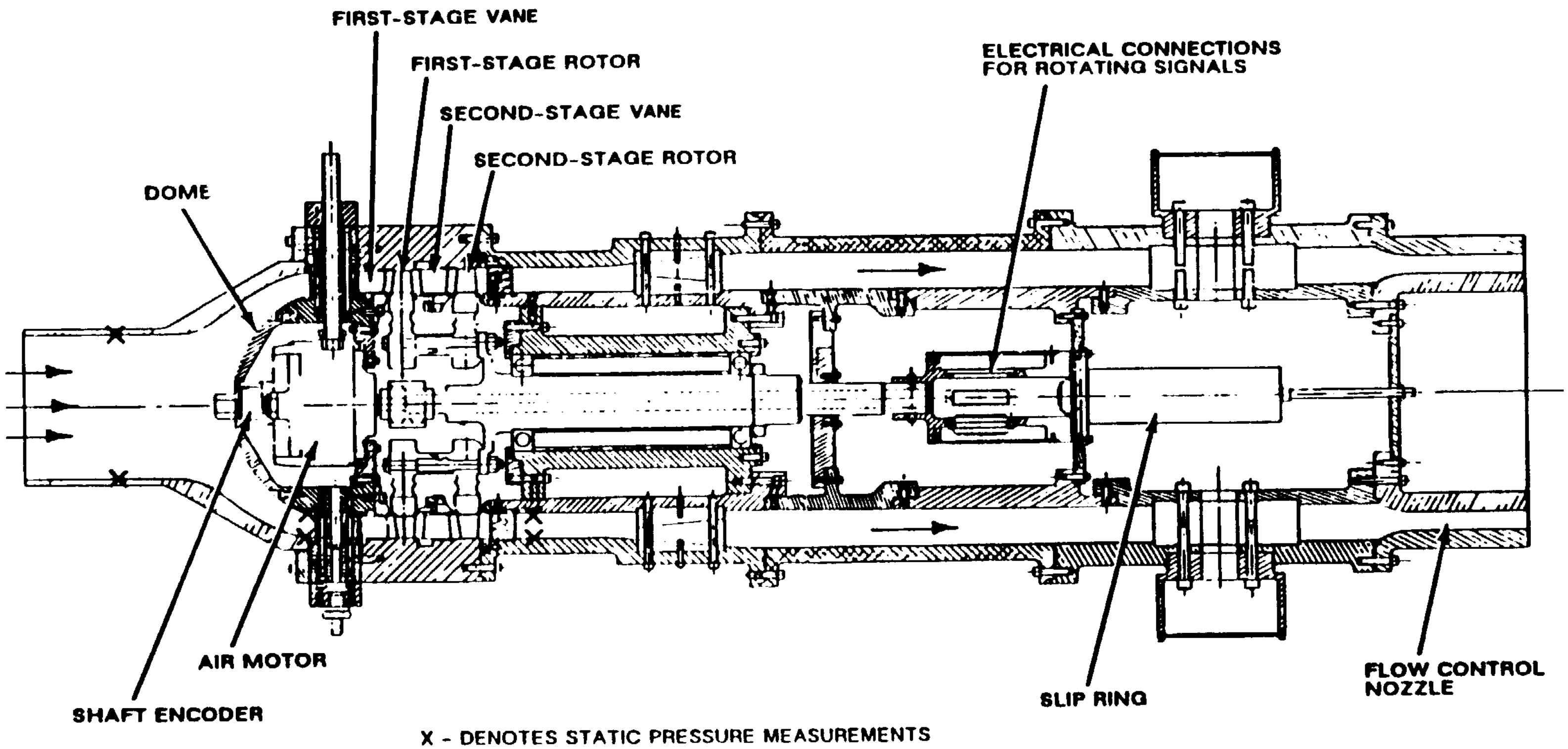

Figure 2.3.1 SKETCH OF DEVICE HOUSING SSME TURBINE STAGE

Mounted onto the forward end of the drive motor shaft is a 1000 pulse/revolution Hewlett Packard HEDS 5000 shaft encoder from which turbine speed and angular position is determined. This unit outputs a TTL pulse every 360°/1000=0.36° and a second TTL pulse once every revolution (the zero-crossing pulse). The shaft encoder was initially aligned such that the zero-crossing pulse occurred when the stagnation point of the first stage rotor blade containing the leading edge insert (heat-transfer) gage described in the next section was 12.2° CCW from TDC of the first stage vane. The pulses from the shaft encoder are used to trigger the data recording system. Since the turbine speed is not kept constant during the run, a 25 MHz timing pulse in the form of a ramp signal is fed into one channel of the high frequency data recorder to determine the arrival time of each encoder pulse. Mounted on the downstream end of the shaft is a 200 channel, freon/oil cooled, slip ring unit.

2.4 Heat-Flux Instrumentation

The heat-flux measurements were performed using thin-film resistance thermometers. These devices represent an old and very well established technology that was developed as part of the early hypersonics flow research work in the late 1950's for measurement of heat-flux distributions in short-duration facilities. The thin-film gages are made of platinum (~100 Å thick) and are hand painted on an insulating Pyrex (7740) substrate in the form of a strip that is approximately 1.02 x 10^{-4}-m (0.004-in) wide by about 5.08 x 10^{-4}-m (0.020-in) long. The response time of the elements is on the order of 10^{-8} s. The substrates containing the heat-flux gages are Epoxied within the base metal throughout the turbine stage. The substrate onto which the gage is painted can be made in many sizes and shapes.

Both button-type gages and the contoured leading-edge inserts were used for this work. The first stage vane and blade row were instrumented using both types of instrumentation along the 10%, 50%, and 90% span locations. Some gages were installed in the first stage blade shroud, blade platform, and blade tip. The second stage vane had button gages only along the 50% span. The locations of the heat transfer instrumentation are summarized in the Appendix in section A.2. Figure 2.4.1 is a photograph of a rotor blade that has been instrumented with button-types gages and Figure 2.4.2 is a photograph of a blade containing a contoured leading-edge insert. Each of the gages has two lead wires. The wires from the gages on the rotor are routed through the hollow shaft to the slip-ring unit.

2.5 Pressure Instrumentation

Measurements were also obtained using miniature silicon diaphragm pressure transducers located on the first-stage vane and the first-stage blade. The particular gages being used are Kulite Model LQ-062-600A with an active pressure area of 0.64 mm by 0.64 mm, and a frequency response of about 100 kHz in the installed configuration. Twenty-eight pressure transducers were installed on the vanes and twenty-four were installed on the blades. The pressure transducers were placed at 10%, 50%, and 90% span on the first vane and blade stages, and were distributed over several different vanes and blades so as to not disturb the integrity of the surface. No pressure transducers were installed in the second stage vane. The location of the surface mounted pressure transducers are summarized in the Appendix in section A.2. Figure 2.5.1 is a photograph of several of these transducers located at 10% span on the suction surface of the blade. Each of these transducers has four leads--two power leads and two output leads. The wires from the gages on the rotor are routed through the hollow shaft to the slip-ring unit.

Flowpath static pressure was measured on the outer wall of the turbine model at the inlet and exit to the turbine stages and between each blade row. The upstream static pressure was nearly equal to the upstream total pressure because the inlet Mach number was low (on the order of 0.1). The inlet Mach number was calculated and the inlet total

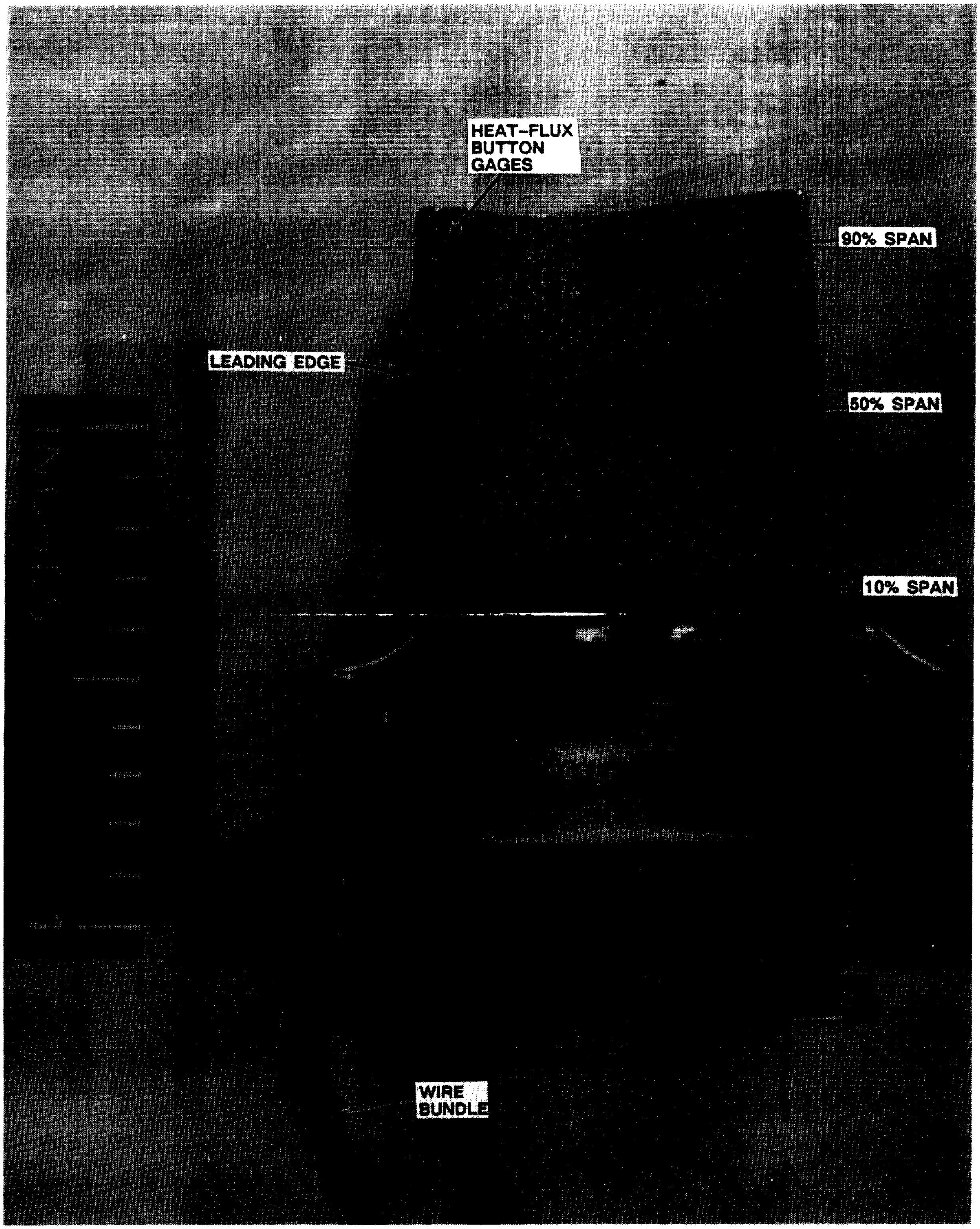

Figure 2.4.1 BUTTON-TYPE HEAT-FLUX GAGES ON FIRST-STAGE BLADE PRESSURE SURFACE

ORIGINAL PAGE
BLACK AND WHITE PHOTOGRAPH

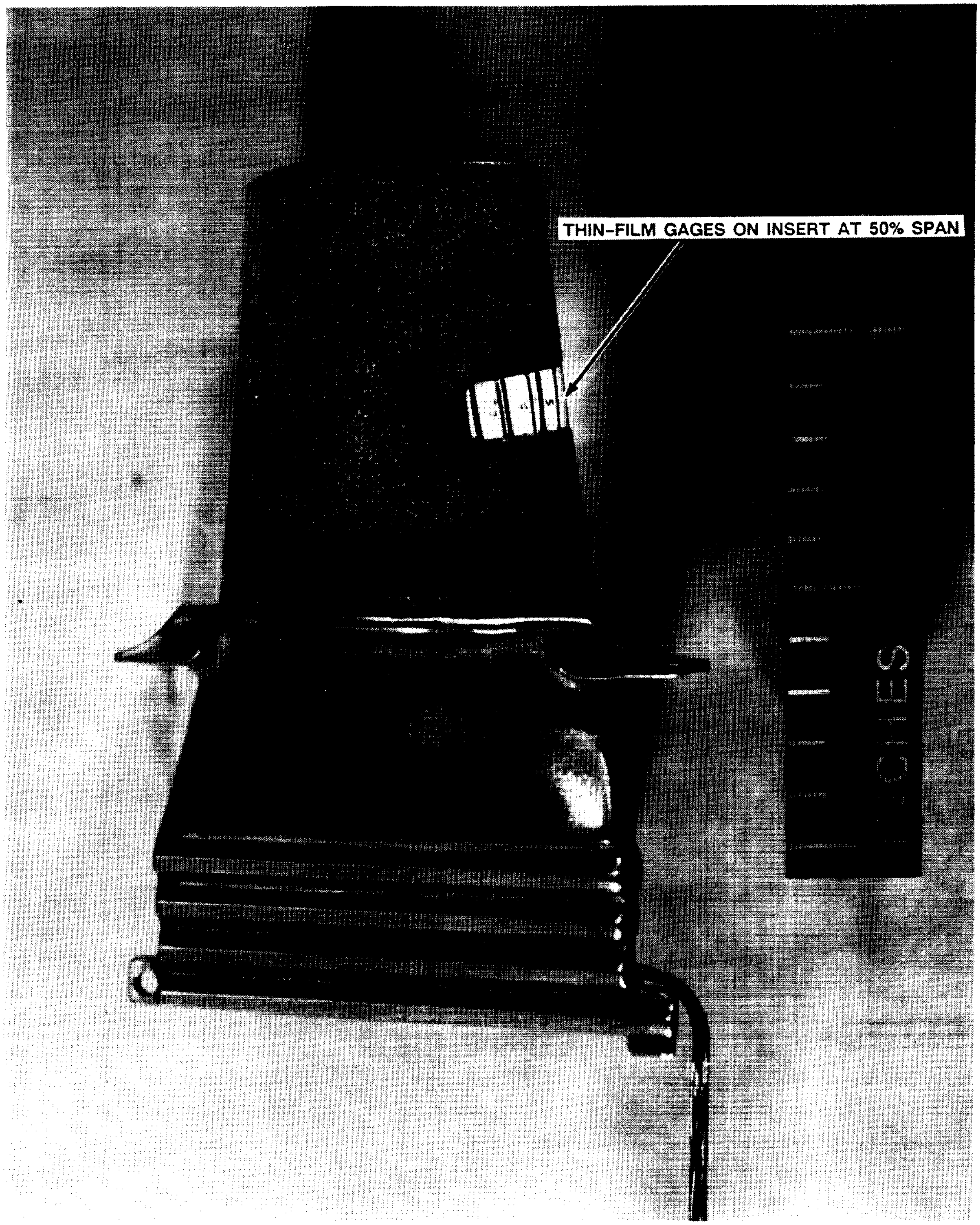

Figure 2.4.2 PHOTOGRAPH OF LEADING-EDGE INSERT HEAT-FLUX GAGES ON FIRST-STAGE BLADE

ORIGINAL PAGE
BLACK AND WHITE PHOTOGRAPH

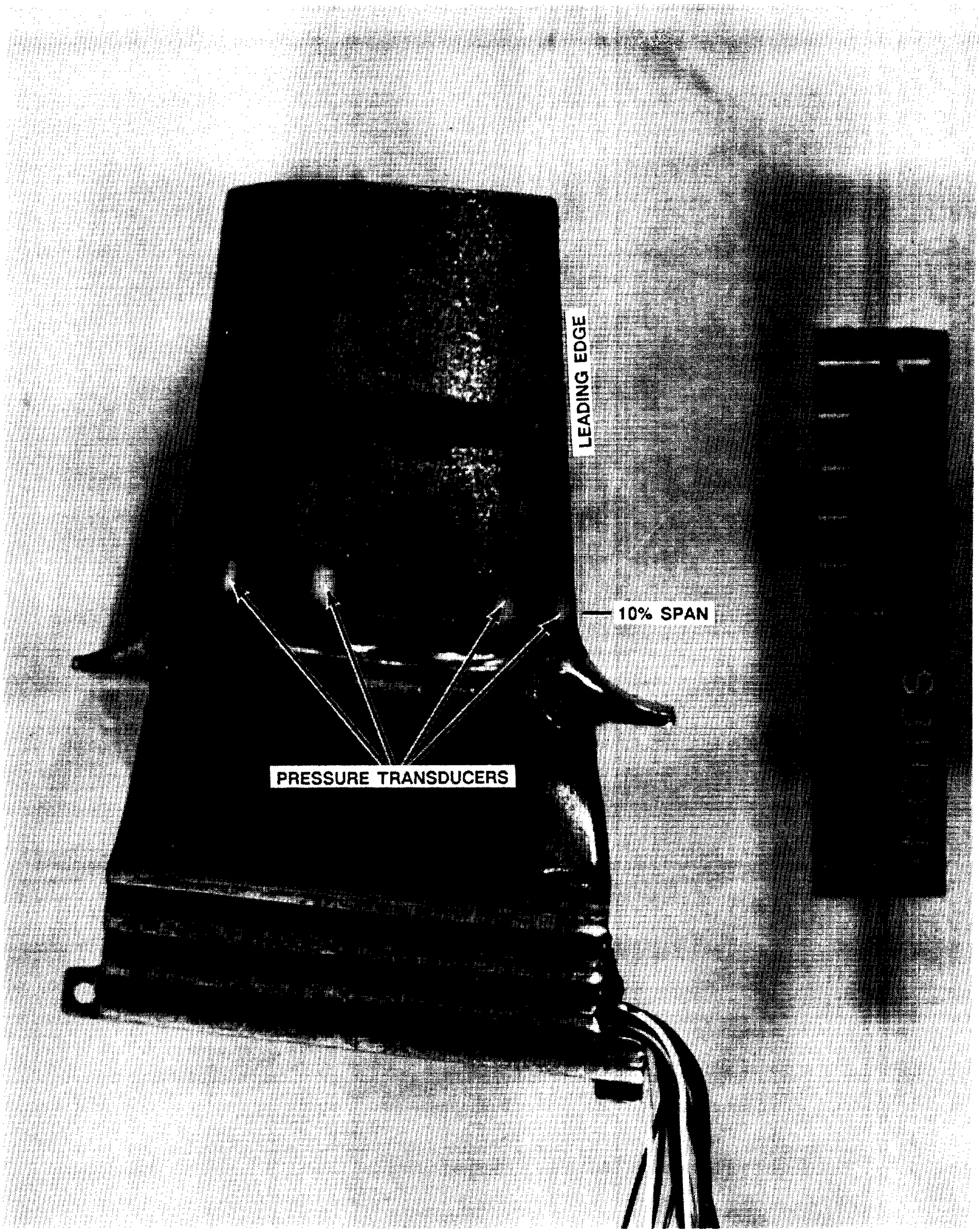

Figure 2.5.1 PHOTOGRAPH OF PRESSURE TRANSDUCERS AT 10% SPAN ON FIRST-STAGE BLADE SURFACE

pressure was obtained from the isentropic flow relationship. Total pressure was also measured in the passage downstream of the second rotor using two rakes of transducers.

2.6 High Speed Data Acquisition

An attempt was made to obtain time resolved data for selected heat transfer and pressure gages on the first stage rotor using a bank of 24 programmable, high-speed data recording units (Datalab DL6010 and DL6020). These units were configured so that a sample was recorded whenever a pulse was output by the shaft encoder, i.e., once every 0.36°. A separate timer box was used to measure the recording time after trigger. The data obtained using this bank of high-speed recorders were, however, contaminated with noise that was inadvertently introduced into the system. The unsteady pressure and heat transfer envelopes therefore could not be obtained. This problem will be rectified by start of the second phase of this program.

SECTION 3

EXPERIMENTAL RESULTS AND COMPARISON WITH PREDICTIONS

A total of thirteen runs were made during which several model configurations were used. Of these thirteen runs and different model configurations, eight runs produced data that could be used for the intentions of this research program. Some of the runs that did not produce useable data were lost because of shock-tube diaphragm failures. The remainder were lost in experimenting with the configuration of the model inlet duct. Table 1 summarizes the reflected shock conditions, the flow conditions at the turbine inlet, and the turbine speed for the eight runs to be discussed herein. Two shock tube conditions were run for these experiments; the first at a reflected-shock pressure and temperature of approximately 6.2×10^3 kPa (900 psia) and 544 K (980 °R), respectively, and the second at a reflected-shock pressure and temperature of approximately 10×10^3 kPa (1445 psia) and 602 K (1084 °R), respectively. For a given test condition, the range in reflected-shock pressure shown in Table 1 is the result of attempting to increase the test time by changing the relative amount of helium in the driver gas which also influences the incident shock Mach number and hence the reflected shock conditions. The two reflected-shock conditions result in first vane inlet Reynolds numbers (based on first vane chord) of approximately 1.4×10^5 and 2.5×10^5, respectively. Table 2(a) gives the measured upstream, interstage, and exit pressures, and Table 2(b) provides the pressure ratios for each of the vane and blade rows. The area of the downstream flow choke was changed so that data could be obtained at two values of stage pressure ratio, for each test condition. Measurements were obtained with the turbine speed set at 100%±1% of the design value or at approximately 103% of the design value. Limited data were obtained at off-design speed.

Run	$\dot{W}$ [lbm/s]	$\left.\frac{P_{T,in}}{P_{s,out}}\right\|_{stage}$	$P_{s,in}$ [psia]	Reflected shock pressure [psia]	Reflected shock temp. [°R]	$Re\|_{vc}$ ($x10^{-5}$)*	Actual speed [rpm]	% Design speed**
1	9.52	—	90	865	949	2.39	6100	68
5	5.59	1.66	46.6	900	995	1.39	9075	99
6	5.81	1.65	48.3	929	990	1.44	9468	103
7	10.2	1.48	86	1519	1112	3.00	9612	99
8	9.74	1.38	89	1442	1084	2.69	9690	101
11	10.0	1.42	98	1369	1057	2.40	9585	101
12	5.83	1.54	48.3	925	981	1.45	9380	103
13	5.51	1.54	45.3	878	970	1.38	9365	103

*Reynolds number based on vane chord and vane inlet conditions.

** $N_{corr} = 291.4 \text{ rpm} / \sqrt{°R}$

Table 1--Summary of flow parameters.

Run	P_t into 1st vane (psia)	P_s exiting 1st vane (psia)	P_s exiting 1st rotor (psia)	P_s exiting 2nd vane (psia)	P_s exiting 2nd rotor (psia)	P_t exiting 2nd rotor (psia)	$\left.\frac{P_{T,in}}{P_{s,out}}\right\|_{stage}$	$\left.\frac{P_{T,in}}{P_{T,out}}\right\|_{stage}$
1	90.0	78.5	67.6	—	—	—	—	—
5	47.1	40.4	34.3	30.5	28.3	29.1	1.66	1.62
6	48.9	43.0	36.4	32.5	29.7	30.4	1.65	1.61
7	86	77	70	63	58.3	59.9	1.49	1.45
8	89	82	75	68	64.3	64.4	1.40	1.40
11	98	90	79	71.5	69.0	67.5	1.44	1.47
12	48.8	43.3	37.3	34.1	31.7	32.2	1.54	1.52
13	45.8	40.3	34.7	32.0	29.7	30.2	1.54	1.52

Table 2a--Measured interstage pressures. Static pressure were measured at the outer shroud.

Run	First vane $\frac{P_{T,in}}{P_{s,out}}$	First stage $\frac{P_{T,in}}{P_{s,out}}$	Second vane $\frac{P_{s,in}}{P_{s,out}}$	Second rotor $\frac{P_{s,in}}{P_{s,out}}$
1	1.15	1.33	—	—
5	1.17	1.37	1.12	1.08
6	1.14	1.34	1.12	1.09
7	1.13	1.24	1.11	1.08
8	1.10	1.20	1.10	1.06
11	1.10	1.26	1.10	1.04
12	1.13	1.31	1.09	1.08
13	1.14	1.32	1.08	1.08

Table 2b--Component pressure ratios. Static pressures were measured at the outer shroud.

The Stanton number results presented here for both of the vane rows and the first blade row are based on conditions at the first vane inlet. The relationship used to evaluate the Stanton number was

$$St = \frac{\dot{q}(T)}{(\dot{W}/A)[H_o(T_o) - H_w(T)]} \quad (1)$$

The value of A used for this evaluation was 1.73 x 10^{-2} m^2 (0.186 ft^2), and corresponds to the annular area upstream of the first stage vane. In this formulation, the heat flux and the wall enthalpy are both evaluated at the same temperature, T. If the cold-wall heat flux, $\dot{q}(T_w)$, is desired, then it can be obtained by multiplying the given Stanton number by $(\dot{W}/A)[H_o(T_o) - H_w(T_w)]$. The greatest contributor to the uncertainty in Stanton number is the uncertainty in the weight flow, $\dot{W}$. For these experiments, the weight flow was found from an experimentally determined flow calibration curve supplied by NASA MSFC which plotted the flow function as a function of the total to static pressure ratio across the first stage nozzle. The uncertainty in the vane row pressure measurement translate into an uncertainty in the flow function and the weight flow. An uncertainty of approximately 10% in the weight flow was found. Assuming an uncertainty in the heat flux and temperature measurements to be 5%, the expected error in the Stanton numbers can be calculated using the methodology of Kline and McClintock, 1953 to be 12%.

3.1 First Vane and First Blade Surface Pressure Results

The measured surface pressure distributions on the first vane at 10%, 50%, and 90% span along with the predicted pressure distributions are presented on Figures 3.1.1-3.1.3. These results are presented for two stage pressure ratios, approximately 1.54 and 1.65. The agreement between the data and the prediction at all three spanwise locations is not particularly good. The cause of the disagreement is in large part attributable to the uncertainty in the pressure measurement. Prior to the initial experiment, the pressure

Figure 3.1.1--Pressure distribution at 10% span on first vane.

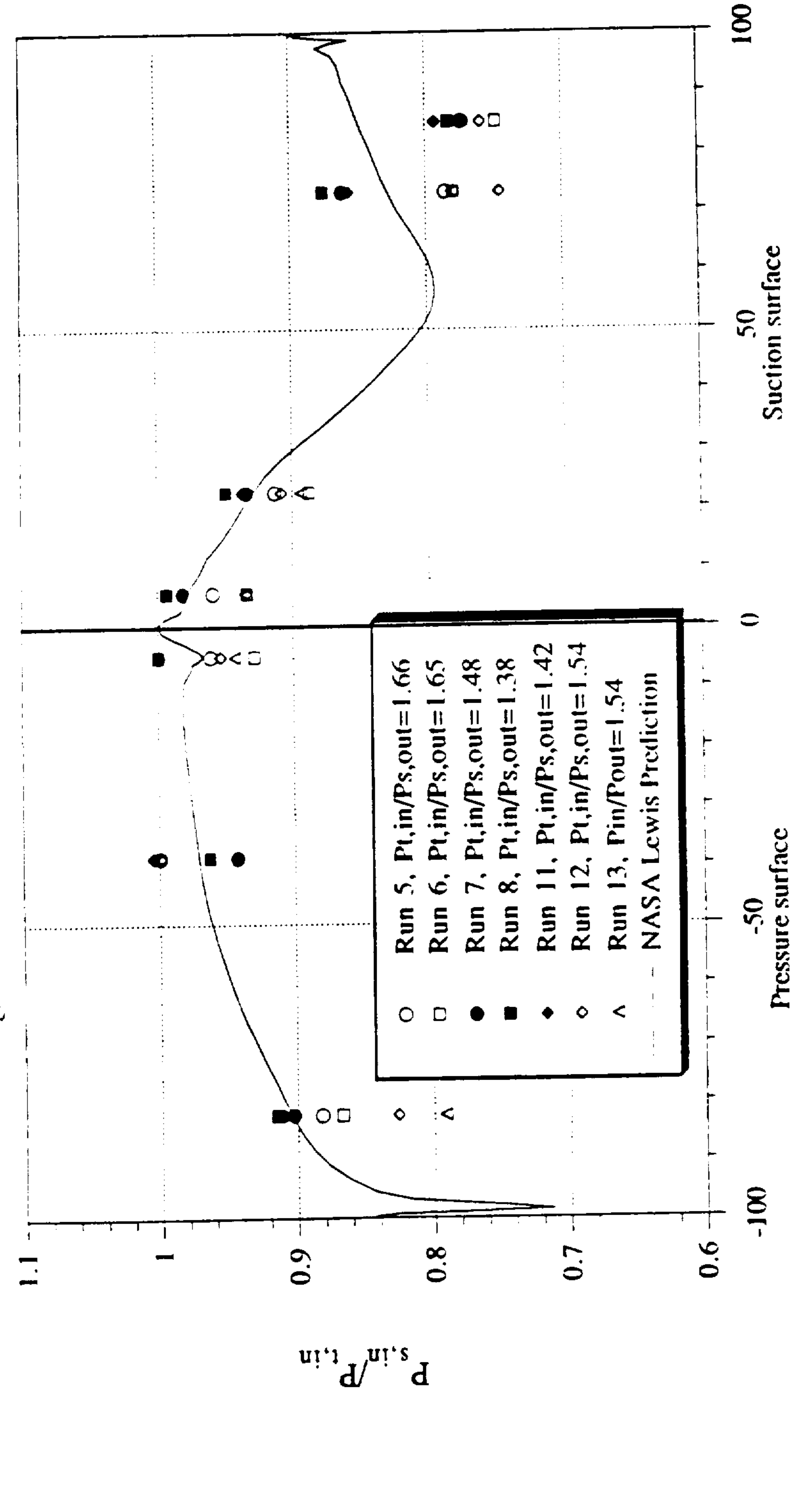

Figure 3.1.2--Pressure distribution at 50% span on first vane.

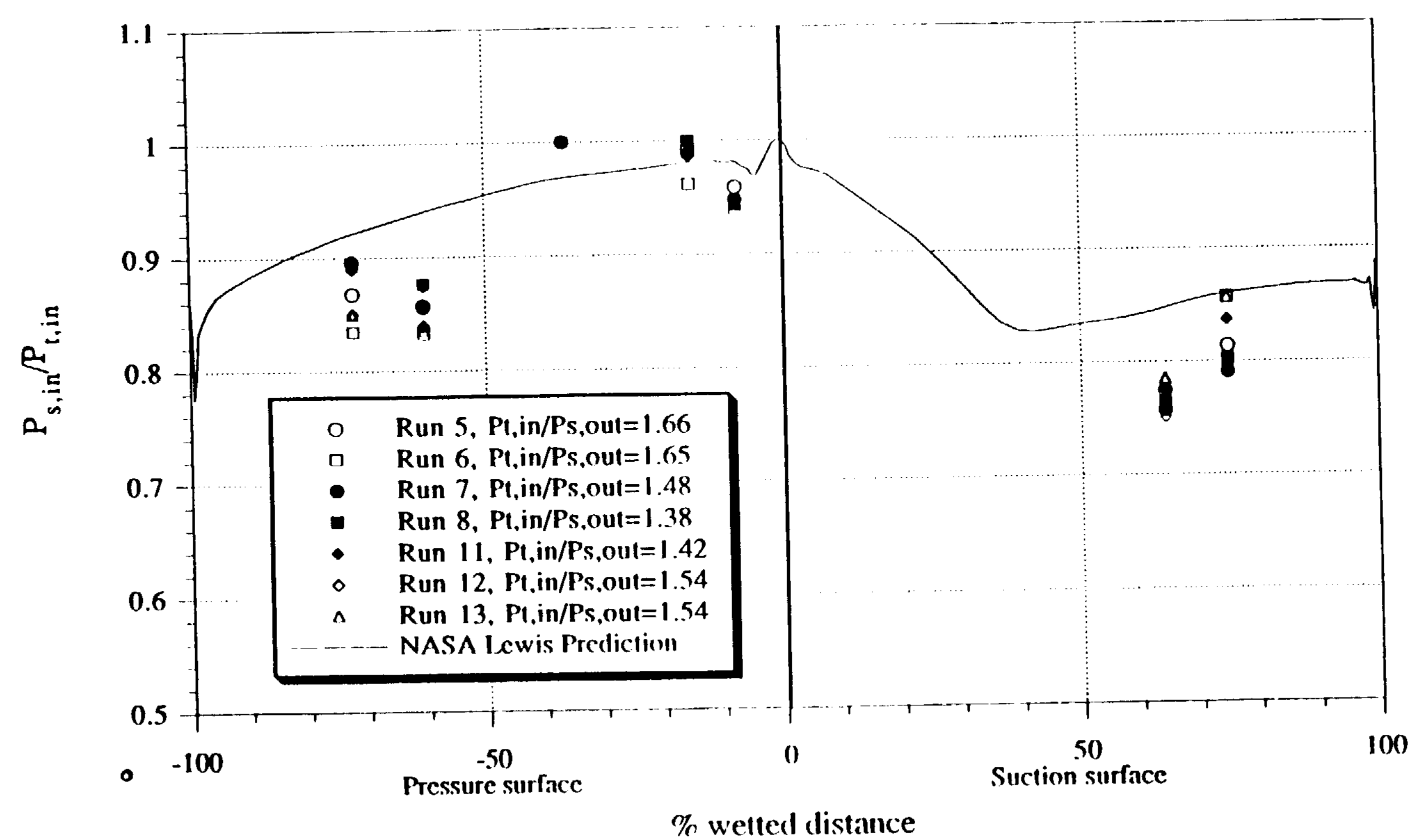

Figure 3.1.3--Pressure distribution at 90% span on first vane.

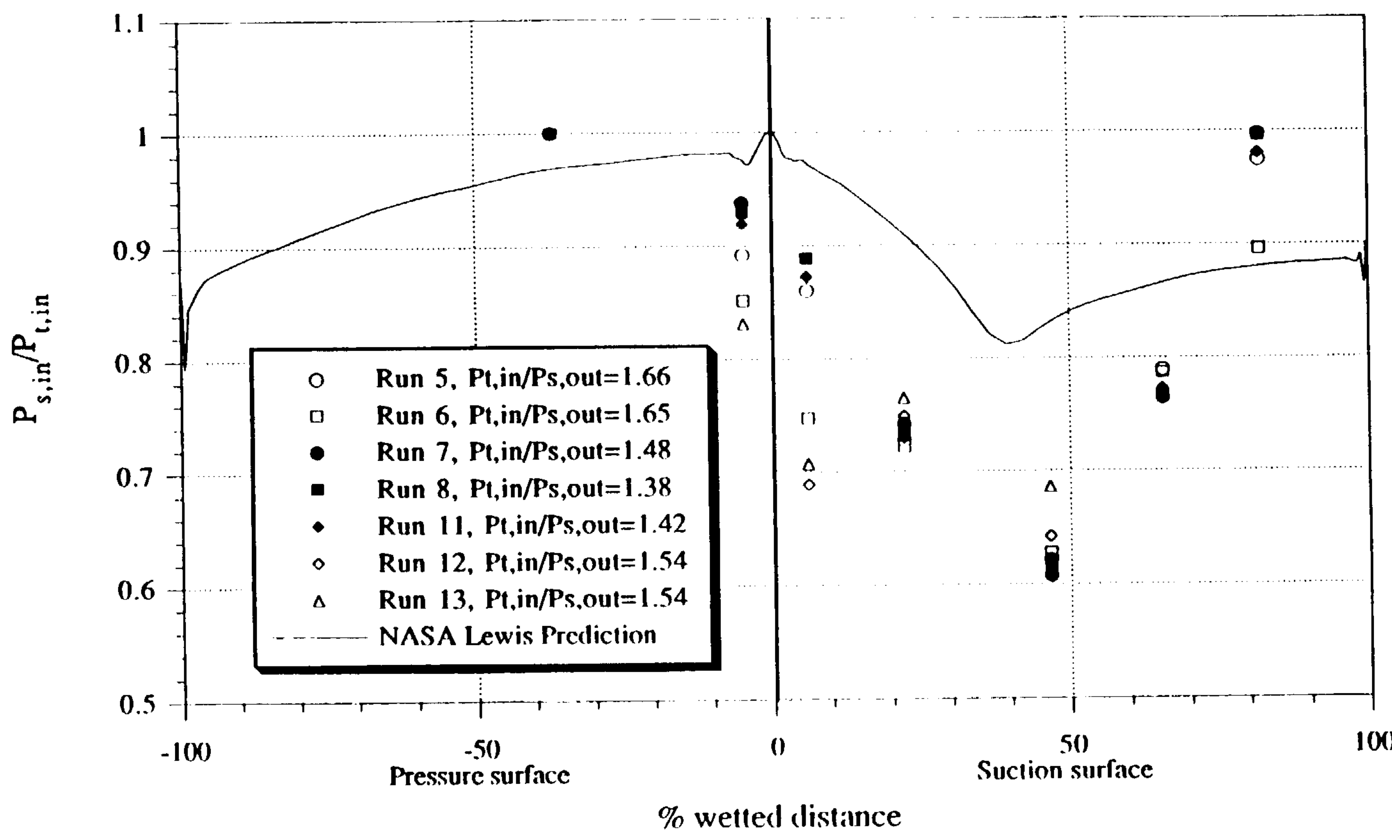

transducers were calibrated over the range from vacuum to 1.48 MPa (215 psia). During and after the experiments, they were calibrated again from vacuum to 0.655 MPa (95 psia). These latter calibrations were done by pressurizing the dump tank housing the turbine stage (see Figure 2.1.1). The pressure readings were recorded using the entire data recording system that is used during the experiment. For a given transducer, a linear fit was obtained for each data set over the pressure range of these experiments. The slope of the calibrations for most of the transducers was reproducible to within 3%. For a few others, the slope varied by as much as 5%. The pressure drop across the first vane row and the first blade row is relatively small for this turbine, being on the order of 10% to 15% of the inlet total pressure, which makes the uncertainty in the slope of the transducer calibration an important consideration. If a pressure measurement uncertainty of 3% due to variations in the slope of the calibration equation is assumed, along with a 2% uncertainty due to shock-tunnel reproducibility, the expected error in the normalized pressures (P/P_T) may be calculated using the methodology of Kline and McClintock (1953) to be 4.7%. The difficulty encountered here with the pressure measurements was unanticipated. A previous measurement program reported in Dunn, Bennett, Delaney, and Rao, 1990(a) demonstrated much better agreement between measurements and prediction. The calibration technique was the same in that work as used here. However, the transducers used in Dunn, et al., 1990a were 0 to 100 psia units while those used in this work were 0 to 600 psia units.

Figures 3.1.4, 3.1.5, and 3.1.6 present the measured surface pressure distributions on the first blade at the 10%, 50% and 90% locations at both values of stage pressure ratio. The same difficulties encountered with the vane pressure data described above were also encountered with the blade data. The disagreement between the measurements and the prediction are felt to be due to inaccuracy in the pressure measurement rather than problems with the prediction.

Figure 3.1.4--Pressure distribution at 10% span on first blade.

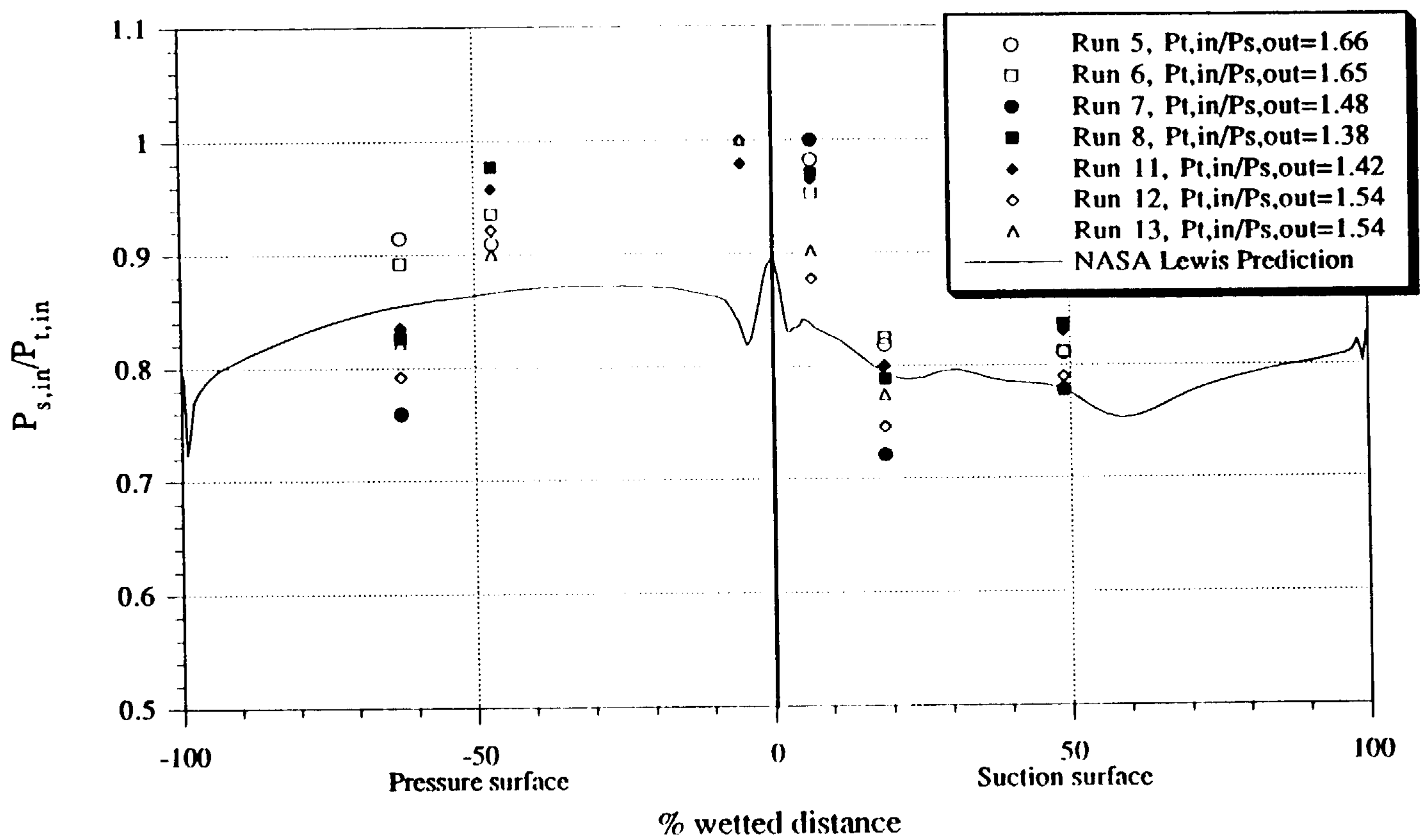

Figure 3.1.5--Pressure distribution at 50% span on first blade.

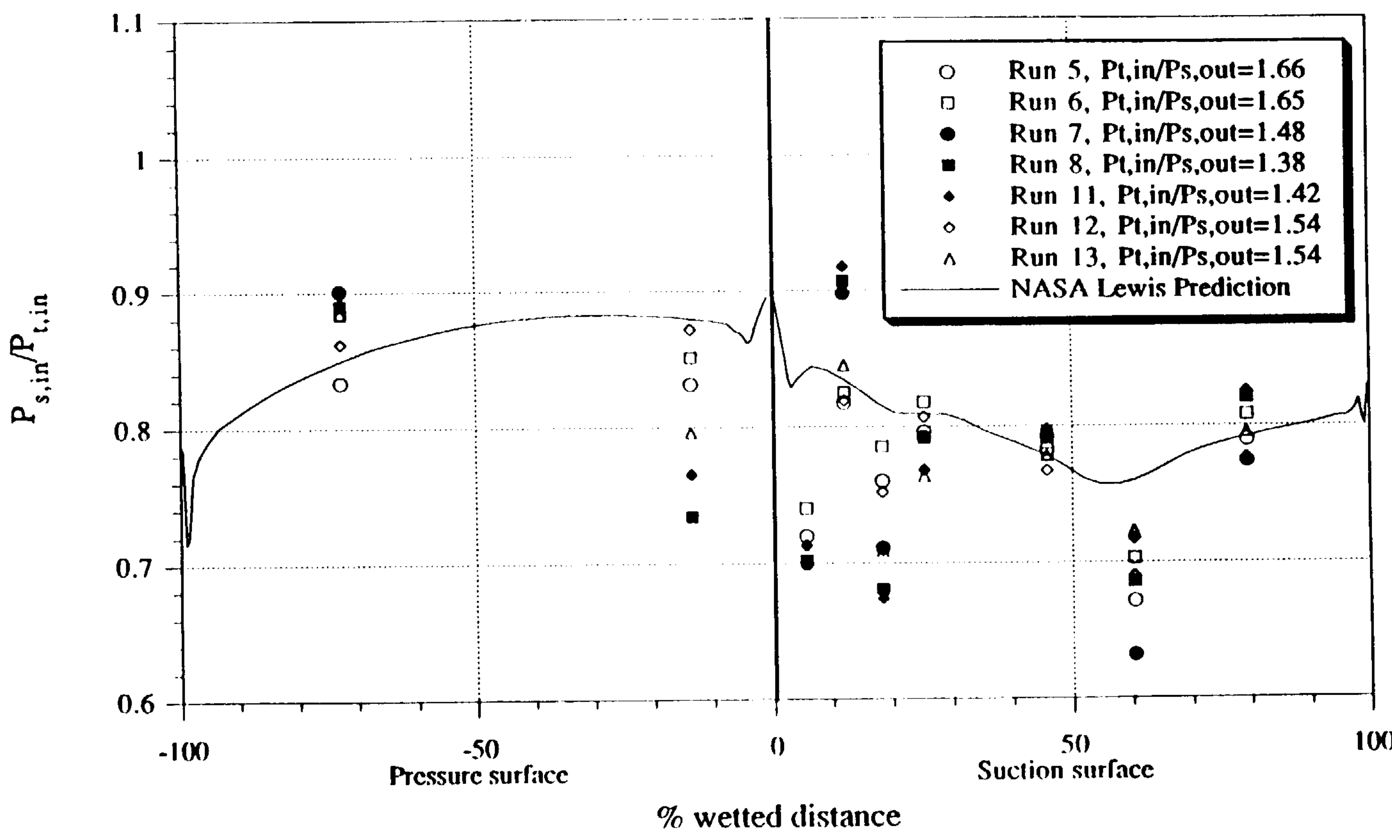

Figure 3.1.6--Pressure distribution at 90% span on first blade.

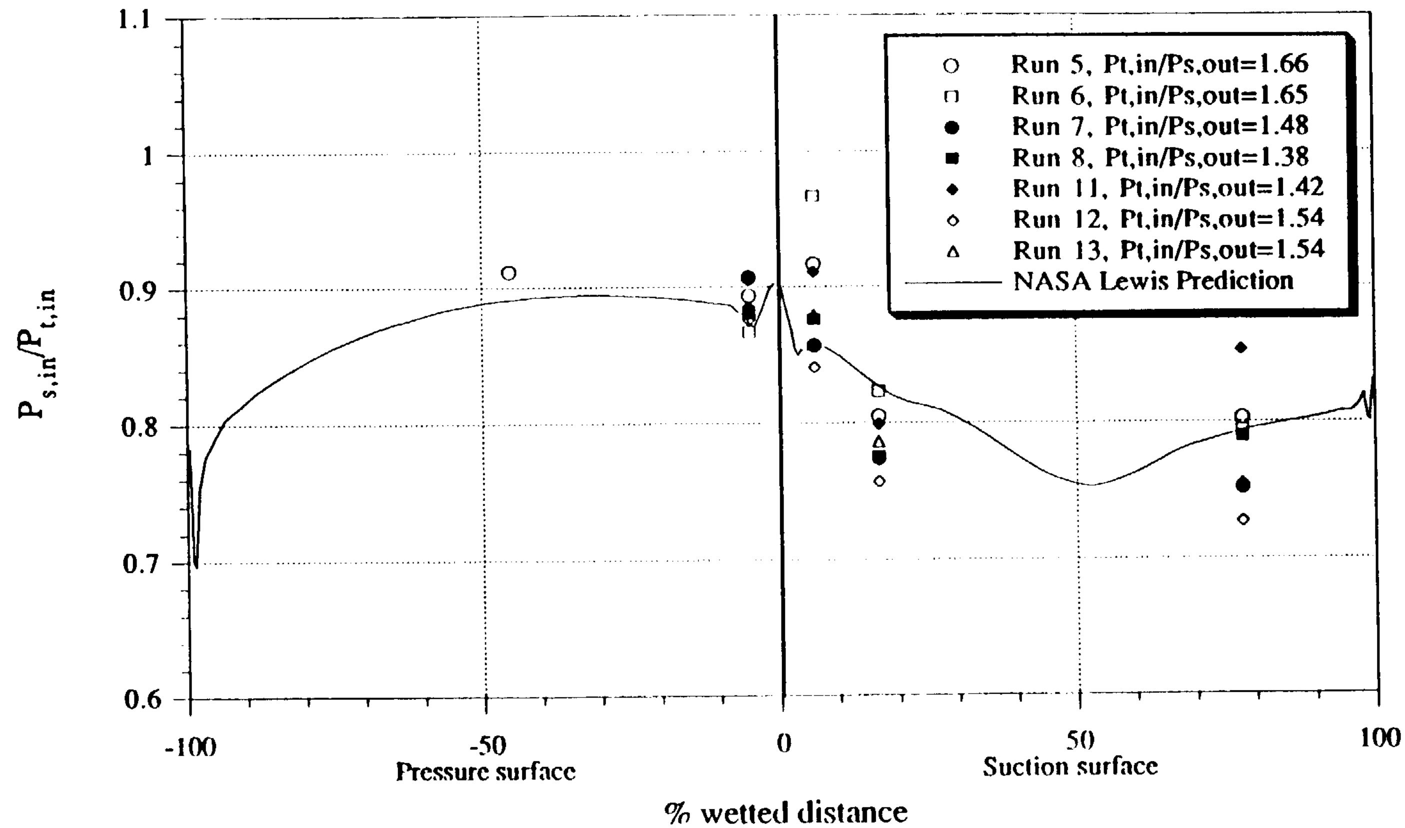

3.2 First Vane Surface Stanton Number Results

Figures 3.2.1 and 3.2.2 present the measured Stanton number distributions for the vane at 50% span for Reynolds numbers of 140,000 and 250,000, respectively. Figure 3.2.3 presents the Stanton number data for both Reynolds numbers at 10% span and Figure 3.2.4 presents data for both Reynolds numbers at 90% span. The low Reynolds number data were obtained at stage pressure ratios of 1.54 and 1.65 while the higher Reynolds number data were obtained at about 1.4 and 1.48. Inspection of the data suggests that the stage pressure ratio, in general, has little influence on the Stanton number distributions for the vane locations at which measurements were obtained.

The experimental results for the first vane presented in Figure 3.2.1 illustrate a rapid decrease in Stanton number on the suction surface from the stagnation point to about 15% wetted distance followed by a sharp increase near this location, then a peak at about 50% wetted distance. On the pressure surface, the data fall sharply from the stagnation point reaching a minimum at about 25% wetted distance, then increases steadily towards the trailing edge. This trend in the pressure surface data is consistent with that seen previously for the Garrett TFE731-2 HP turbine (Dunn, Rae and Holt, 1984), the Air Force LART (Dunn, Martin and Stanek, 1986) the Teledyne 702 turbine (Dunn and Chupp, 1988), as well as two other unpublished Calspan data sets. The peak Stanton number is shown to occur at the stagnation point and the maximum value reached on the suction and pressure surfaces are comparable with each other and equal to a little more than half of the stagnation value. Similar trends are seen at high Reynolds numbers (Figures 3.2.2) but with the minimums occurring closer to the stagnation point. Furthermore, the maximum in the suction surface data also occurs closer to the stagnation point.

Figure 3.2.1 also compares vane midspan experimental results with four predictions. Two of the predictions are for fully turbulent flow. The third and fourth predictions incorporate transition models. The two fully turbulent predictions were done

Figure 3.2.1. Stanton number distribution on first vane, 50% span, Re~140,000.

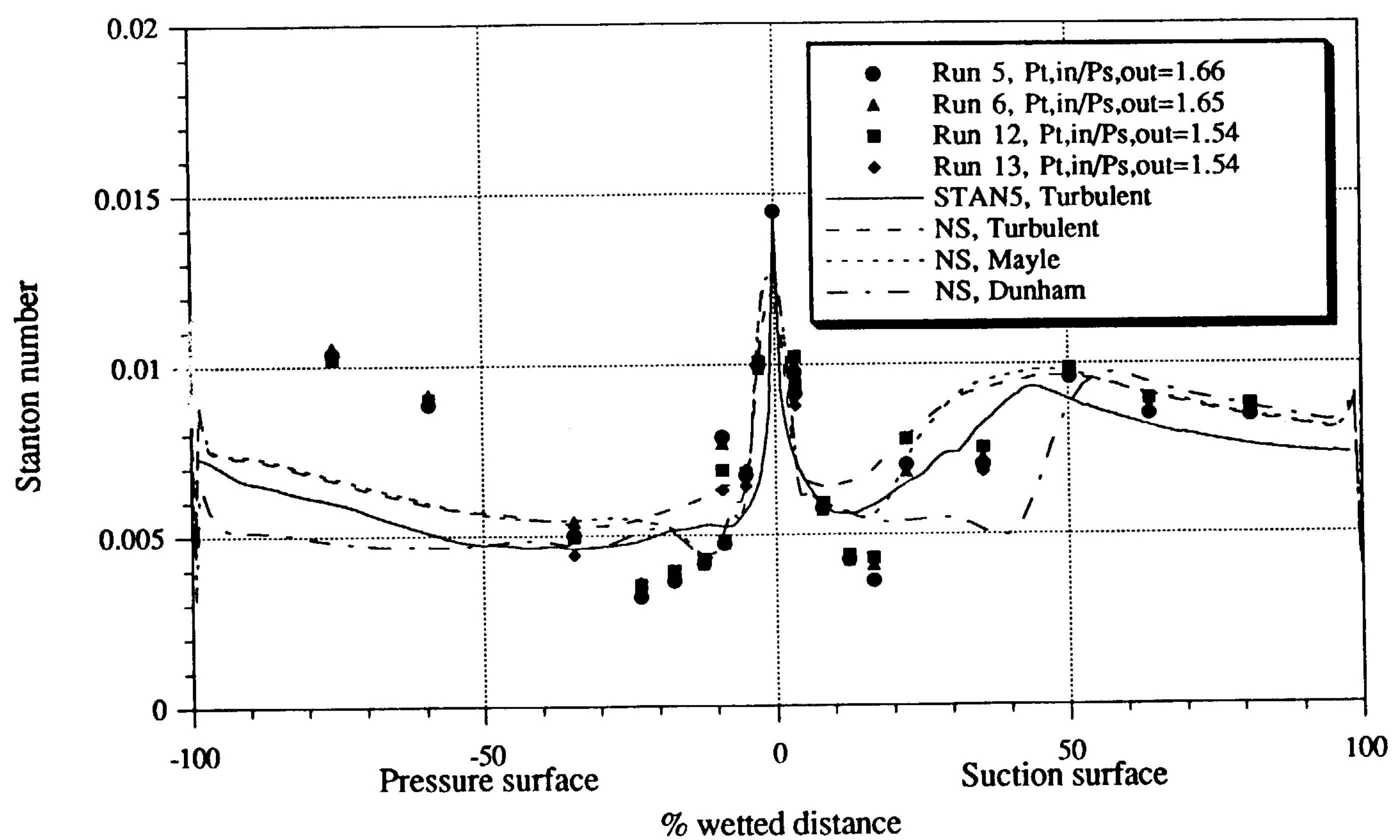

Figure 3.2.2. Stanton number distribution on first vane, 50% span, Re~250,000 results.

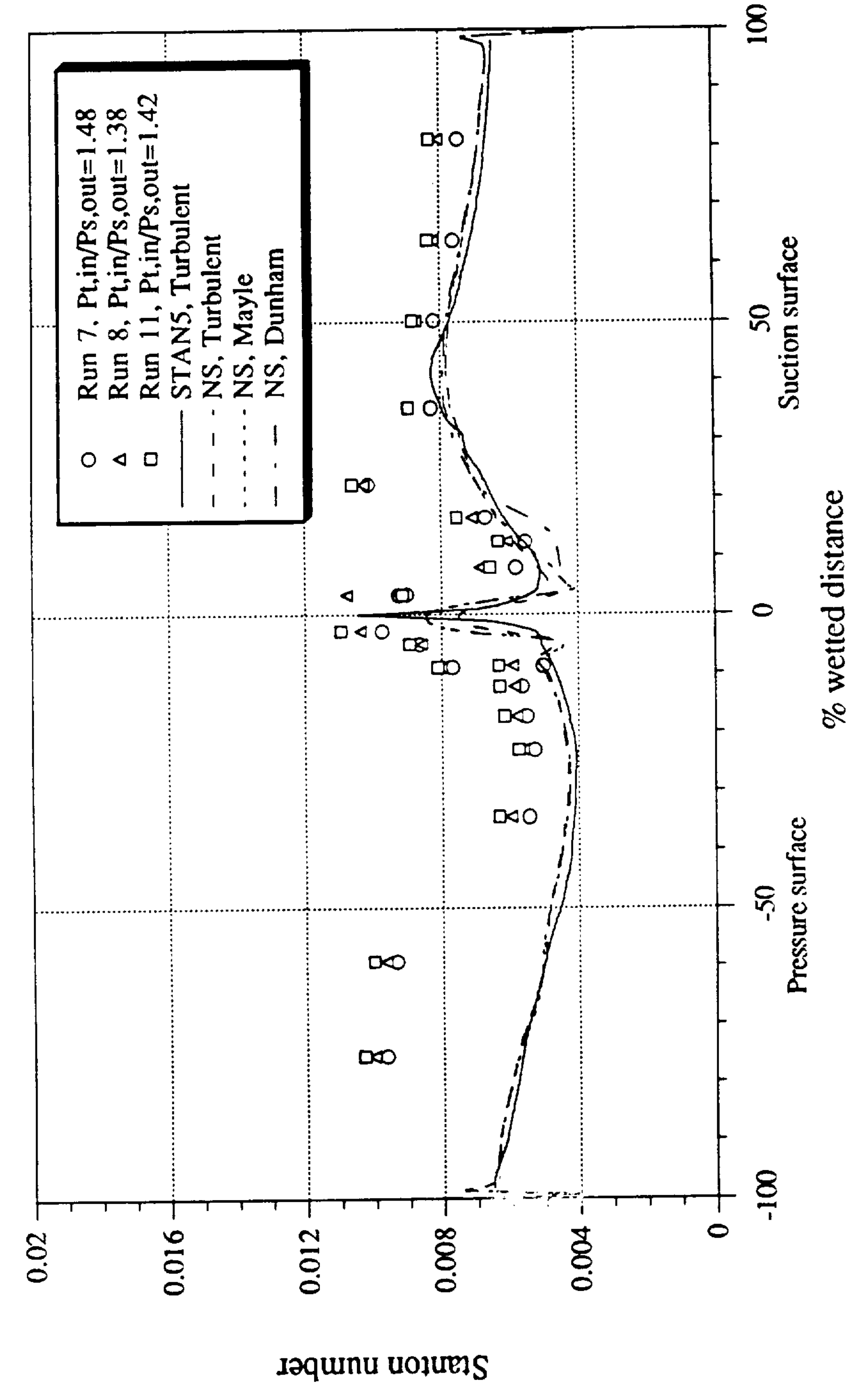

Figure 3.2.3. Stanton number distribution on first vane, 10% span. closed symbols: Re~140,000 data, open symbols: Re~250,000 data

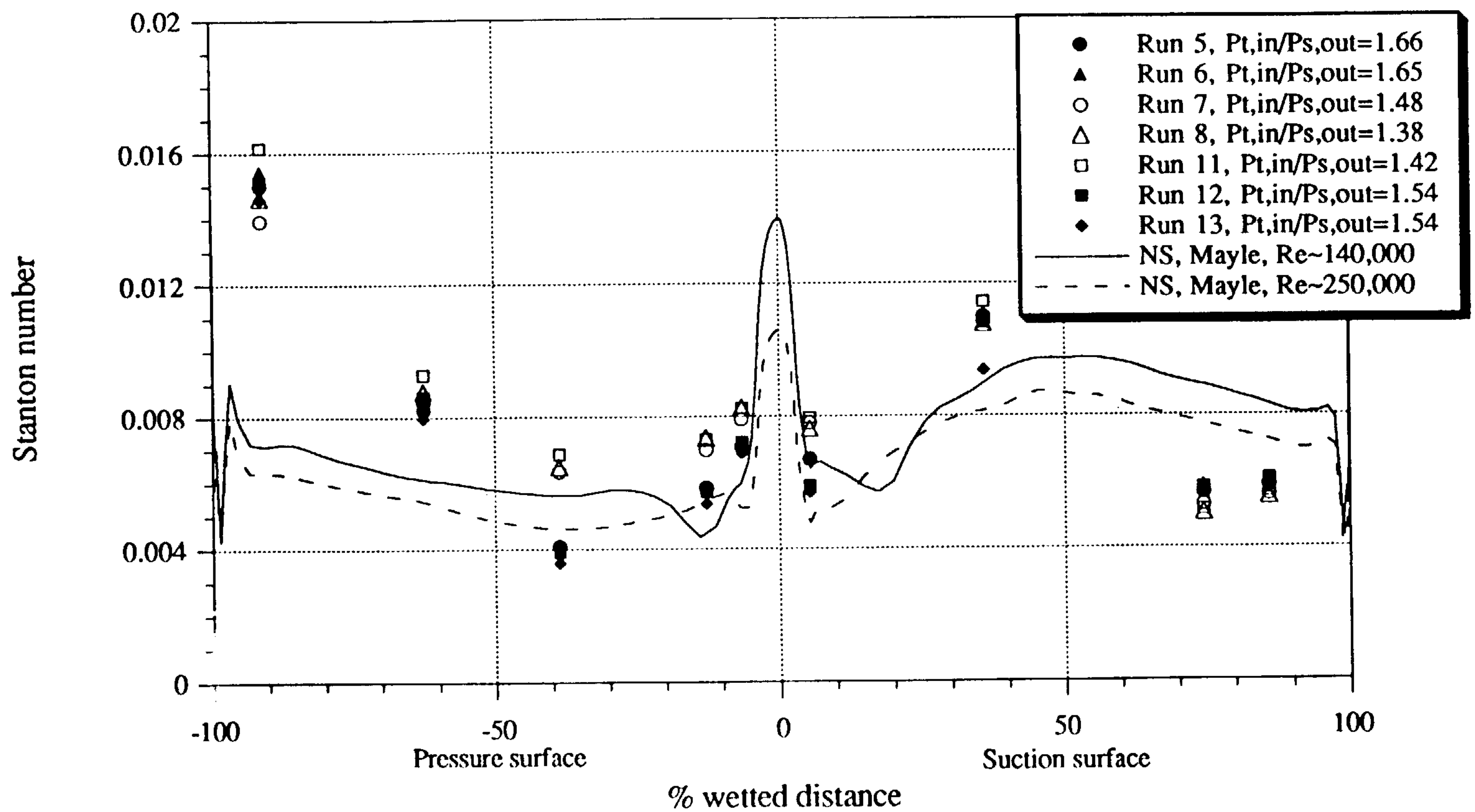

Figure 3.2.4. Stanton number distribution on first vane, 90% span
closed symbols: Re~140,000 data, open symbols: Re~250,000 data

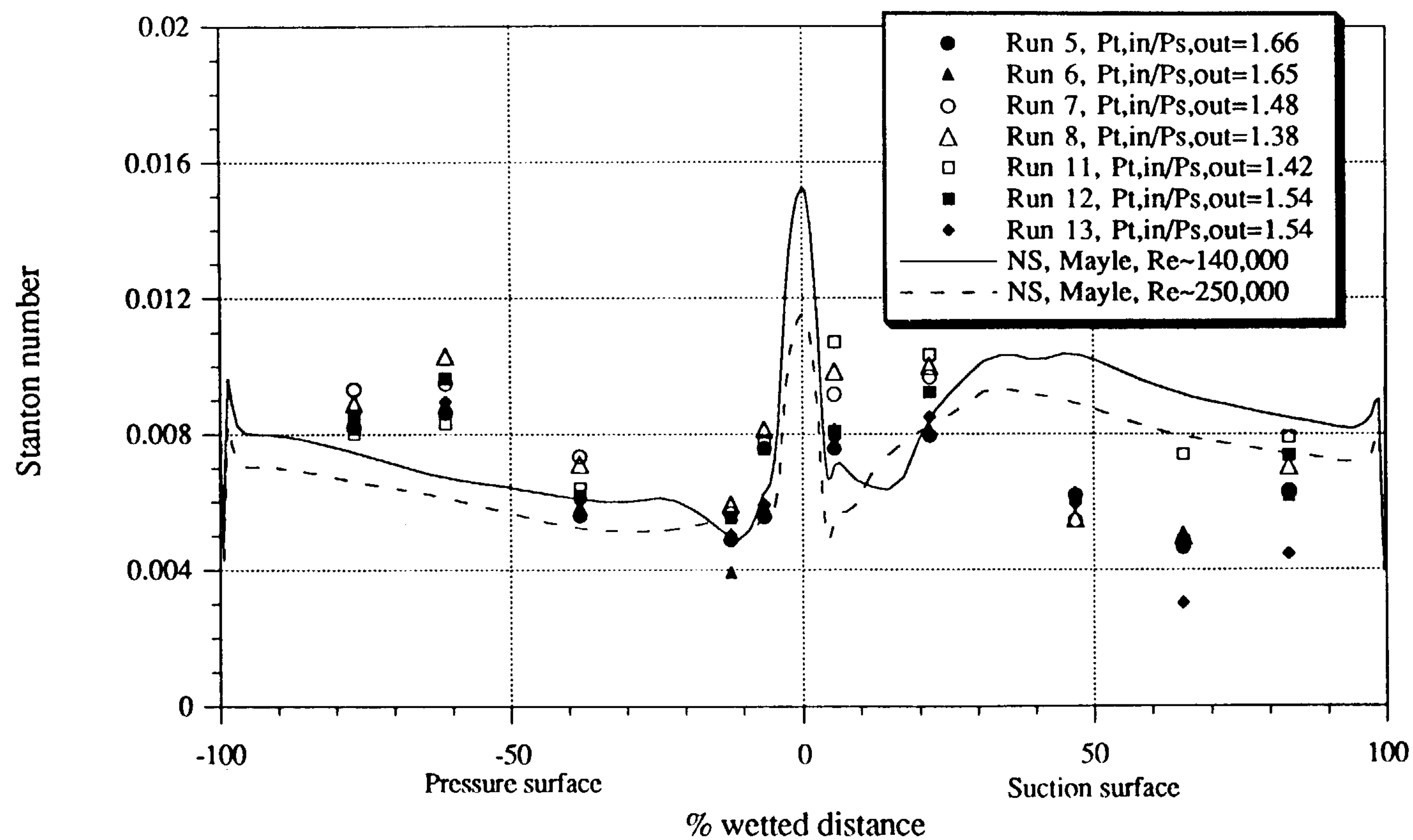

using the quasi-3D Navier-Stokes analysis described by Boyle (1991) and Gaugler's modified version the STAN5 boundary layer analysis of Crawford and Kays (1976). The predictions including transition were obtained by incorporating the transition model of Mayle, 1991 and the transition model due to Dunham, 1972 into the just noted Navier-Stokes analysis. Of the two fully turbulent predictions, the STAN5 prediction illustrates better overall agreement with the data. On the suction surface, the STAN5 prediction doesn't fall as low as the data in the vicinity of 15% wetted distance, and it doesn't climb as high as the data beyond 50% wetted distance. On the pressure surface, both of the fully turbulent predictions agree with the data reasonably well from the stagnation point to about 40% wetted distance. The data points at 60% and 80% wetted distance are significantly greater than the prediction. It was noted earlier in this section that this trend has been seen previously for full-stage turbines. This same trend was noted by Nealy, et al., 1984 for a vane ring downstream of a combustor. However, the Navier-Stokes analysis used here was applied to those data (Boyle, 1991) and reasonably good agreement between data and prediction was obtained. It is felt that the relatively high upstream turbulence in itself is not sufficient to account for the high pressure surface heat transfer, since the local turbulence level decreases significantly as the flow accelerates through the vane passage. The good agreement between the STAN5 boundary layer prediction and the Navier-Stokes fully turbulent analyses suggests that the numerical solutions of the analyses are not the source of the disagreement with the experimental data.

For the calculation incorporating the Dunham, 1972 transition model, transition occurs midway along the suction surface. However, the prediction is not in good agreement with the experimental data from about 7% wetted distance to 50% wetted distance. This analysis predicts Stanton numbers along the pressure surface that are generally in agreement with STAN5 over the initial 50% of that surface. Beyond 50%, the shape of the Dunham prediction deviates from the other two and falls below them and well below the data. This is because the flow never becomes fully turbulent with this model. Also included on Figure 3.3.1 is the Navier-Stokes prediction with the Mayle, 1991 transition model incorporated. This prediction is in much better agreement with the data than is the other prediction incorporating transition. Overall, the Navier-Stokes prediction which includes the Mayle transition model appears to be in better agreement with the data than any of the other predictions.

Figure 3.2.2 presents a comparison between the high Reynolds number data and the same four predictions described above. There is very little difference among the predictions at this higher Reynolds number except in the vicinity of the stagnation point and in the region of 5% to 20% on the suction surface. Both the N-S and the STAN5 solutions predict the stagnation region data reasonably well. The N-S solution with the Mayle transition model predicts the 5% to 20% wetted distance region better than the N-S solution with the Dunham model. On the pressure surface, all of the predictions are in reasonably good agreement with each other and all fall below the data from the stagnation point to about 40% wetted distance. The experimental results at 60% and 80% wetted distance are underpredicted by a significant amount by all four solutions. In summary, the predictions shown in Figures 3.2.1 and 3.2.2 show best agreement with the data when a fully turbulent analysis is used, even for the low Reynolds number cases. The transition models of both Mayle and of Dunham are highly dependent on the freestream turbulence intensity. Previous measurements gave an intensity of about 6% at the turbine inlet. At the low Reynolds number, Dunham's model predicts the start of transition too far downstream on the suction surface. Mayle's model agrees better with the data. At the high Reynolds number, transition occurs close to the leading edge, and there is little difference among the predictions.

Figures 3.2.3 and 3.2.4 present the first vane Stanton number results at 10% and 90% span, respectively. Both sets of Reynolds number data are included on these figures. The N-S prediction with the Mayle transition model has been selected for comparison with the experimental data. It would be anticipated that the high Reynolds number data set should be consistently lower than the low Reynolds number data by about 15% ($(2)^{0.2}=1.15$). There is sufficient uncertainty in the Stanton number results as described in Section 4 that generally, the data sets appear to overlap. The agreement between the suction surface prediction and the data is not as good as it was at midspan for either 10% or 90% span. In general, beyond 50% wetted distance, the prediction fell well above the data on the suction surface. The data point at 60% wetted distance is above the prediction, but no more so than the suction surface data points are below the prediction. The pressure surface data at 90% span are in as good agreement with the prediction as has been seen at any location on this vane.

3.3 First Blade Surface Stanton Number Results

3.3.1 Discussion of blade data

Figures 3.3.1 and 3.3.2 present the measured Stanton number distributions for the first blade at midspan for Reynolds numbers of 140,000 and 250,000, respectively. The Reynolds number data sets are both given on the same figure for the 10% span (Figure 3.3.3) and the 90% span (Figure 3.3.4) locations. The heat-flux values in the vicinity of the leading-edge region are known to be sensitive to incidence angle. However, the rotor speed range over which data were taken in these experiments (99% to 103% of design) was sufficiently small that it is unlikely that incidence angle had a significant effect. Likewise, the local Stanton number is sensitive to stage pressure ratio because of the change in incidence angle associated with the higher axial velocity (increased weight flow) at the lower value of pressure ratio. From the weight flow data presented in Table 1 it was difficult to obtain an estimate of the incidence angle variation resulting from the difference in pressure ratio. The experimental data (runs 5, 6, 12, and 13) at the 10% and 90% spanwise locations are consistent with each other near the leading edge in that the Stanton numbers for runs 5 and 6 are consistently greater than those for runs 12 and 13.

Figure 3.3.1. Stanton number distribution on first blade, 50% span, Re~140,000.

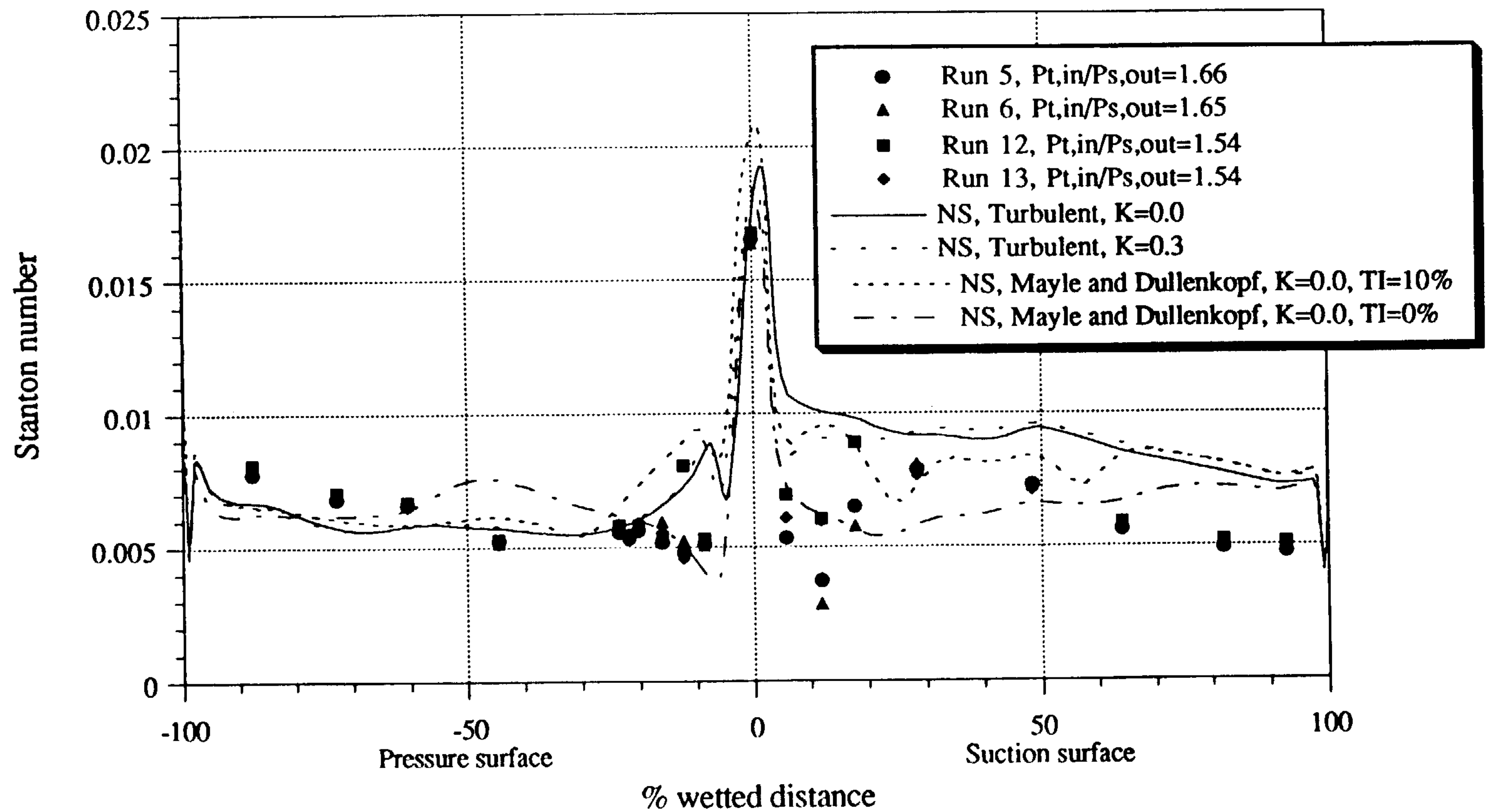

Figure 3.3.2. Stanton number distribution on first blade, 50% span, Re~250,000. Comparison with predictions for various roughness heights.

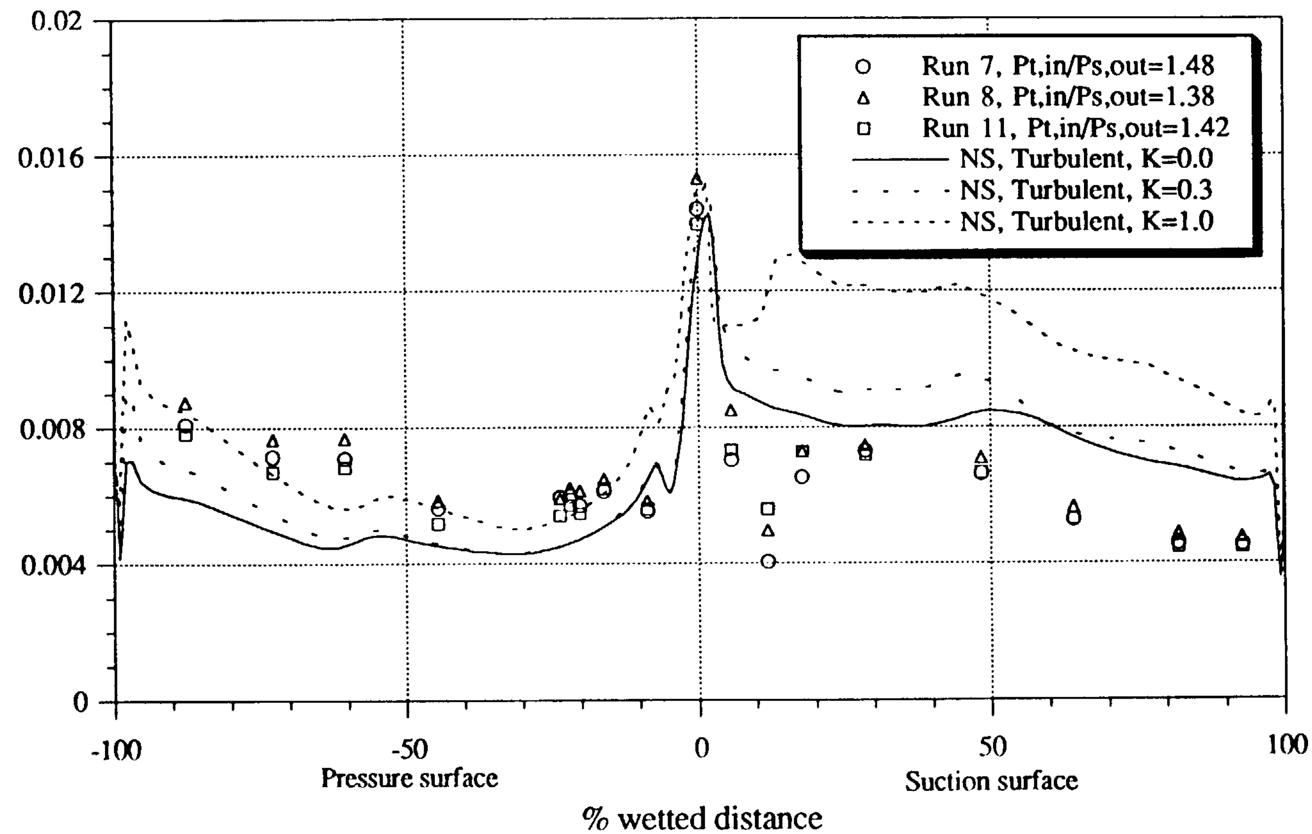

Figure 3.3.3. Stanton number distribution on first blade, 10% span
closed symbols: Re~140,000 data, open symbols: Re~250,000 data

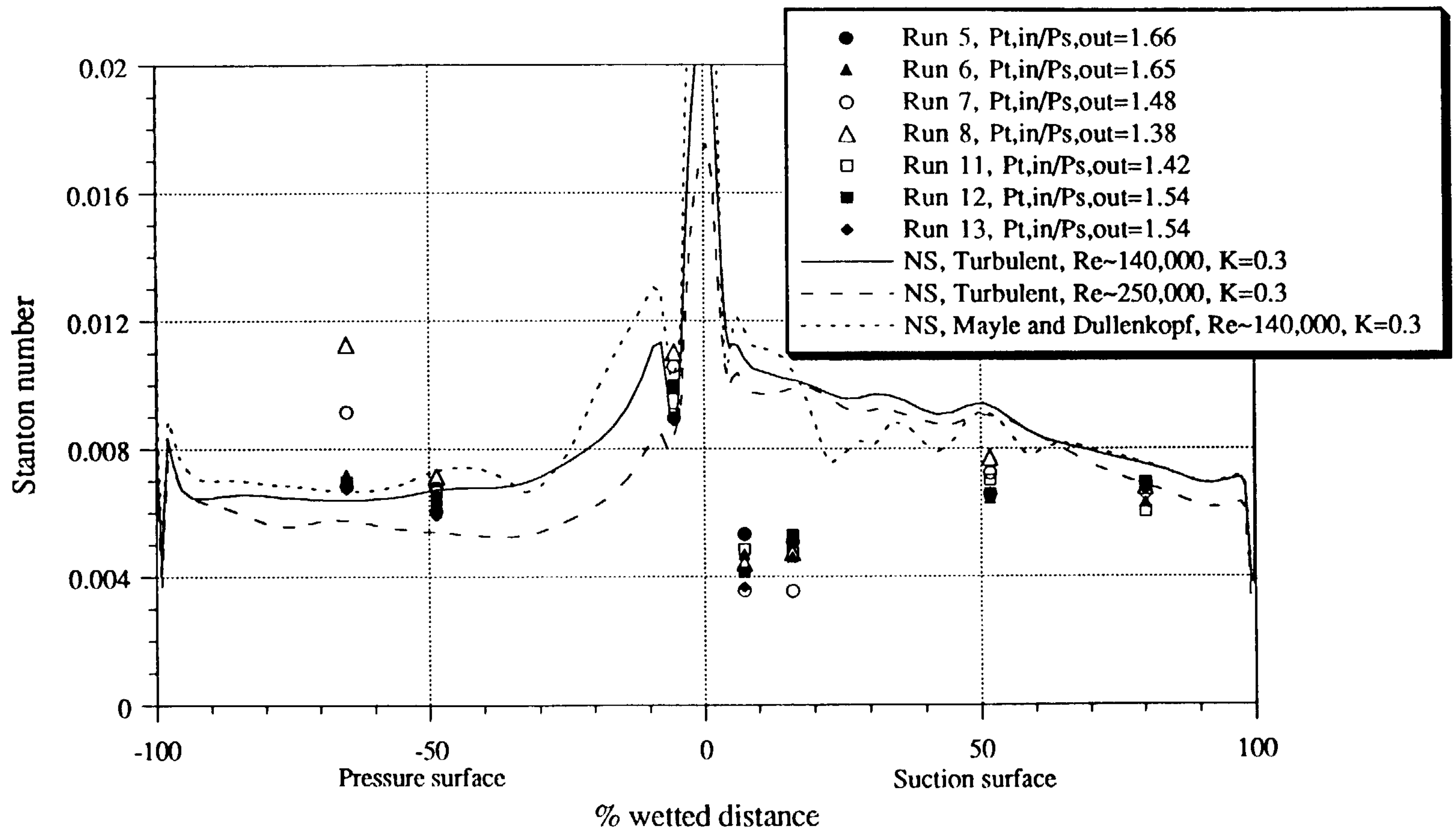

Figure 3.3.4. Stanton number distribution on first blade, 90% span
closed symbols: Re~140,000 data, open symbols: Re~250,000 data

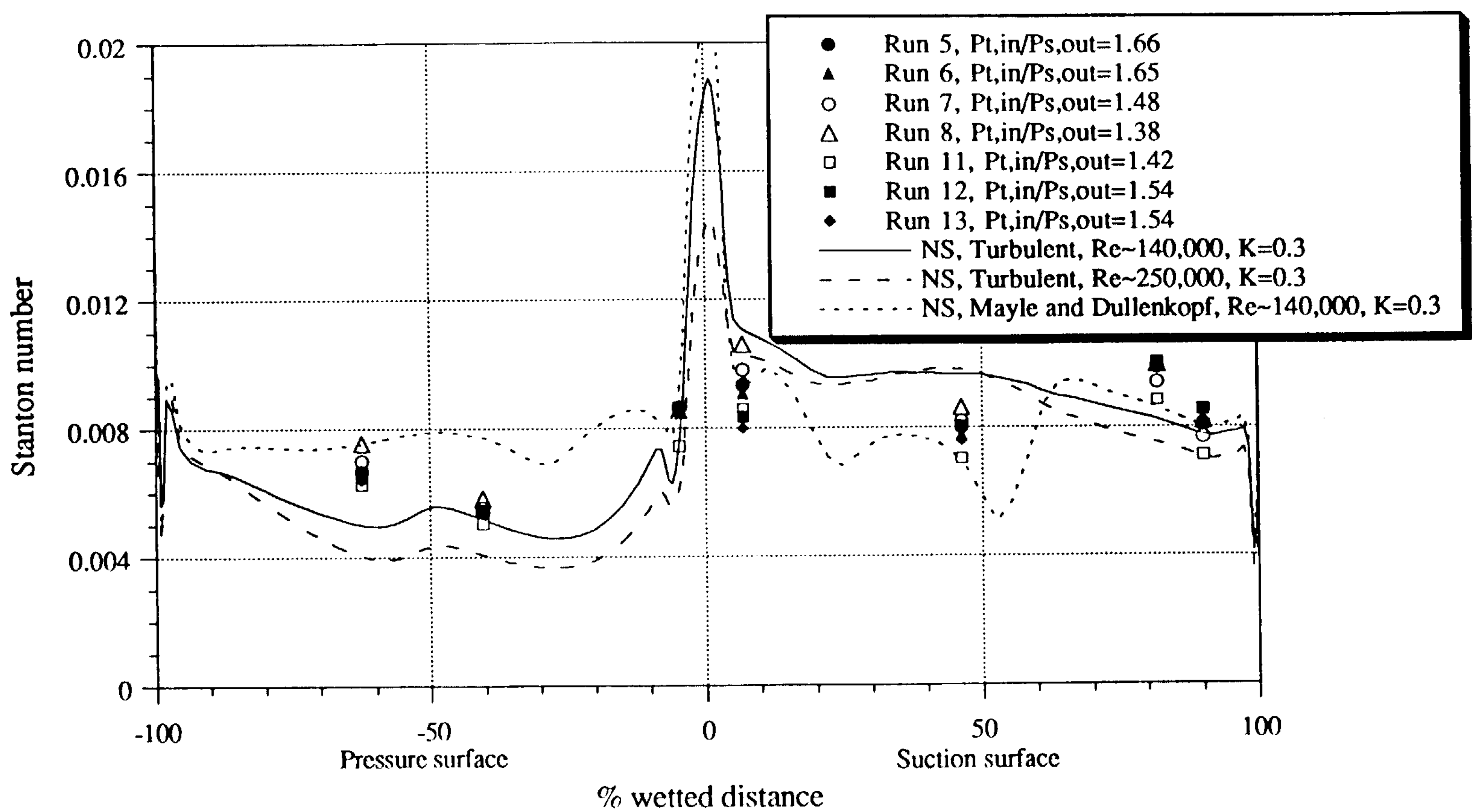

However, the trend in the Stanton number results from these same runs at midspan are opposite to that observed at 10% and 90% suggesting that if there was an influence, it didn't occur all along the leading edge. Another interpretation of the data would be that within the uncertainty of the data, no significant influence of pressure ratio or speed was observed for the range of conditions used here. Beyond 50% wetted distance, the results illustrate little influence on the Stanton number distribution for either the pressure or suction surface. Returning for a moment to the midspan results presented on Figure 3.3.1, at the stagnation point the experimental results are in agreement with each other, but immediately thereafter (from 0% to 15% wetted distance) on the suction surface and in the vicinity of 12% wetted distance the data do not coalesce. Three of the runs (run 6, 12, and 13) shown on this figure were for nominally 103% of design speed, and the other (run 5) for 99% of design speed. Two of the runs at 103% of design speed were for a stage pressure ratio of 1.54 (runs 12 and 13) while the other two runs were at a pressure ratio of about 1.65 (runs 5 and 6). At the 12% wetted distance location, two of the 103% speed points (runs 12 and 13 for the same stage pressure ratio) are in good agreement while the other one (run 6, higher pressure ratio) is low. Also note that runs 5 and 6, which are for the same stage pressure ratio but different speeds (99% and 103%), are in reasonably good agreement with each other suggesting that for this speed variation the influence on Stanton number distribution is not large.

The experimental data presented on Figure 3.3.1 show that the Stanton number fell rapidly from the stagnation point to about 10% wetted distance followed by a rapid increase, reaching a maximum value for the suction surface at about 25% wetted distance. On the pressure surface, the Stanton number increases from a minimum value in the vicinity of 15% wetted distance to a maximum near 90% wetted distance. The maximum values occurring on these two surfaces are comparable and well below the stagnation point value. Included on Figure 3.3.1 are two fully turbulent Navier-Stokes predictions, one for a rough airfoil and the other for a smooth airfoil, and a N-S prediction, with the

Mayle and Dullenkopf, 1989, 1990 intermittency model included, for a smooth airfoil. The STAN5 boundary layer analysis showed separation for the midspan pressure surface using the predicted inviscid flow field for a boundary condition and, therefore, the STAN5 prediction could not be obtained for the blade. The Navier-Stokes analyses do not indicate a significant increase in heat transfer due to blade surface roughness. On the pressure surface both of the fully turbulent analyses are in good agreement with the experimental data. However, on the suction surface these same predictions fall consistently above the data. The third prediction included on Figure 3.3.1 is in essential agreement with the fully turbulent predictions on the pressure surface. On the suction surface, it also overpredicts the data, but is closer than the fully turbulent predictions. The predicted heat transfer at the leading edge is higher than the experimental data. The average augmentation of the heat transfer in the laminar region was calculated assuming a turbulence intensity of 10%. The transition model used a background turbulence intensity of 2%. The intermittency model overpredicted the heat transfer at the leading edge by about 33%. This indicates that the augmentation due to freestream turbulence was excessive. The Froessling number at the stagnation region was calculated from the experimental results for this case, and using the cylinder in cross flow correlation of Traci and Wilcox, 1975 a freestream turbulence intensity of about 7% was estimated.

Along the entire pressure surface the fully turbulent predictions are nearly identical, and agree well with the experimental data. These predictions for the rotor are in contrast with those for the vane, where the pressure surface heat transfer exceeded the fully turbulent prediction. The transitioning prediction, which includes the effect of freestream turbulence, overpredicts the pressure surface heat transfer. The largest source of uncertainty in the heat transfer predictions is due to the uncertainty in the freestream turbulence for the augmentation of the laminar viscosity due to this freestream turbulence.

3.3.2 Blade surface roughness considerations

The first stage blade of this turbine appeared to be rough and there was concern that the roughness may enhance the heat transfer. Blair and Anderson, 1992 have illustrated that this enhancement can be significant. The influence of surface roughness on the blade data presented herein was therefore investigated.

Boyle and Civinskas, 1991, investigated the influence of surface roughness on the predicted heat transfer to the surface. The effective roughness height was strongly dependent on both the roughness and the density. The roughness density can be found from the trace shown in Figure 2.2.7. In this figure, the horizontal axis is compressed by more than a factor of ten over the vertical axis. Even though the blade shown in Figure 2.4,1, 2.4.2, and 2.5.1 are visibly rough, the peaks are not spaced closely together.

Comparing the two analyses shows that the effect of surface roughness is very small. This was not unexpected. The insensitivity to surface roughness is the result of both the low Reynolds number, and the effect of surface roughness density. In the Navier-Stokes analysis a reference y^+ was used for an a priori determination of the grid spacing. This reference value is given by

$$y^+_{REF} = 0.17y\ Re^{0.9}/s^{0.1}$$

where y is the distance from the surface, Re is the exit Reynolds number per unit length, and s is a characteristic distance.

An analogous reference roughness height is

$$k^+_{REF} = 0.17k\ Re^{0.9}/s^{0.1}$$

For the low Reynolds number case the exit unit Reynolds number was 1.28 x 10^7/m (3.9 x 10^6/ft).

The roughness height, k, in the above equations is not the actual roughness height, but rather the equivalent roughness height. The equivalent roughness height was estimated using the approach taken by Boyle and Civinskas, 1991 to be less than 0.3 of the actual roughness height. Even though the actual roughness height was ~150,000 Å (590 microinches), the value of k^{+}_{REF} was calculated to be only 2.7. This value of the reference roughness height is only approximate since it is based on a friction factor for a smooth flat plate. Nonetheless, the value of k^{+} is less than the value of 5 for a hydraulically smooth surface. Consequently, the rough and smooth heat transfer predictions are nearly identical. It should be noted that blades with this surface roughness, when operated in the SSME environment, are no longer hydraulically smooth due to the much higher Reynolds number of the actual engine. Calculations showed an increase in heat transfer of up to 25% due to surface roughness at the SSME operating conditions for K=0.3. The parameter K represents the ratio of the equivalent roughness height (k) to the actual roughness height.

Figure 3.3.2 presents the first blade midspan Stanton number data for the high Reynolds number case. Also included on this figure are three N-S predictions which were performed for different surface roughness heights. The N-S turbulent prediction with K=0 is consistently above the N-S prediction with the Mayle and Dullenkopf intermittency model. The value of Stanton number at the stagnation point is predicted reasonably well by the N-S solution. On the suction surface, the N-S turbulent prediction for a smooth surface (K=0) is consistently above the data. The prediction for K=0.3 is about 12% high[illegible] the initial 50% of the surface, then about the same over the remainder of the surface. The prediction for K=1.0 represents a significant enhancement and is well above the data over the entire surface.

On the pressure surface of the blade, Figure 3.3.2 illustrates that the shape of the predictions is consistent with the data. The predictions for K=0 and K=0.3 both fall below the data. The prediction for K=1.0 is in reasonable good agreement with the data over the entire pressure surface.

Figures 3.3.3 and 3.3.4 present the experimental data and comparisons with predictions for the 10% span and the 90% span locations, respectively. Both sets of Reynolds number data are included on these figures. Figure 3.3.3 includes the fully turbulent N-S predictions for both Reynolds numbers and the N-S prediction with the Mayle and Dullenkopf intermittency model for the low Reynolds number. At the high Reynolds number, this prediction is essentially the same as the corresponding N-S fully turbulent prediction. For the suction surface, there is very little difference among the three predictions. The data between 5% and 15% wetted distance are substantially below the predictions, while the data between 50% and 80% are below, but in reasonable agreement with the predictions. For the pressure surface, the fully turbulent prediction is generally below the data while the intermittency model provides a reasonable representation of the data. The comparison presented in Figure 3.3.4 for the 90% span location demonstrates reasonably good agreement between the data and the intermittency model prediction for the suction surface and correspondingly good agreement on the pressure surface for the N-S fully turbulent prediction.

3.4 Second Vane Surface Stanton Number Results

The second vane Stanton number measurements are shown in Figures 3.4.1 for both Reynolds number cases and both stage pressure ratios. For the second vane, only midspan heat-flux data wer[illegible] Figure 3.4.1 also includes the predicted midspan Stanton number distributions. A fully turbulent and an intermittency model prediction are shown. The high Reynolds number intermittency prediction provides a good prediction at the stagnation point. On the suction surface, the fully turbulent and the low Reynolds number intermittency model predictions are conservative over the entire surface. The high Reynolds number intermittency model prediction is a better representation of the

Figure 3.4.1. Stanton number distribution on second vane, 50% span
closed symbols: Re~140,000 data, open symbols: Re~250,000 data

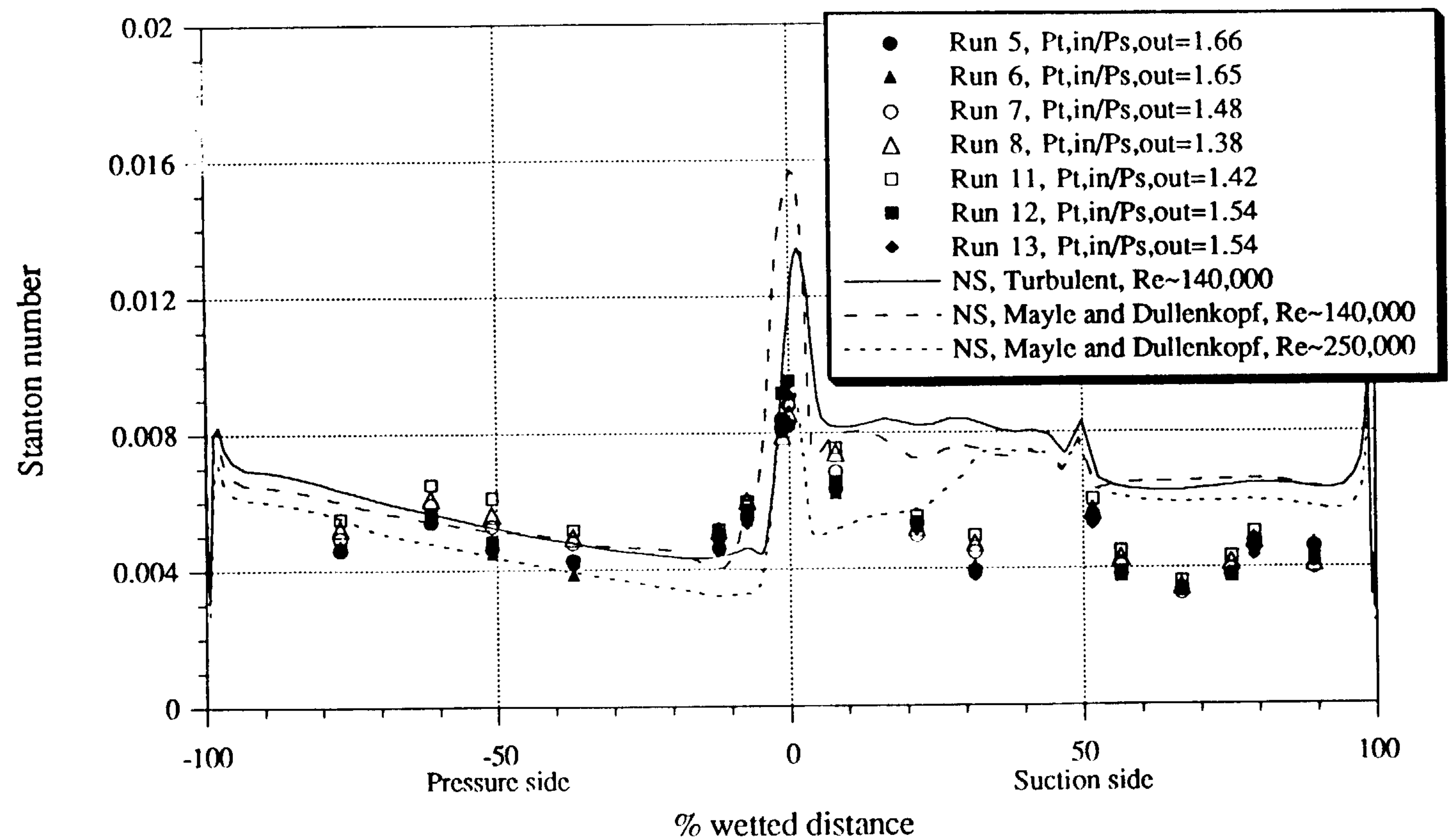

data. On the pressure surface, both the fully turbulent and the low Reynolds number intermittency models provide reasonable predictions of the data. The high Reynolds number intermittency model prediction on this surface is lower than the other two predictions by about 15% as would be anticipated.

3.5 Blade Platform, Blade Tip and Shroud Results for Design Speed Condition

Figures 3.5.1 and 3.5.2 present the blade platform Stanton number distribution for the low and high Reynolds number conditions, respectively, at three values of overall stage pressure ratio. At the higher Reynolds number, the data for the values of stage pressure ratio are in reasonable agreement. The low Reynolds number results presented in Figure 3.5.1 also suggest that the influence of pressure ratio is small. Further, the influence of Reynolds number appears to be small. For both Reynolds number cases, the trend of the data is to show a relatively small Stanton number increase in the chordwise direction. However, with only two measurement locations, it is difficult to determine anything more than this trend. The platform Stanton number values are of the same order as the blade midspan values.

Figures 3.5.3 and 3.5.4 present the Stanton number results obtained from the gages located in the blade tip at the low and high Reynolds number condition, respectively. The high Reynolds number results of runs 7, 8 and run 11 (Figure 3.5.4) were obtained at values of pressure ratio ranging from 1.38 to 1.48. The results of run 11 are shown to consistently fall below those of run 8. Run 7, which was performed at the larger value of stage pressure ratio, produced results at the 75% chord location which are not consistent with a well defined influence of pressure ratio on the tip Stanton number. There also appears to be a rather wide range in Stanton number value at the 39% tip-region measuring station. The low Reynolds number experiments (which were run at stage pressure ratios of 1.54 and 1.65) illustrate even a more pronounced variation in results at the 18% measuring station (shown on Figure 3.5.3) than was shown at 39% tip

Figure 3.5.1--Stanton number distribution on the blade platform, Re~140,000.

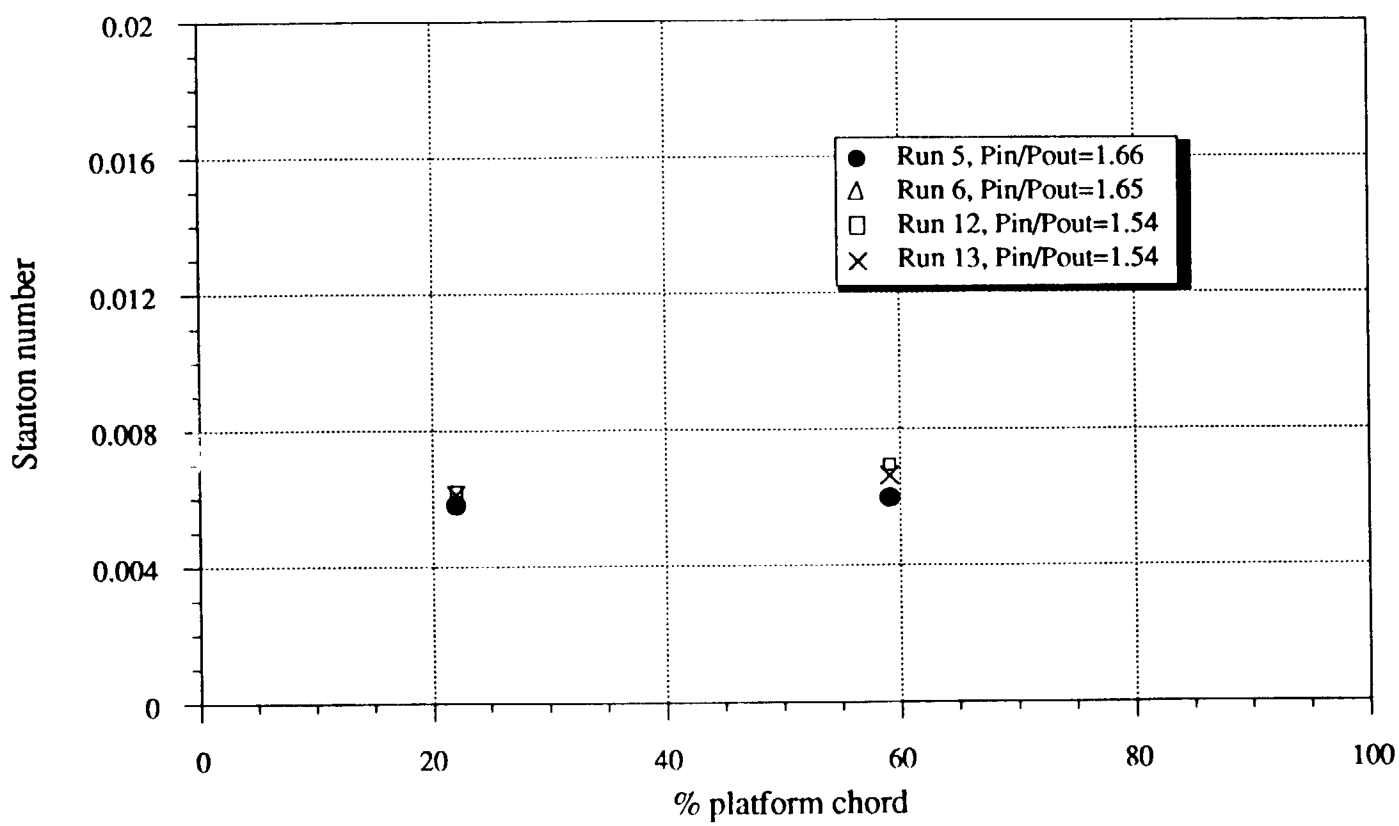

Figure 3.5.2--Stanton number distribution on the blade platform, Re~250,000.

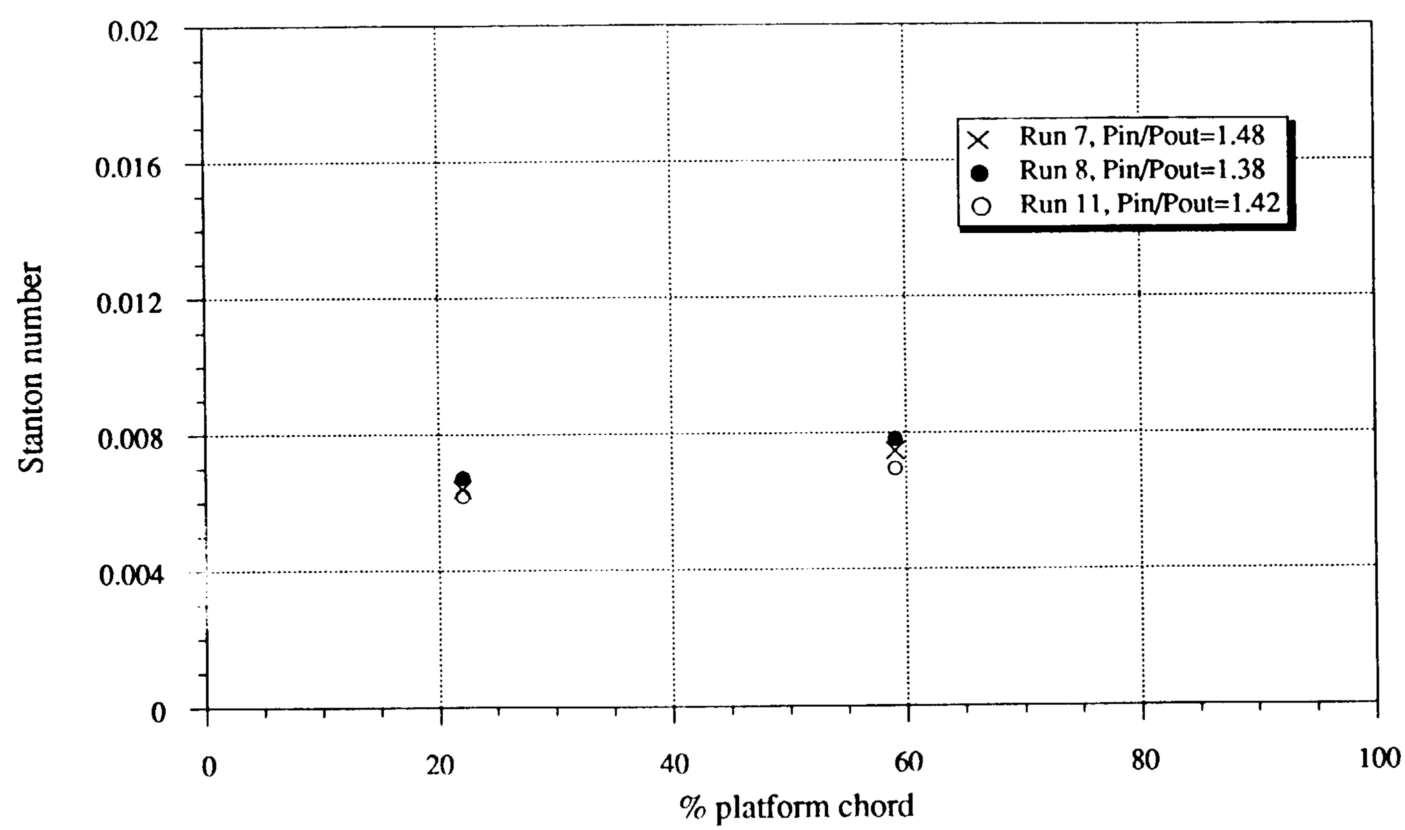

Figure 3.5.3--Stanton number distribution on the blade tip, Re~140,000.

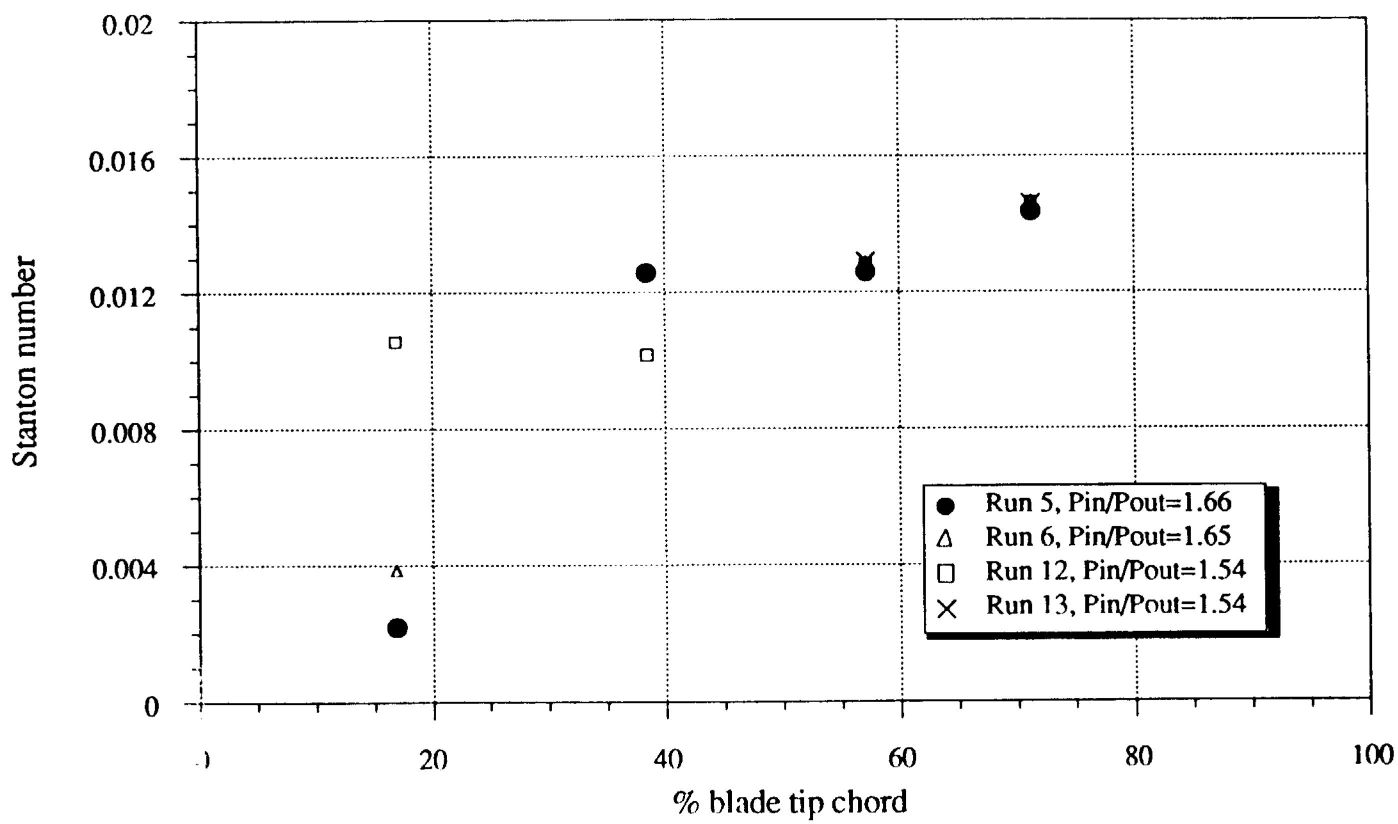

Figure 3.5.4--Stanton number distribution on the blade tip, Re~250,000.

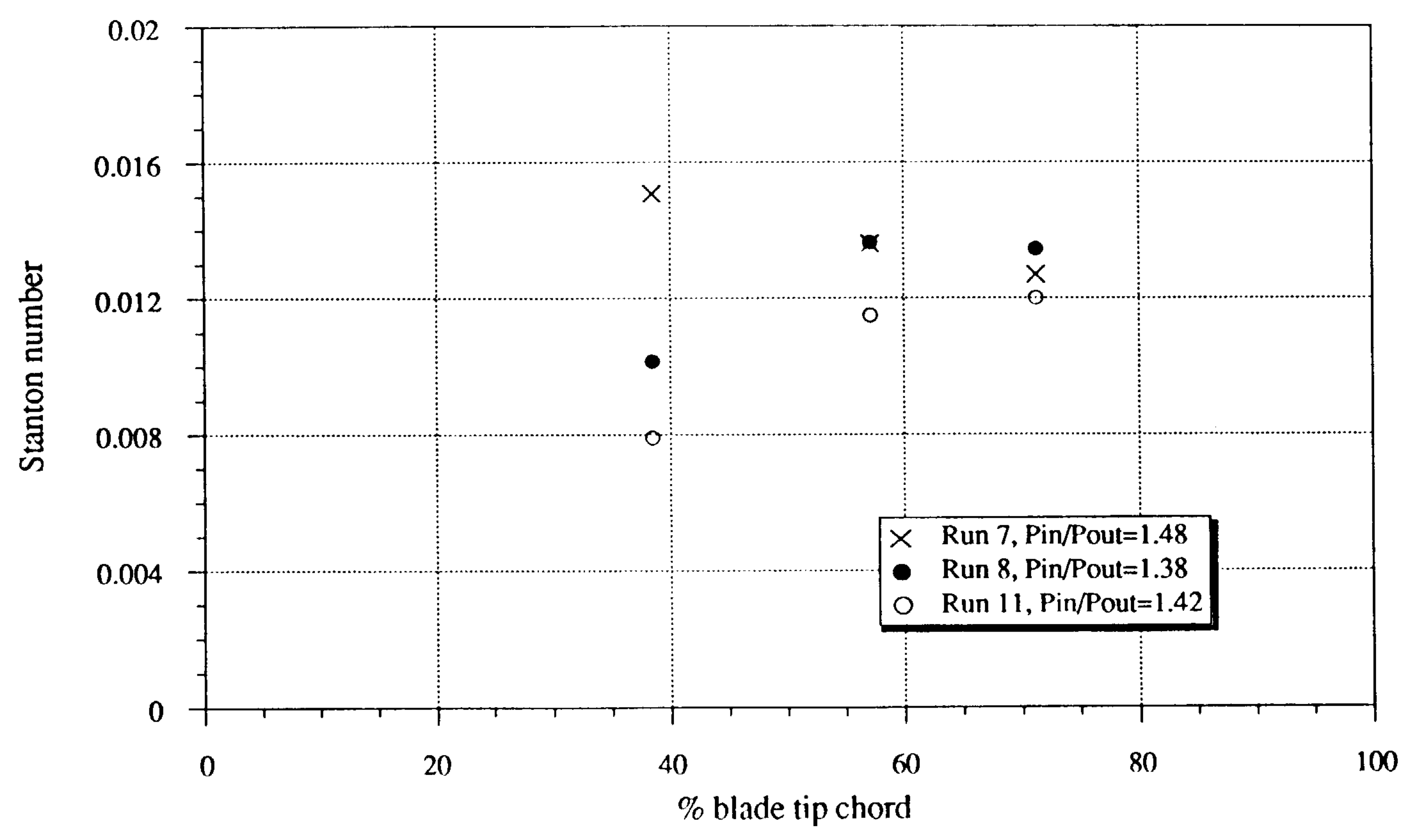

chord. There does not appear to be definitive influence of either Reynolds number or stage pressure ratio on the heat transfer results. For both Reynolds number cases, the tip region Stanton number values start out at small chord values with a rather wide variation, but converge near midchord. At chord values less than 40%, the tip Stanton numbers are on the order of the blade midspan values, but at large chord values the tip Stanton numbers rapidly approach the blade stagnation point value.

Figures 3.5.5 and 3.5.6 present the Stanton number distributions on the stationary shroud. The high Reynolds number data presented on Figure 3.5.6 illustrate a relatively high value of Stanton number over the entire region for which data were obtained. Stage pressure ratio does not appear to influence the results. Figure 3.5.5 presents corresponding results for the low Reynolds number test case. The results for both Reynolds numbers appear to be relatively independent of both Reynolds number and stage pressure ratio. For both Reynolds number cases, the shroud Stanton numbers are not as large as the blade stagnation point or tip values, but they are larger than the values measured at other blade locations.

Figures 3.5.7 and 3.5.8 are composite plots of the platform, tip and shroud Stanton number data as a function of blade chord. The root and tip locations are noted on the abscissa. For the data presented in both of these plots, the tip data are shown to be generally greater than either the platform or shroud data. The shroud data fall between the tip and the platform levels.

3.6 Vane and Blade Surface Results for Off-Design Speed (68% Design Speed)

Figures 3.6.1-3.6.3 plot the Stanton number distributions for the 50%, high Reynolds number runs on the first vane, first blade and second vane, respectively. These are included to complete the comparison between full speed and off-design speed data. As would be expected, speed has relatively little influence on the first vane for the vane pressure ratio of this turbine (Figure 3.6.1). Figure 3.6.2 presents the first blade data and

Figure 3.5.5--Stanton number distribution on the blade shroud, Re~140,000.

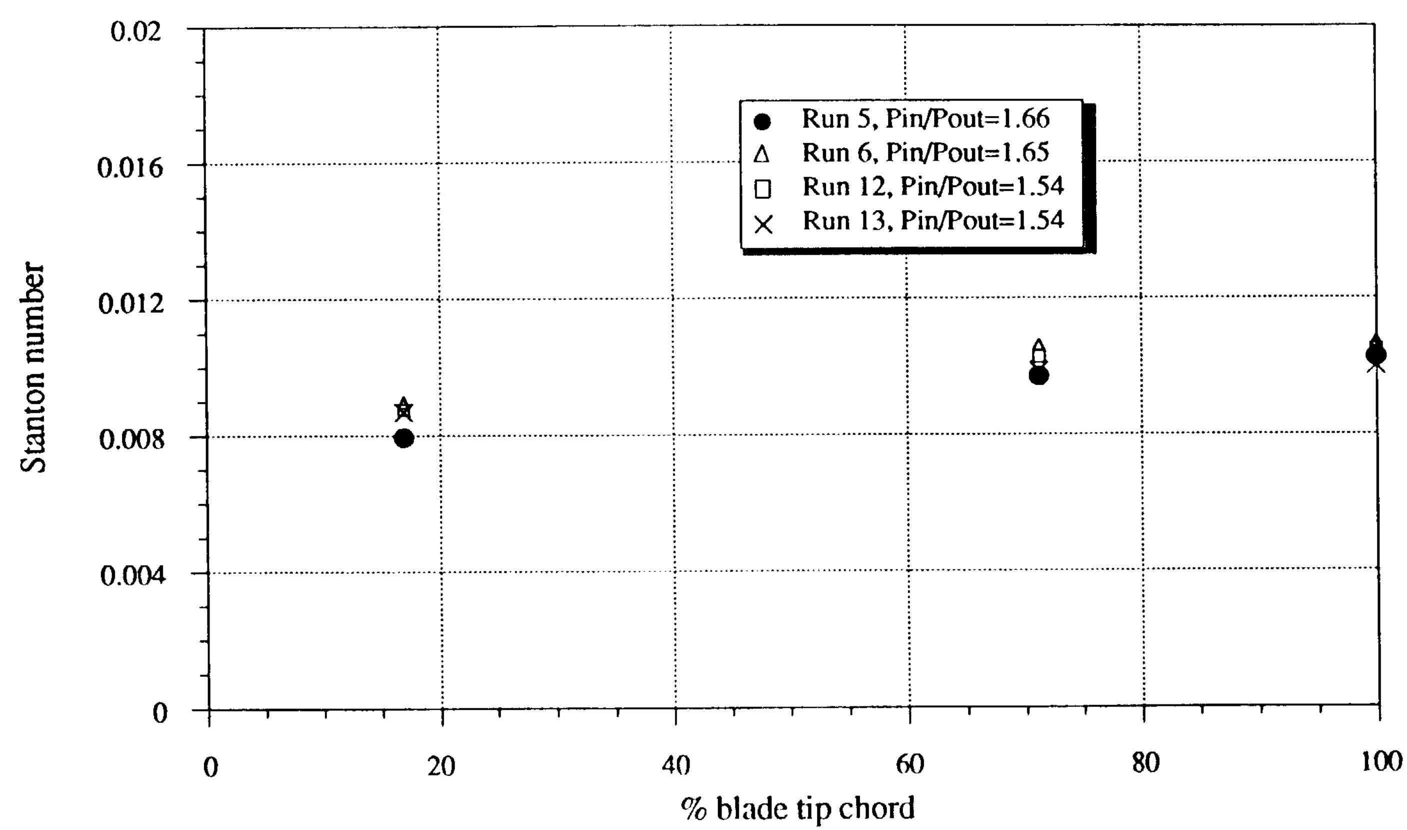

Figure 3.5.6--Stanton number distribution on the blade shroud, Re~250,000.

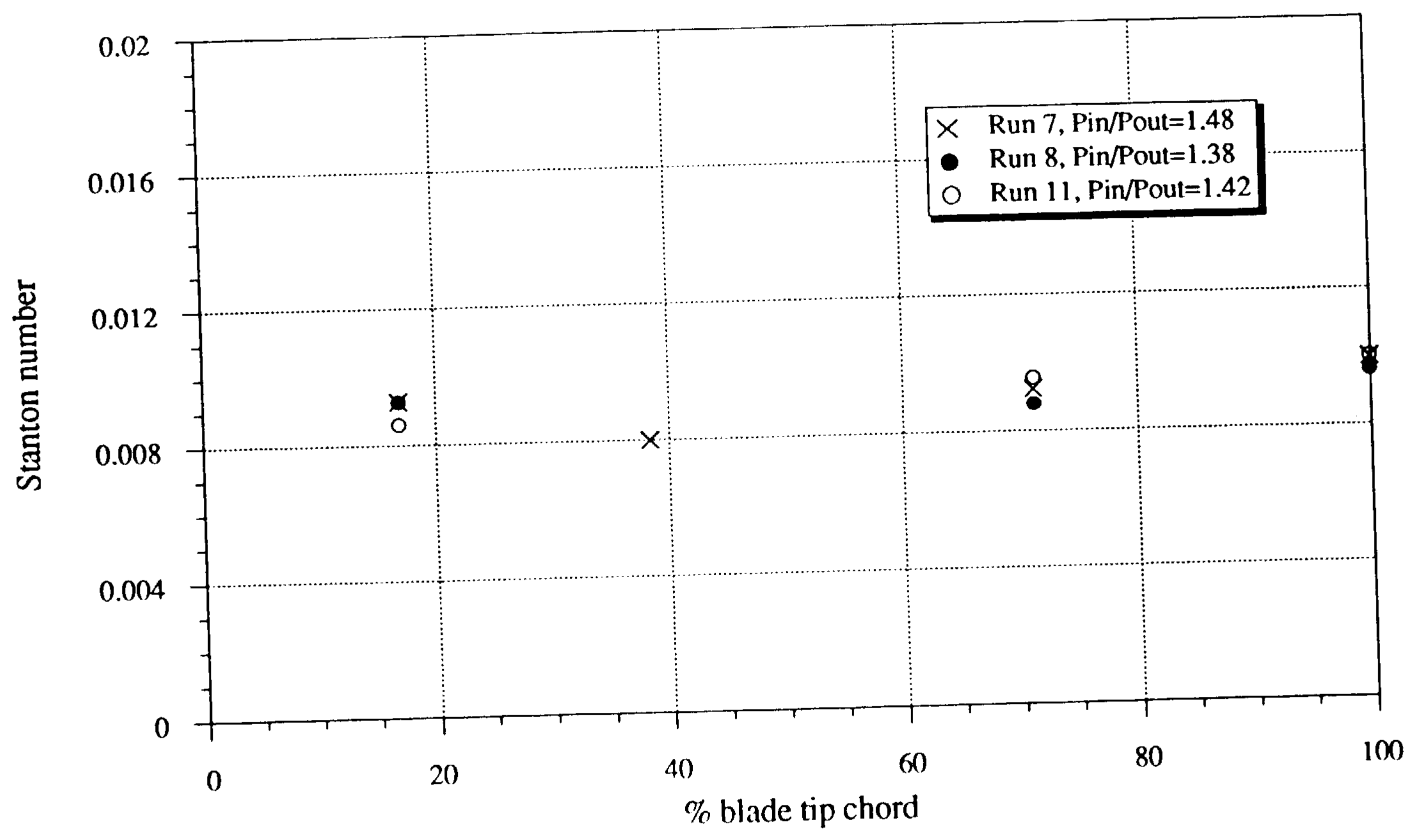

Figure 3.5.7--First blade tip, shroud, and platform, Re~140,000 (Runs 5,6,12, and 13)

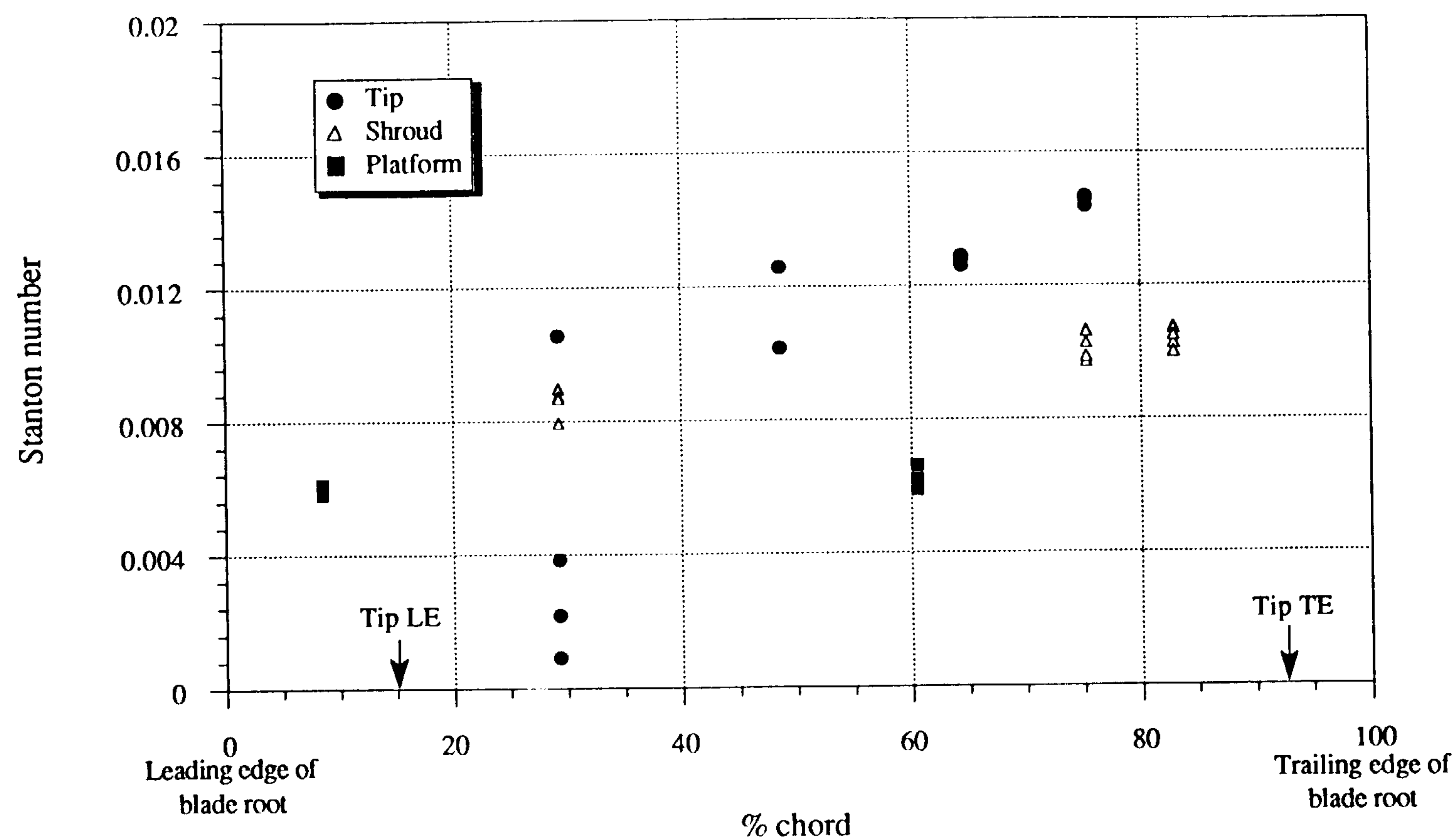

Figure 3.5.8--First blade tip, shroud, and platform, Re~250,000 (Runs 7,8, and 11)

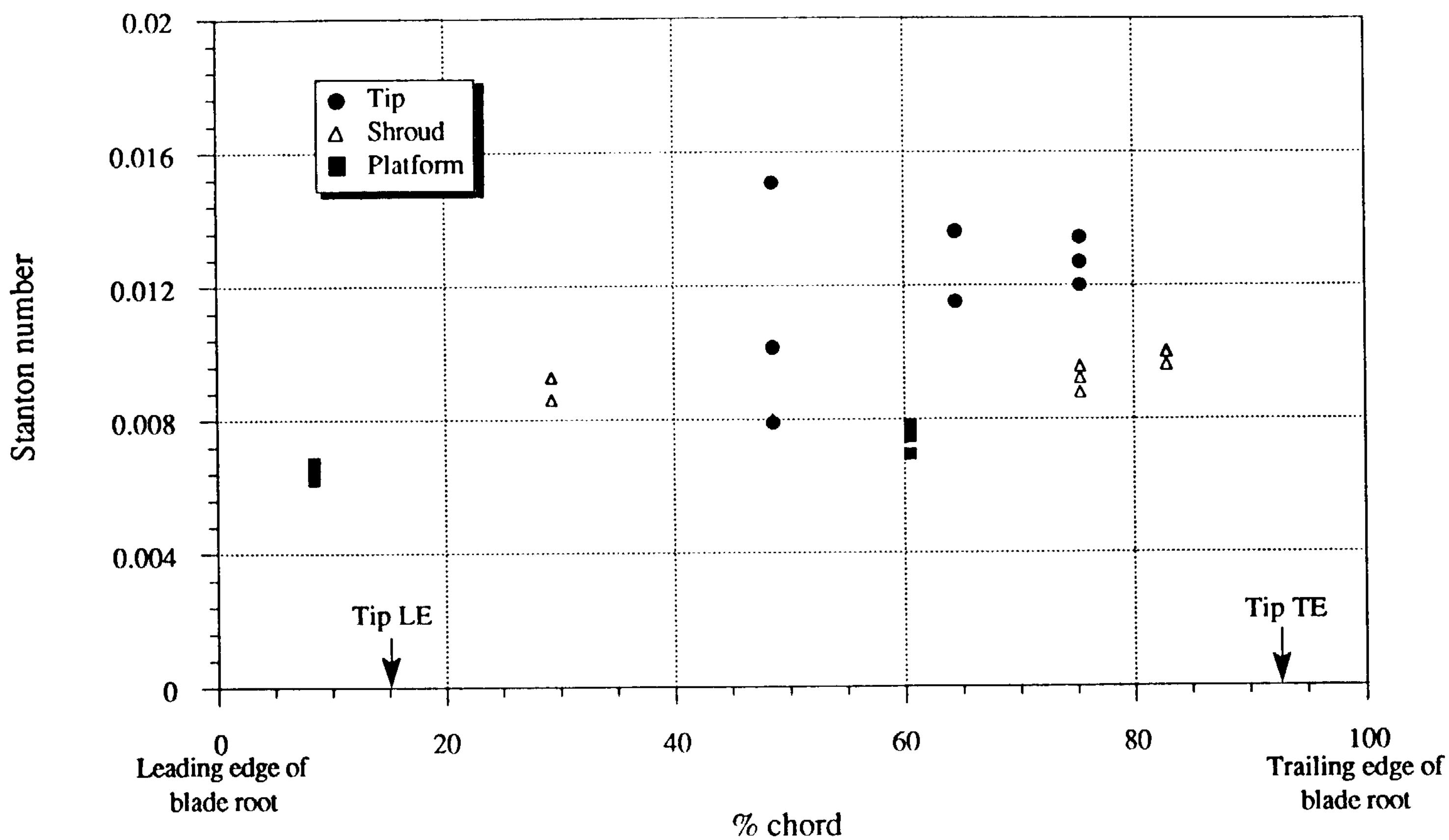

Figure 3.6.1--Stanton number distribution at 50% span on first vane, Re~250,000, comparison with off speed data.

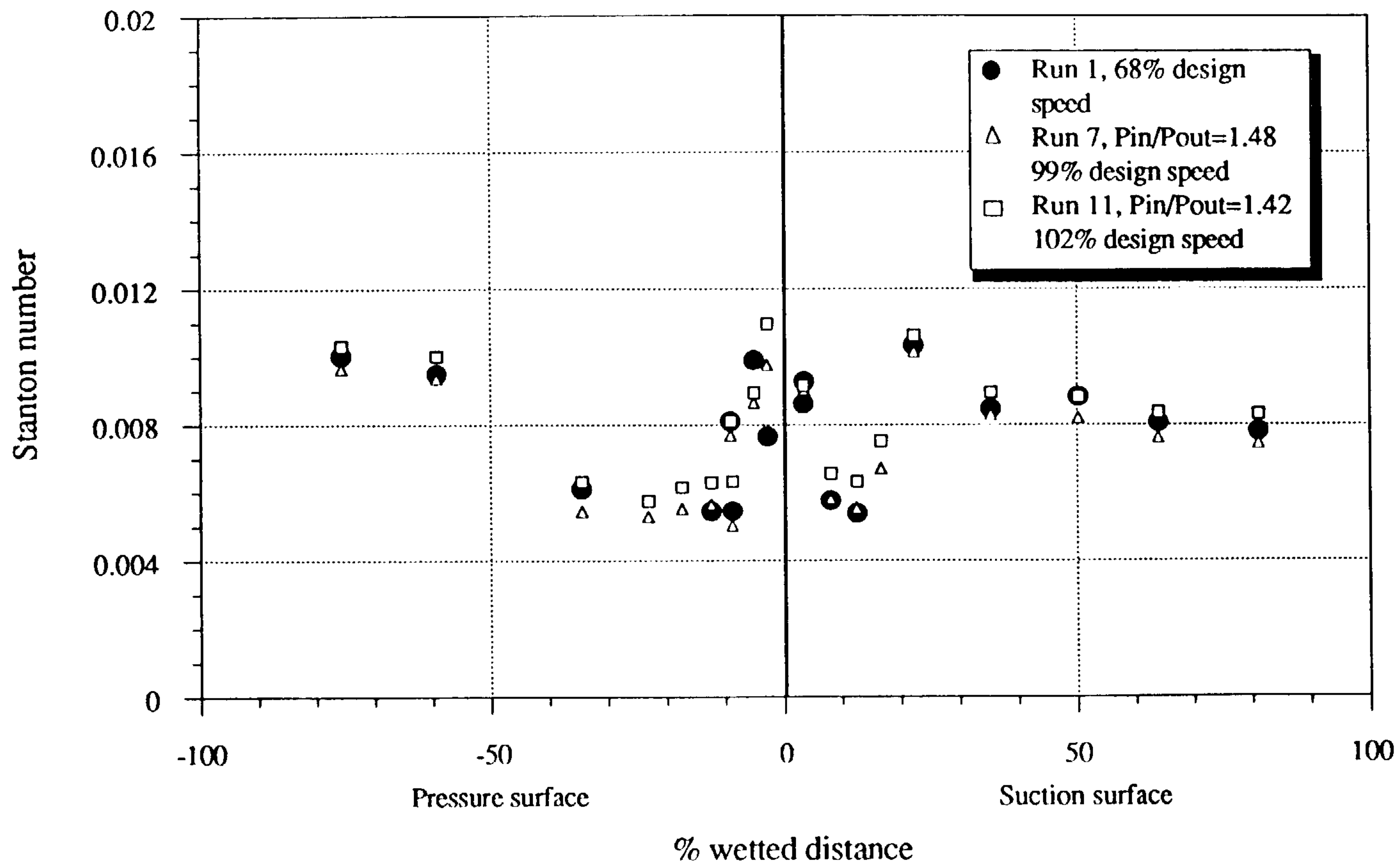

Figure 3.6.2--Stanton number distribution at 50% span on first blade, Re~250,000, comparison with off speed data.

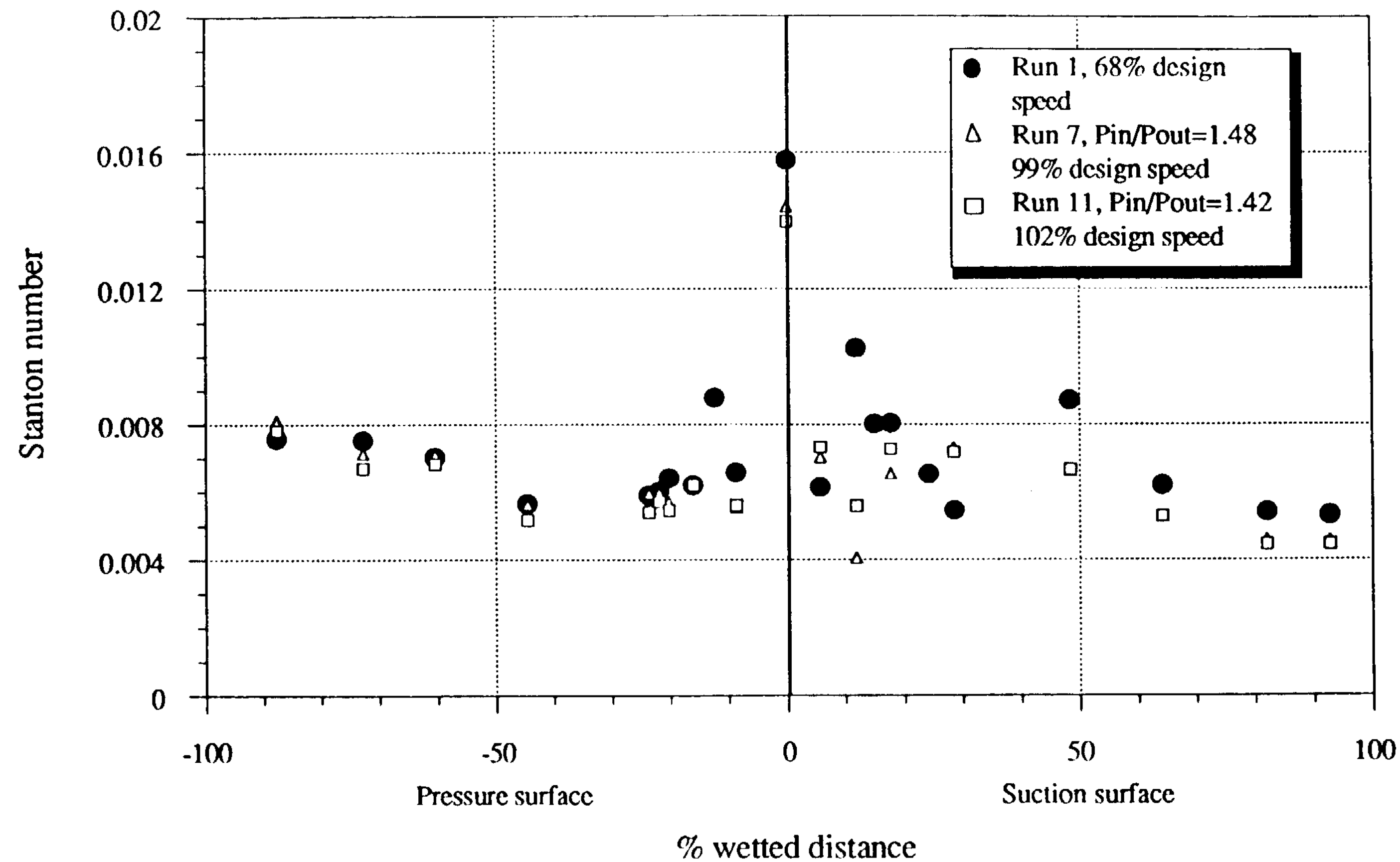

Figure 3.6.3--Stanton number distribution at 50% span on second vane, Re~250,000, comparison with off speed data.

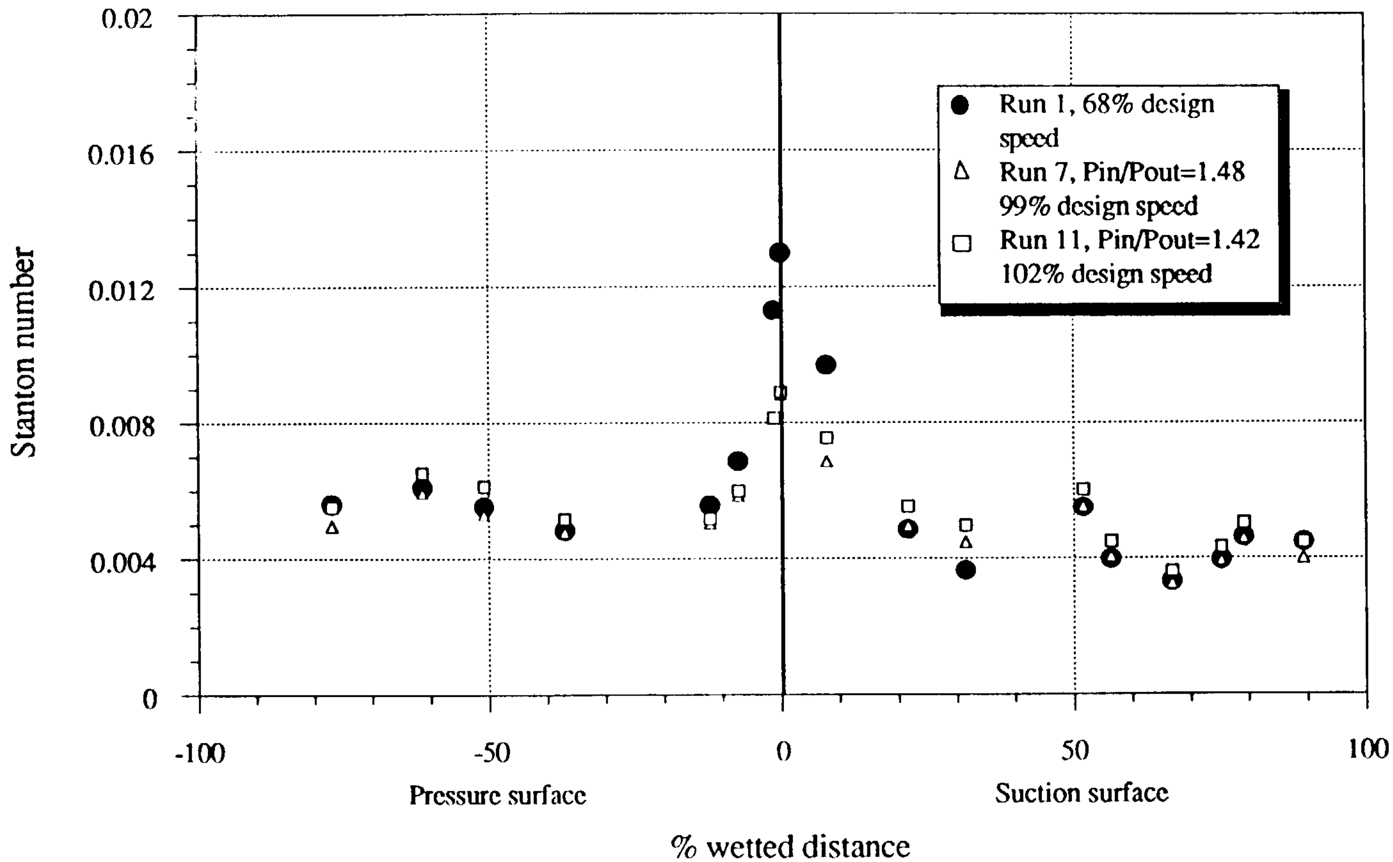

illustrates that in the vicinity of the leading edge, incidence angle has a noticeable influence on the magnitude of the Stanton number. Beyond 20% wetted distance on the pressure surface the influence of incidence angle is shown to be relatively small. For the suction surface at wetted distances less than 30%, the trend is not consistent apparently because of the transition location. At 50% wetted distance and beyond, the off-speed data are generally above the design speed data. Figure 3.6.3 presents the second vane Stanton number results. In the immediate region of the leading edge (5% to 10%), the off-design turbine speed appears to have an influence on the second vane Stanton number distribution. If there was going to be an influence, it is in this region that one would expect it to occur. However, on the second vane, the influence dies out much more rapidly than it did for the first blade, being essentially gone by about 5% wetted distance on the pressure surface and by 20% wetted distance on the suction surface.

3.7 Blade Platform, Tip and Shroud Results for Off-Design Speed

Figures 3.7.1 -3.7.3 present a comparison of the off speed (68% of design value) data with the design speed data for the blade platform, blade tip and the shroud, respectively. The data presented were obtained at the high Reynolds number at a stage pressure ratio of approximately 1.4 and 1.5. The results presented on Figure 3.7.1 for the platform illustrate that at each of the locations, the Stanton number results do not appear to be influenced by rotor speed. This is not surprising since both locations are sufficiently far from the stagnation point that incidence angle should not be important. Figure 3.7.2 compares the off speed and design speed tip region data. For this region, Metzger and Rued, 1989 have shown that blade relative motion should not have a significant influence on the average tip region heat transfer. At two measuring stations, the off speed results fall above the design speed values. However, at the third station, this is not true and thus the results are inconclusive. Figure 3.7.3 presents the time averaged shroud heat transfer results. The Stanton number is shown to have an increasing trend

Figure 3.7.1--Stanton number distribution on the blade platform, Re~250,000, comparison with off speed data.

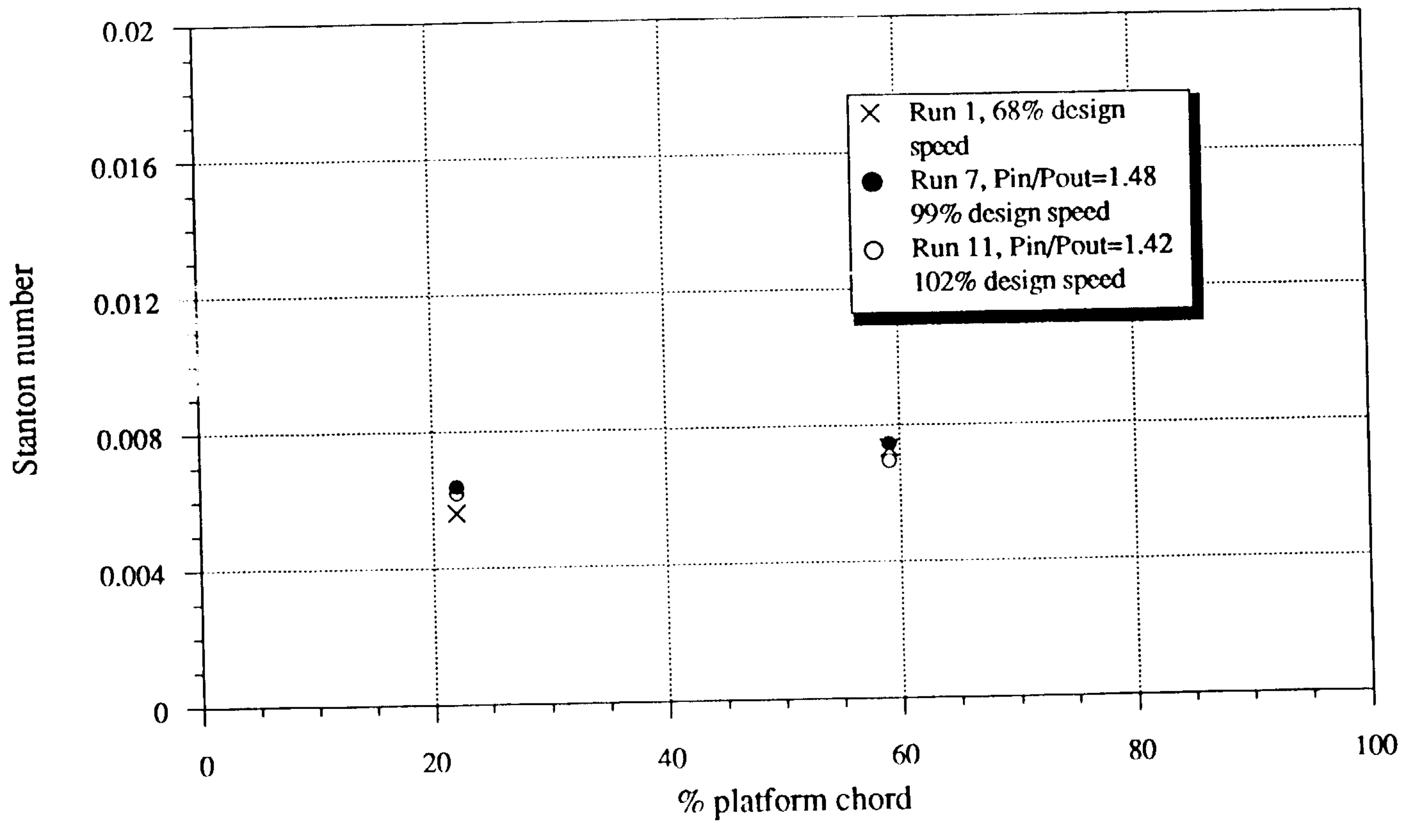

Figure 3.7.2--Stanton number distribution on the blade tip, Re~250,000, comparison with off speed data.

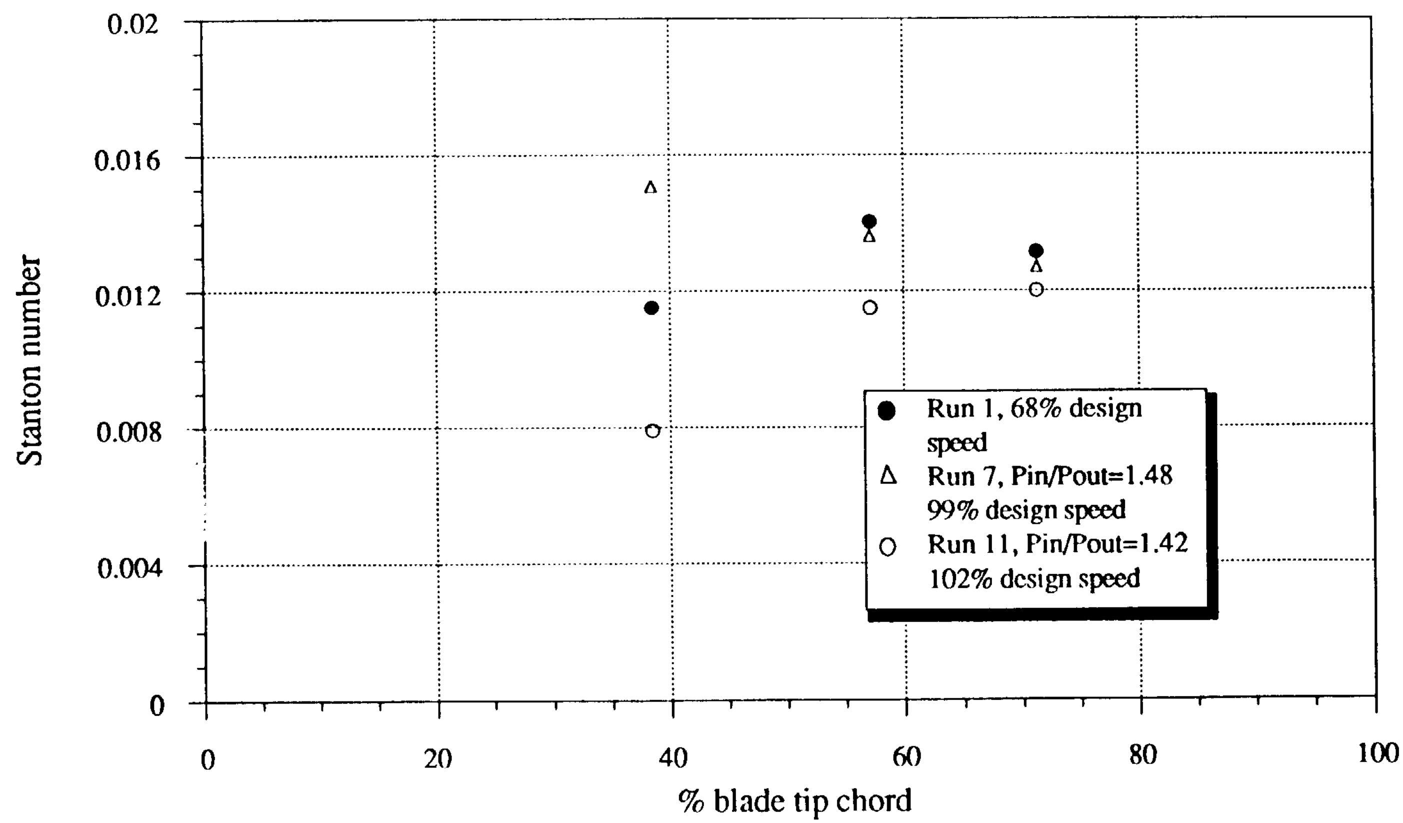

Figure 3.7.3--Stanton number distribution on the blade shroud, Re~250,000, comparison with off speed data.

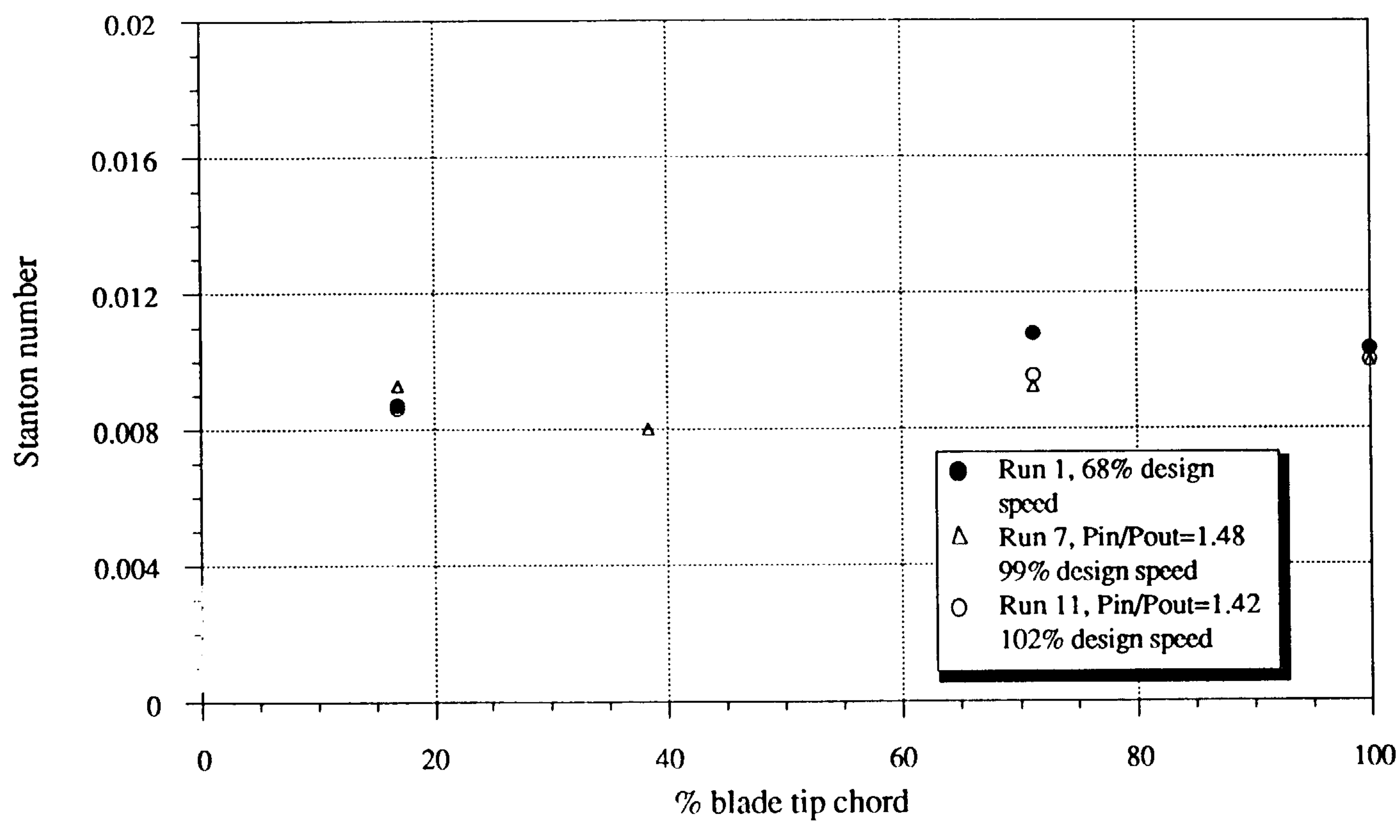

towards the blade trailing edge as would be anticipated because of the increasing driver pressure on the flow through the tip in moving from the leading edge towards the trailing edge. For a reduced rotor speed, a particular gage in the shroud would be exposed to the tip gap flow for a longer period of time (per rotor revolution) but it is also clear of the rotor tip for a longer period of time. The fraction of time for which the shroud gage is covered by the tip is the same as it is for the higher speed. If the gap flow is the same, then one would not expect to see a significant influence on Stanton number. However, because the influence of rotor speed on the blade surface pressure distribution in the tip region was not measured it is not possible to be certain that the tip flow was the same for both speeds and thus it is difficult to close the discussion of this point.

SECTION 4

CONCLUSIONS

Surface pressure and Stanton number distributions have been measured at selected locations on the first vane, first blade and second vane of a full two-stage turbine. The first vane and first blade pressure measurements have been compared with the prediction, but the agreement was not particularly good because of difficulties with the measurement. The measured Stanton number distributions at midspan for the first vane and the first blade have been compared with predictions obtained using a quasi-3D N-S code and a modified STAN5 technique. For the first vane, comparisons were presented for the fully turbulent case and for the transition case using two transition models (Mayle, 1991 and Dunham, 1972). At the low Reynolds number, the Mayle transition model and the fully turbulent prediction provided good agreement with the suction surface data. The fully turbulent, the Mayle transition model, and the Dunham transition model all provided good agreement with the suction surface data for the high Reynolds number case. The first vane pressure surface data were consistently underpredicted by all of the predictions. The sensitivity of the predictions to flow parameters such as turbulence intensity, coupled with the lack of agreement for the vane pressure surface heat transfer illustrates the importance of correctly modeling the actual flow field in any heat transfer analysis.

The first blade data were compared to N-S turbulent and N-S with the Mayle and Dullenkopf, 1989, 1990 intermittency model predictions. There is very little difference between the results of these two predictions. For the blade suction surface, the predictions were consistently above the data. The agreement between data and prediction for the pressure surface was reasonably good.

The surface of the blade used in these experiments appeared to be very rough. However, when the roughness density was accounted for, the analysis showed only a small increase in blade heat transfer due to surface roughness. The relatively good agreement between the measured and predicted rotor heat transfer supports this conclusion. In the analysis the effect of surface roughness is strongly dependent on Reynolds number. Consequently, for the actual SSME engine operating conditions the analysis predicts a significant increase in blade heat transfer due to surface roughness.

The second vane data were compared with N-S fully turbulent calculations and with a N-S solution including the Mayle and Dullenkopf intermittency model. For the suction surface, both calculations were generally conservative. However, for the pressure surface, the predicted Stanton number distributions were in good agreement with the experimental data.

The tip region was shown to exhibit high heat-transfer rates by comparison with the blade stagnation-point value. The shroud Stanton number values were less than the tip values, but higher than the platform values. Data were presented to illustrate the influence of off-design rotor speed on the vane and blade Stanton number distributions. The first vane Stanton number distribution was also not influenced by rotor speed. The tip and shroud distributions were not significantly influenced by rotor speed. However, both the first blade and the second vane were influenced by rotor speed in the vicinity of the leading edge. This influence persisted on the first blade over a greater portion of the surface than it did on the second vane.

REFERENCES

Abhari, R.S., Guenette, G.R., Epstein, A.H., and Giles, M.B., 1991, "Comparison of Time-Resolved Turbine Rotor Blade Heat Transfer Measurements and Numerical Calculations," ASME Paper No. 91-GT-268.

Adamczyk, J.J., 1985, "Model Equation for Simulating Flows in Multistage Turbomachinery," ASME Paper No. 85-GT-226.

Adamczyk, J.J., 1986, "A Model for Closing the Inviscid Form of the Average-Passage Equation System," ASME Paper No. 86-GT-227.

Allen, H.W. and Kofskey, M.G., 1955, "Visualization Study of Secondary Flows in Turbine Rotor Tip Regions," NACA TN 3519.

Bindon, J.P., 1986, "Visualization of Axial Turbine Tip Clearance Using a Linear Cascade," Report No. CUED/A-Turbo TR122, Whittle Laboratory, Cambridge University, United Kingdom.

Blair, M.F., Dring, R.P., and Joslyn, H.D., 1988, "The Effects of Turbulence and Stator/Rotor Interaction on Turbine Heat Transfer, Part I: Design Operating Conditions," ASME Paper No. 88-GT-125.

Blair, M.F. and Anderson, O.L., 1989, "The Effects of Reynolds Number, Rotor Incidence Angle and Surface Roughness on the Heat Transfer Distribution in a Large-Scale Turbine Rotor Passage," UTRC Report No. UTRC-R89-957852-24.

Blair, M.F. and Anderson, O.L., 1992, "An Experimental Study of Heat Transfer in a Large Scale Turbine Rotor Passage," 37th International Gas Turbine Conference, Paper GT-92-.

Booth, T.C., Dodge, P.R. and Hepworth, H.K., 1982, "Rotor-Tip Leakage: Part I - Basic Methodology," Journal of Engineering for Power, Vol. 104, pp. 154-161.

Boyle, R.J., 1991, "Navier-Stokes Analysis of Turbine Blades Heat Transfer," Journal of Turbomachinery, pp. 392-403.

Boyle, R.J. and Civinskas, K.C., 1991, "Two-Dimensional Navier-Stokes Heat Transfer Analysis for Rough Turbine Blades," AIAA/SAE/ASME 27th Joint Propulsion Conference, Paper No. AIAA-91-2129.

Chima, R.V., 1986, "Development of an Explicit Multigrid Algorithm for Quasi-Three-Dimensional Flows in Turbomachinery", AIAA Paper No. 86-0032, NASA TM-87128.

Civinskas, K.C., Boyle, R.J. and McConnaughey, H.V., 1988, "Impact of ETO Propellants on the Aerothermodynamic Analyses of Propulsion Components," AIAA/ASME/SAE/ASEE 24th Joint Propulsion Conference, Paper No. AIAA-88-3091.

Crawford, M.E. and Kays, W.M., 1976, "STAN5 - A Program for Numerical Computation of Two-Dimensional Internal and External Boundary-Layer Flows," NASA CR-2742.

Dring, R.P. and Joslyn, H.D., 1986, "Through-Flow Analysis of a Multi-Stage Compressor, Part I - Aerodynamic Input," ASME Paper No. 86-GT-13.

Dunham, J. 1972, "Predictions of Boundary Layer Transition on Tubomachinery Blades", AGARD-AG-164.

Dunn, M.G. and Stoddard, F.J., "Measurement of Heat Transfer Rate to a Gas Turbine Stator," ASME Journal of Engineering for Power, Vol. 101, No. 2, April 1979.

Dunn, M.G. and Hause, A., 1982, "Measurement of Heat Flux and Pressure in a Turbine Stage," ASME Journal of Engineering for Power, Vol. 104, pp. 215-223.

Dunn, M.G., Rae, W.J. and Holt, J.L., 1984a, "Measurement and Analysis of Heat Flux Data in a Turbine Stage: Part I: Description of Experimental Apparatus and Data Analysis," Journal of Engineering for Power, Trans. ASME, Vol. 106, pp. 229-240.

Dunn, M.G., Rae, W.J., and Holt, J.L., 1984, "Measurement and Analyses of Heat Flux Data in a Turbine Stage: Part II - Discussion of Results and Comparison with Predictions," ASME Journal of Engineering for Gas Turbines and Power, Vol. 106, pp. 234-240.

Dunn, M.G., Martin, H.L., and Stanek, M.J., 1986, "Heat-Flux and Pressure Measurements and Comparison with Prediction for a Low Aspect Ratio Turbine Stage," ASME Journal of Turbomachinery, Vol. 108, pp. 108-115.

Dunn, M.G., 1986, "Heat-Flux Measurements for the Rotor of a Full-Stage Turbine: Part I - Time-Averaged Results," Journal of Turbomachinery, Vol. 108, pp. 90-97.

Dunn, M.G., George, W.K., Rae, W.J., Woodward, S.H., Moller, J.C., and Seymour, P.J., 1986, "Heat-Flux Measurments for the Rotor of a Full-Stage Turbine: Part II-Description of Analysis Technique and Typical Time-Resolved Measurements", Journal of Turbomachinery, Vol. 108, pp. 98-107.

Dunn, M.G. and Chupp, R.E., 1988, "Time-Averaged Heat-Flux Distributions and Comparison with Prediction for the Teledyne 702 hp Turbine Stage," ASME Journal of Turbomachinery, Vol. 110, pp. 51-56.

Dunn, M.G. and Chupp, R.E., 1989, "Influence of Vane/Blade Spacing and Injection on Stage Heat-Flux Distributions," AIAA Journal of Propulsion and Power, Vol. 5, No. 2, pp. 212-200.

Dunn, M.G., Seymour, P.J., Woodward, S.H., George, W.K., and Chupp, R.E., 1989, "Phase-Resolved Heat-Flux Measurements on the Blade of a Full-Scale Rotating Turbine", Journal of Turbomachinery, Vol. 111, pp. 8-19.

Dunn, M.G., Bennett, W., Delaney, R., and Rao, K., 1990(a), "Investigation of Unsteady Flow Through a Transonic Turbine Stage: Data/Prediction Comparison for Time-Averaged and Phase-Resolved Pressure Data," AIAA/SAE/ASME/ASEE 26th Joint Propulsion Conference, Orlando, FL, AIAA Paper No. 90-2409 (see also ASME J. of Turbomachinery, Vol. 114, pp. 91-99).

Dunn, M.G., 1989, "Phase and Time-Resolved Measurements of Unsteady Heat Transfer and Pressure in a Full-Stage Rotating Turbine," ASME Paper 89-GT-135.

Dunn, M.G. 1990, "Heat Transfer and Pressure Measurements for the SSME Fuel-Side Turbopump", Proceedings of the NASA 1990 Earth-to-Orbit Conference, Marshall Space Flight Center, AL.

Epstein, A.H., Guenette, G.R., Norton, R.J.G. and Yuzhang, C., 1985, "Time Resolved Measurements of a Turbine Rotor Stationary Tip Casing Pressure and Heat Transfer Field," AIAA Paper No. 85-1220.

Gaugler, R.E., 1981, "Some Modifications to, and Operating Experiences with, the Two-Dimensional Finite-Difference, Boundary-Layer Code STAN5," ASME Paper No. 81-GT-89.

George, W.K., Rae, W.J., and Woodward, S.H., 1991, "An Evaluation of Analog and Numerical Techniques for Unsteady Heat Transfer Measurements with Thin-Film Gauges in Transient Facilities", Experimental Thermal and Fluid Sciences, Vol. 4, pp. 333-342.

Giles, M.B., 1988, "Calculation of Unsteady Wake Rotor Interaction," AIAA Journal of Propulsion and Power, Vol. 4, No. 4, pp. 356-362.

Hah, C., 1984, "A Navier-Stokes Analysis of Three-Dimensional Turbulent Flows Inside Turbine Blade Rows at Design and Off-Design Conditions," Journal of Engineering for Power, Trans. ASME, 106, pp. 421-429.

Katsanis, T., 1969, "FORTRAN Program for Calculating Transonic Velocities on a Blade-to-Blade Stream Surface of a Turbomachine," NASA TN D-5427.

Katsanis, T and McNally, W.D., 1977, "Revised FORTRAN Program for Calculating Velocities and Streamlines on the Hub-Shroud Mid-Channel Stream Surface of an Axial-, Radial-, or Mixed-Flow Turbomachine or Annular Duct," Vol. I, User's Manual, Vol. II - Programmer's Manual," NASA TN D-8430, 8431.

Kline, S.J. and McClintock, 1953, "Describing Uncertainties in Single-Sampled Experiments", Mechanical Engineering, Vol. 75, pp. 3-8.

Mayle, R.E., 1991, "The Role of Laminar-Turbulent Transition in Gas Turbine Engines", paper presented at the 36th International Gas Turbine Conference, Paper No. 91-GT-261, Orlando, FL.

Mayle, R.E. and Dullenkopf, K., 1989, "A Theory of Wake Induced Transition", ASME J. of Turbomachinery, Vol. 112, pp. 188-195.

Mayle, R.E. and Dullenkopf, K., 1990, "More on the Turbulent-Strip Theory for Wake Induced Transition", paper presented at the 35th International Gas Turbine Conference, Paper No. 90-GT-137, Brussels, Belgium.

Mayle, R.E. and Metzger, D.E., 1982, "Heat Transfer at the Tip of an Unshrouded Turbine Blade," Proceedings, Seventh International Heat Transfer Conference, Vol. 3, pp. 87-92.

McFarland, E.R., 1984, "A Rapid Blade-to-Blade Solution for use in Turbomachinery Design," Journal of Engineering for Gas Turbines and Power, Vol. 105, No. 2, pp. 376-382.

Metzger, D.E., Dunn, M.G., and Hah, C., 1990, "Turbine Tip and Shroud Heat Transfer," Paper presented at the 35th ASME International Gas Turbine and Aerospace Congress, Paper No. 90-GT-333, Brussels, Belgium.

Metzger, D.E. and Rued, K., 1989, "The Influence of Turbine Clearance Gap Leakage on Flowpath Velocities and Heat Transfer, Part I: Sink Flow Effects on Blade Pressure Sides," Journal of Turbomachinery, Trans. ASME, Vol. 111, pp. 284-292.

McNally, W.D., 1970, "Fortran Program for Calculating Compressible Laminar and Turbulent Boundary Layers in Arbitrary Pressure Gradients," NASA TND-5681.

Moore, J. and Tilton, J.S., 1988, "Tip Leakage Flow in a Linear Turbine Cascade," Journal of Turbomachinery, Trans. ASME, Vol. 110, pp. 18-26.

Nealy, D.A., Milele, M.S., Hylton, L.D., and Gladden, H.J., 1984, "Measurements of Heat Transfer Distribution Over the Surfaces of Highly Loaded Turbine Nozzle Guide Vanes", J. of Engineering for Gas Turbines and Power, Vol. 106, pp. 149-158.

Rae, W.J., Taulbee, D.B., Civinskas, K.C., and Dunn, M.G., 1988, "Turbine-Stage Heat Transfer: Comparison of Short Duration Measurements with State-of-the-Art Predictions", Journal of Propulsion and Power, Vol. 4, No. 6, pp. 541-548.

Rai, M.M., 1987, "Navier-Stokes Simulations of Rotor/Stator Interaction Using Patched and Overlaid Grids," Journal of Propulsion, No. 3, pp. 387-396.

Rai, M.M. and Madavan, K.K., 1988, "Multi Airfoil Navier Stokes Simulation of Turbine Rotor-Stator Interaction," AIAA Paper No. 88-0361.

Rao, K.V. and Delaney, R.A., 1990, "Investigation of Unsteady Flow Through a Transonic Turbine Stage, Part I - Analysis," AIAA/SAE/ASME/ASEE 26th Joint Propulsion Conference, Orlando, FL, AIAA Paper No. 90-2408.

Taulbee, D.B., Tran, L., and Dunn, M.G., 1988, "Stagnation Point and Surface Heat Transfer for a Turbine Stage: Prediction and Comparison with Data", ASME 33rd International Gas Turbine Conference, Paper 88-GT-30, Amsterdam.

Traci, R.M. and Wilcox, D.C., 1975, "Freestream Turbulence Effects on Stagnation Heat Transfer," AIAA Journal, Vol. 13, No. 7, pp. 890-896.

Tran, L and Taulbee, D.B., 1991, "Prediction of Unsteady Rotor-Surface Pressure and Heat Transfer from Wake Passings", ASME 36th International Gas Turbine Conference, Paper No. 91-GT-267, Orlando, Florida.

Wadia, A.R. and Booth, T.C., 1982, "Rotor-Tip Leakage: Part II - Design Optimization Through Viscous Analysis and Experiment," Journal of Engineering for Power, Trans. ASME, Vol. 104, 1982, pp. 162-169.

APPENDIX

A.1 Vane and Blade Coordinates

A.1.1 First Nozzle Coordinates

First nozzle, hub

	x [in]	y[in]
1	0.00013213	0.85099
2	0.00052741	0.84738
3	0.0011839	0.84380
4	0.0020981	0.84027
5	0.0032653	0.83683
6	0.0046793	0.83347
7	0.0063326	0.83023
8	0.0082165	0.82712
9	0.010321	0.82415
10	0.012636	0.82134
11	0.015147	0.81870
12	0.017843	0.81626
13	0.020710	0.81402
14	0.023731	0.81199
15	0.026891	0.81018
16	0.030173	0.80861
17	0.033561	0.80728
18	0.037036	0.80620
19	0.040580	0.80538
20	0.057465	0.80198
21	0.074350	0.79836
22	0.091235	0.79453
23	0.10812	0.79048
24	0.12500	0.78620
25	0.14189	0.78169
26	0.15877	0.77696
27	0.17566	0.77199
28	0.19254	0.76678
29	0.20943	0.76133
30	0.22631	0.75564
31	0.24320	0.74969
32	0.26008	0.74349
33	0.27697	0.73703
34	0.29385	0.73031
35	0.31074	0.72331
36	0.32762	0.71603
37	0.34451	0.70847
38	0.36139	0.70062
39	0.37828	0.69246
40	0.39516	0.68401
41	0.41205	0.67523
42	0.42893	0.66613
43	0.44582	0.65670
44	0.46270	0.64692
45	0.47959	0.63678
46	0.49647	0.62627
47	0.51336	0.61539
48	0.53024	0.60410
49	0.54713	0.59240
50	0.56401	0.58027
51	0.58090	0.56769
52	0.59778	0.55464
53	0.61467	0.54110
54	0.63155	0.52705
55	0.64844	0.51244
56	0.66532	0.49727
57	0.68220	0.48148
58	0.69909	0.46504
59	0.71597	0.44791
60	0.73286	0.43004
61	0.74974	0.41137
62	0.76663	0.39184
63	0.78351	0.37136
64	0.80040	0.34986
65	0.81728	0.32721
66	0.83417	0.30331
67	0.85105	0.27798
68	0.86794	0.25103
69	0.88482	0.22221
70	0.90171	0.19120
71	0.91859	0.15755
72	0.93547	0.12064
73	0.95226	0.079845
74	0.95938	0.061524
75	0.96650	0.043204
76	0.97361	0.024884
77	0.98073	0.0065631
78	0.98230	0.0038427
79	0.98463	0.0017172
80	0.98750	0.00039538
81	0.99063	4.5100e-06
82	0.99374	0.00058252
83	0.99652	0.0020755
84	0.99872	0.0043429
85	1.0001	0.0071712
86	1.0006	0.010294
87	1.0006	0.011143
88	1.0005	0.011986
89	1.0003	0.012818
90	1.0001	0.013632
91	0.98945	0.044610
92	0.97884	0.075588
93	0.96823	0.10657

94	0.95762	0.13754
95	0.94701	0.16852
96	0.93640	0.19950
97	0.92579	0.23047
98	0.91517	0.26145
99	0.90456	0.29243
100	0.89579	0.31792
101	0.88691	0.34341
102	0.87803	0.36860
103	0.86915	0.39346
104	0.86027	0.41799
105	0.85139	0.44216
106	0.84251	0.46596
107	0.83363	0.48935
108	0.82475	0.51232
109	0.81587	0.53485
110	0.80700	0.55689
111	0.79812	0.57842
112	0.78924	0.59939
113	0.78036	0.61975
114	0.76852	0.64546
115	0.75657	0.66951
116	0.74463	0.69194
117	0.73269	0.71293
118	0.72075	0.73262
119	0.70881	0.75107
120	0.69686	0.76840
121	0.68492	0.78470
122	0.67298	0.80004
123	0.66104	0.81450
124	0.64910	0.82813
125	0.63716	0.84099
126	0.62521	0.85311
127	0.61327	0.86455
128	0.60133	0.87533
129	0.58939	0.88549
130	0.57745	0.89505
131	0.56551	0.90404
132	0.55357	0.91249
133	0.54162	0.92041
134	0.52968	0.92783
135	0.51774	0.93476
136	0.50580	0.94121
137	0.49386	0.94720
138	0.48192	0.95275
139	0.46998	0.95787
140	0.45803	0.96256
141	0.44609	0.96683
142	0.43415	0.97070
143	0.42221	0.97418
144	0.41027	0.97726
145	0.39833	0.97997
146	0.38638	0.98230
147	0.37444	0.98426
148	0.36250	0.98585
149	0.35056	0.98708
150	0.33862	0.98796
151	0.32668	0.98848
152	0.31474	0.98865
153	0.30462	0.98856
154	0.29439	0.98827
155	0.28417	0.98779
156	0.27395	0.98712
157	0.26373	0.98626
158	0.25351	0.98521
159	0.24329	0.98396
160	0.23307	0.98252
161	0.22285	0.98088
162	0.21263	0.97903
163	0.20241	0.97698
164	0.19219	0.97472
165	0.18197	0.97224
166	0.17174	0.96954
167	0.16152	0.96661
168	0.15130	0.96344
169	0.14108	0.96003
170	0.13086	0.95635
171	0.12064	0.95241
172	0.11042	0.94819
173	0.10020	0.94367
174	0.089978	0.93883
175	0.079757	0.93365
176	0.069536	0.92810
177	0.059316	0.92215
178	0.049095	0.91577
179	0.038874	0.90891
180	0.028653	0.90151
181	0.018432	0.89349
182	0.016656	0.89197
183	0.014952	0.89037
184	0.013325	0.88869
185	0.011778	0.88693
186	0.010314	0.88511
187	0.0089374	0.88322
188	0.0076500	0.88126
189	0.0064551	0.87925
190	0.0053553	0.87719
191	0.0043528	0.87507
192	0.0034499	0.87292
193	0.0026486	0.87072
194	0.0019505	0.86849
195	0.0013573	0.86622
196	0.00087012	0.86393
197	0.00049012	0.86163
198	0.00021811	0.85930
199	5.4660e-05	0.85697
200	1.4000e-07	0.85463

First nozzle, midspan

	x [in]	y[in]
1	0.00013143	0.87560
2	0.00052459	0.87200
3	0.0011775	0.86843
4	0.0020869	0.86491
5	0.0032478	0.86147
6	0.0046542	0.85813
7	0.0062986	0.85489
8	0.0081725	0.85179
9	0.010266	0.84882
10	0.012568	0.84602
11	0.015066	0.84339
12	0.017748	0.84094
13	0.020599	0.83870
14	0.023603	0.83667
15	0.026747	0.83486
16	0.030012	0.83329
17	0.033381	0.83195
18	0.036838	0.83086
19	0.040363	0.83003
20	0.057963	0.82639
21	0.075563	0.82253
22	0.093164	0.81843
23	0.11076	0.81408
24	0.12836	0.80950
25	0.14596	0.80467
26	0.16356	0.79959
27	0.18117	0.79426
28	0.19877	0.78868
29	0.21637	0.78283
30	0.23397	0.77673
31	0.25157	0.77035
32	0.26917	0.76370
33	0.28677	0.75678
34	0.30437	0.74957
35	0.32197	0.74207
36	0.33957	0.73427
37	0.35717	0.72618
38	0.37477	0.71778
39	0.39237	0.70906
40	0.40997	0.70002
41	0.42757	0.69065
42	0.44517	0.68093
43	0.46277	0.67087
44	0.48037	0.66044
45	0.49797	0.64964
46	0.51557	0.63846
47	0.53317	0.62687
48	0.55077	0.61488
49	0.56837	0.60246
50	0.58597	0.58959
51	0.60357	0.57627
52	0.62117	0.56245
53	0.63877	0.54814
54	0.65637	0.53329
55	0.67397	0.51789
56	0.69157	0.50191
57	0.70917	0.48530
58	0.72677	0.46804
59	0.74437	0.45009
60	0.76197	0.43139
61	0.77957	0.41189
62	0.79717	0.39153
63	0.81477	0.37025
64	0.83237	0.34795
65	0.84997	0.32454
66	0.86757	0.29991
67	0.88517	0.27391
68	0.90277	0.24636
69	0.92037	0.21706
70	0.93796	0.18573
71	0.95556	0.15198
72	0.97316	0.11533
73	0.99066	0.075653
74	0.99808	0.058299
75	1.0055	0.040945
76	1.0129	0.023591
77	1.0203	0.0062364
78	1.0219	0.0036896
79	1.0242	0.0016451
80	1.0271	0.00037010
81	1.0302	6.9900e-06
82	1.0333	0.00059956
83	1.0360	0.0020971
84	1.0382	0.0043615
85	1.0396	0.0071818
86	1.0401	0.010294
87	1.0400	0.011221
88	1.0399	0.012141
89	1.0397	0.013047
90	1.0394	0.013931
91	1.0284	0.043257
92	1.0173	0.072584
93	1.0063	0.10191
94	0.99527	0.13124
95	0.98424	0.16056
96	0.97320	0.18989
97	0.96217	0.21921
98	0.95113	0.24853
99	0.94010	0.27786
100	0.93097	0.30205
101	0.92174	0.32639
102	0.91250	0.35059
103	0.90327	0.37464
104	0.89403	0.39854
105	0.88480	0.42227

106	0.87557	0.44583
107	0.86633	0.46921
108	0.85710	0.49239
109	0.84786	0.51537
110	0.83863	0.53813
111	0.82940	0.56065
112	0.82016	0.58292
113	0.81092	0.60474
114	0.79861	0.63284
115	0.78619	0.65993
116	0.77377	0.68587
117	0.76134	0.71073
118	0.74892	0.73442
119	0.73650	0.75655
120	0.72408	0.77724
121	0.71166	0.79658
122	0.69924	0.81467
123	0.68681	0.83160
124	0.67439	0.84745
125	0.66197	0.86227
126	0.64955	0.87615
127	0.63713	0.88912
128	0.62471	0.90125
129	0.61229	0.91258
130	0.59987	0.92316
131	0.58745	0.93301
132	0.57503	0.94219
133	0.56261	0.95072
134	0.55019	0.95863
135	0.53777	0.96595
136	0.52535	0.97271
137	0.51293	0.97894
138	0.50051	0.98465
139	0.48809	0.98986
140	0.47567	0.99460
141	0.46325	0.99888
142	0.45083	1.0027
143	0.43840	1.0061
144	0.42598	1.0091
145	0.41356	1.0117
146	0.40114	1.0140
147	0.38872	1.0158
148	0.37630	1.0173
149	0.36388	1.0185
150	0.35146	1.0193
151	0.33904	1.0197
152	0.32662	1.0199
153	0.31609	1.0197
154	0.30546	1.0194
155	0.29483	1.0188
156	0.28420	1.0180
157	0.27357	1.0170
158	0.26294	1.0158
159	0.25231	1.0144
160	0.24168	1.0127
161	0.23105	1.0109
162	0.22042	1.0088
163	0.20979	1.0065
164	0.19916	1.0040
165	0.18853	1.0012
166	0.17789	0.99829
167	0.16726	0.99509
168	0.15663	0.99166
169	0.14600	0.98797
170	0.13537	0.98403
171	0.12474	0.97981
172	0.11411	0.97532
173	0.10348	0.97052
174	0.092848	0.96541
175	0.082217	0.95996
176	0.071586	0.95414
177	0.060955	0.94792
178	0.050325	0.94126
179	0.039694	0.93412
180	0.029063	0.92642
181	0.018432	0.91809
182	0.016656	0.91656
183	0.014952	0.91496
184	0.013325	0.91328
185	0.011778	0.91153
186	0.010314	0.90970
187	0.0089374	0.90781
188	0.0076500	0.90586
189	0.0064551	0.90385
190	0.0053553	0.90178
191	0.0043528	0.89967
192	0.0034499	0.89751
193	0.0026486	0.89532
194	0.0019505	0.89308
195	0.0013573	0.89082
196	0.00087012	0.88853
197	0.00049013	0.88623
198	0.00021811	0.88390
199	5.4660e-05	0.88157
200	1.4000e-07	0.87923

First nozzle, tip

	x [in]	y [in]
1	0.00013073	0.90027
2	0.00052177	0.89667
3	0.0011712	0.89311
4	0.0020757	0.88961
5	0.0032303	0.88618
6	0.0046291	0.88284
7	0.0062647	0.87961
8	0.0081285	0.87651
9	0.010211	0.87355
10	0.012500	0.87075
11	0.014985	0.86812
12	0.017652	0.86568
13	0.020488	0.86344
14	0.023476	0.86140
15	0.026603	0.85959
16	0.029850	0.85801
17	0.033202	0.85667
18	0.036639	0.85557
19	0.040145	0.85472
20	0.058460	0.85086
21	0.076775	0.84674
22	0.095090	0.84237
23	0.11341	0.83774
24	0.13172	0.83285
25	0.15004	0.82769
26	0.16835	0.82227
27	0.18667	0.81658
28	0.20498	0.81062
29	0.22330	0.80438
30	0.24161	0.79786
31	0.25993	0.79105
32	0.27824	0.78395
33	0.29656	0.77656
34	0.31487	0.76887
35	0.33319	0.76087
36	0.35150	0.75256
37	0.36982	0.74393
38	0.38813	0.73498
39	0.40645	0.72570
40	0.42476	0.71607
41	0.44308	0.70610
42	0.46139	0.69577
43	0.47971	0.68507
44	0.49802	0.67400
45	0.51634	0.66254
46	0.53465	0.65068
47	0.55297	0.63840
48	0.57128	0.62570
49	0.58960	0.61255
50	0.60791	0.59895
51	0.62623	0.58487
52	0.64454	0.57030
53	0.66286	0.55520
54	0.68117	0.53957
55	0.69949	0.52337
56	0.71780	0.50657
57	0.73612	0.48915
58	0.75443	0.47107
59	0.77275	0.45229
60	0.79106	0.43276
61	0.80938	0.41243
62	0.82769	0.39125
63	0.84601	0.36915
64	0.86432	0.34606
65	0.88264	0.32188
66	0.90095	0.29652
67	0.91927	0.26984
68	0.93759	0.24171
69	0.95590	0.21192
70	0.97422	0.18026
71	0.99253	0.14642
72	1.0108	0.11002
73	1.0291	0.071462
74	1.0368	0.055074
75	1.0445	0.038686
76	1.0522	0.022298
77	1.0599	0.0059098
78	1.0615	0.0035365
79	1.0638	0.0015731
80	1.0666	0.00034483
81	1.0697	9.4700e-06
82	1.0728	0.00061660
83	1.0755	0.0021187
84	1.0777	0.0043802
85	1.0791	0.0071925
86	1.0795	0.010294
87	1.0795	0.011300
88	1.0794	0.012297
89	1.0791	0.013276
90	1.0788	0.014229
91	1.0673	0.041904
92	1.0558	0.069580
93	1.0444	0.097256
94	1.0329	0.12493
95	1.0215	0.15261
96	1.0100	0.18028
97	0.99853	0.20796
98	0.98707	0.23564
99	0.97561	0.26331
100	0.96612	0.28622
101	0.95653	0.30942
102	0.94694	0.33264
103	0.93735	0.35589
104	0.92776	0.37916
105	0.91816	0.40247

106	0.90857	0.42580
107	0.89898	0.44917
108	0.88939	0.47258
109	0.87980	0.49602
110	0.87020	0.51950
111	0.86061	0.54302
112	0.85102	0.56657
113	0.84143	0.58987
114	0.82864	0.62037
115	0.81574	0.65049
116	0.80284	0.67992
117	0.78994	0.70864
118	0.77705	0.73632
119	0.76415	0.76214
120	0.75125	0.78617
121	0.73835	0.80855
122	0.72545	0.82939
123	0.71255	0.84878
124	0.69966	0.86684
125	0.68676	0.88363
126	0.67386	0.89925
127	0.66096	0.91376
128	0.64806	0.92724
129	0.63516	0.93974
130	0.62226	0.95133
131	0.60936	0.96205
132	0.59647	0.97195
133	0.58357	0.98109
134	0.57067	0.98949
135	0.55777	0.99722
136	0.54487	1.0043
137	0.53197	1.0107
138	0.51907	1.0166
139	0.50617	1.0219
140	0.49327	1.0267
141	0.48038	1.0310
142	0.46748	1.0348
143	0.45458	1.0382
144	0.44168	1.0411
145	0.42878	1.0436
146	0.41588	1.0457
147	0.40298	1.0475
148	0.39008	1.0489
149	0.37718	1.0499
150	0.36429	1.0506
151	0.35139	1.0511
152	0.33849	1.0512
153	0.32756	1.0510
154	0.31652	1.0506
155	0.30548	1.0499
156	0.29444	1.0490
157	0.28340	1.0479
158	0.27236	1.0465
159	0.26132	1.0448
160	0.25028	1.0430
161	0.23924	1.0409
162	0.22820	1.0386
163	0.21716	1.0361
164	0.20612	1.0333
165	0.19507	1.0303
166	0.18403	1.0271
167	0.17299	1.0237
168	0.16195	1.0200
169	0.15091	1.0160
170	0.13987	1.0118
171	0.12883	1.0073
172	0.11779	1.0025
173	0.10675	0.99746
174	0.095713	0.99208
175	0.084673	0.98635
176	0.073633	0.98026
177	0.062593	0.97377
178	0.051553	0.96683
179	0.040513	0.95940
180	0.029472	0.95141
181	0.018432	0.94276
182	0.016656	0.94123
183	0.014952	0.93963
184	0.013325	0.93795
185	0.011778	0.93619
186	0.010314	0.93437
187	0.0089374	0.93248
188	0.0076500	0.93053
189	0.0064551	0.92851
190	0.0053553	0.92645
191	0.0043528	0.92434
192	0.0034499	0.92218
193	0.0026486	0.91998
194	0.0019505	0.91775
195	0.0013573	0.91548
196	0.00087013	0.91320
197	0.00049013	0.91089
198	0.00021811	0.90856
199	5.4670e-05	0.90623
200	1.5000e-07	0.90389

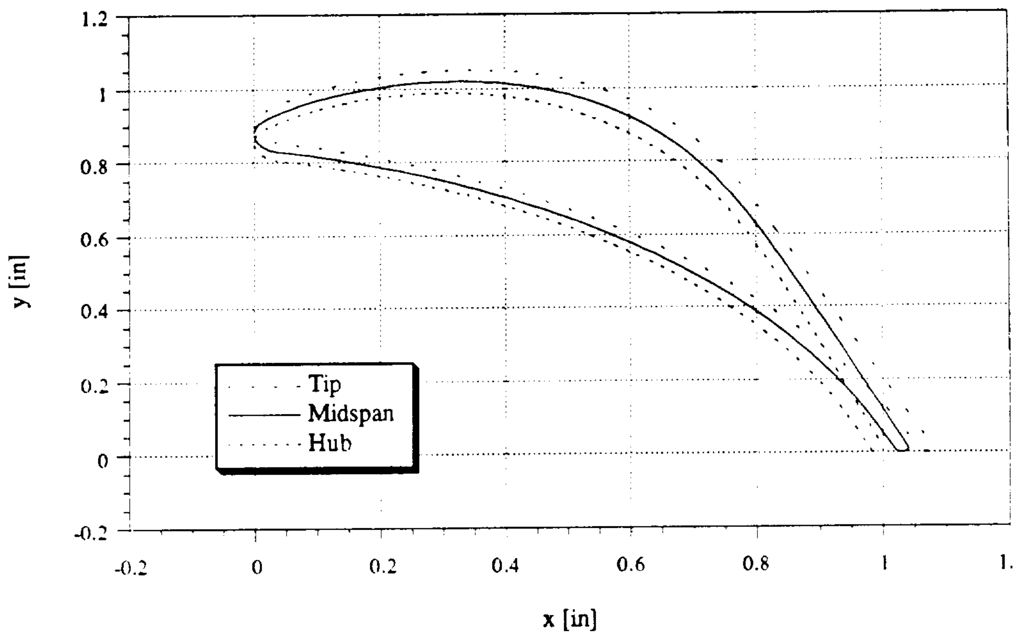

Figure A..1.1--First nozzle: tip, midspan, and hub

A.1.2 First Rotor Coordinates

First rotor, hub

	x [in]	y[in]
1	0.12085	0.22903
2	0.12139	0.22218
3	0.12192	0.21942
4	0.12246	0.21733
5	0.12299	0.21558
6	0.12352	0.21406
7	0.12406	0.21270
8	0.12459	0.21146
9	0.12513	0.21031
10	0.12556	0.20943
11	0.13846	0.18586
12	0.15136	0.16523
13	0.16426	0.14691
14	0.17716	0.13049
15	0.19007	0.11568
16	0.20297	0.10227
17	0.21587	0.090094
18	0.22877	0.079021
19	0.24167	0.068951
20	0.25457	0.059799
21	0.26747	0.051497
22	0.28037	0.043990
23	0.29327	0.037227
24	0.30617	0.031170
25	0.31907	0.025784
26	0.33197	0.021040
27	0.34487	0.016912
28	0.35777	0.013379
29	0.37067	0.010424
30	0.38357	0.0080306
31	0.39648	0.0061865
32	0.40938	0.0048812
33	0.42228	0.0041060
34	0.43518	0.0038545
35	0.44808	0.0041218
36	0.46098	0.0049050
37	0.47388	0.0062027
38	0.48678	0.0080152
39	0.49968	0.010344
40	0.51258	0.013194
41	0.52548	0.016569
42	0.53838	0.020478
43	0.55128	0.024929
44	0.56418	0.029933
45	0.57708	0.035504
46	0.58998	0.041659
47	0.60288	0.048416
48	0.61579	0.055799
49	0.62869	0.063833
50	0.64159	0.072549
51	0.65449	0.081985
52	0.66739	0.092182
53	0.68029	0.10319
54	0.69319	0.11508
55	0.70609	0.12791
56	0.71899	0.14177
57	0.73189	0.15679
58	0.74479	0.17309
59	0.75759	0.19071
60	0.76711	0.20483
61	0.77662	0.21971
62	0.78613	0.23524
63	0.79565	0.25133
64	0.80516	0.26791
65	0.81468	0.28492
66	0.82419	0.30232
67	0.83371	0.32006
68	0.84322	0.33812
69	0.85273	0.35647
70	0.86225	0.37509
71	0.87176	0.39394
72	0.88128	0.41303
73	0.89079	0.43232
74	0.90030	0.45180
75	0.90982	0.47147
76	0.91933	0.49130
77	0.92885	0.51130
78	0.93826	0.53123
79	0.93867	0.53225
80	0.93897	0.53331
81	0.93915	0.53439
82	0.93921	0.53549
83	0.93879	0.53836
84	0.93756	0.54099
85	0.93563	0.54316
86	0.93316	0.54468
87	0.93035	0.54543
88	0.92745	0.54534
89	0.92470	0.54442
90	0.92233	0.54274
91	0.92053	0.54046
92	0.90538	0.51508
93	0.89012	0.49148
94	0.87486	0.46955
95	0.85960	0.44909
96	0.84435	0.42991
97	0.82909	0.41190
98	0.81383	0.39494
99	0.79857	0.37895
100	0.78331	0.36386
101	0.76806	0.34960

102	0.75280	0.33613
103	0.73754	0.32339
104	0.72228	0.31135
105	0.70703	0.29999
106	0.69177	0.28927
107	0.67651	0.27916
108	0.66125	0.26964
109	0.64599	0.26071
110	0.63074	0.25233
111	0.61548	0.24451
112	0.60022	0.23721
113	0.58496	0.23045
114	0.56971	0.22420
115	0.55445	0.21845
116	0.53919	0.21322
117	0.52393	0.20849
118	0.50867	0.20425
119	0.49342	0.20051
120	0.47816	0.19727
121	0.46290	0.19452
122	0.44764	0.19228
123	0.43238	0.19054
124	0.41713	0.18931
125	0.40187	0.18860
126	0.38661	0.18841
127	0.37135	0.18875
128	0.35610	0.18964
129	0.34084	0.19109
130	0.32558	0.19311
131	0.31032	0.19572
132	0.29506	0.19895
133	0.27981	0.20281
134	0.26455	0.20734
135	0.24929	0.21257
136	0.23403	0.21852
137	0.21878	0.22526
138	0.20352	0.23282
139	0.18826	0.24127
140	0.17300	0.25067
141	0.17157	0.25157
142	0.17003	0.25247
143	0.16849	0.25330
144	0.16696	0.25406
145	0.16542	0.25476
146	0.16388	0.25540
147	0.16234	0.25597
148	0.16081	0.25649
149	0.15927	0.25694
150	0.15773	0.25733
151	0.15620	0.25767
152	0.15466	0.25794
153	0.15312	0.25814
154	0.15159	0.25829
155	0.15005	0.25837
156	0.14851	0.25838
157	0.14698	0.25832
158	0.14544	0.25820
159	0.14390	0.25799
160	0.14237	0.25771
161	0.14083	0.25734
162	0.13929	0.25687
163	0.13776	0.25631
164	0.13622	0.25565
165	0.13468	0.25486
166	0.13315	0.25393
167	0.13161	0.25285
168	0.13007	0.25158
169	0.12854	0.25008
170	0.12700	0.24830
171	0.12546	0.24612
172	0.12393	0.24334
173	0.12239	0.23944

First rotor, midspan

	x [in]	y[in]
1	0.17979	0.15760
2	0.18048	0.15051
3	0.18117	0.14765
4	0.18186	0.14549
5	0.18255	0.14370
6	0.18325	0.14215
7	0.18394	0.14077
8	0.18463	0.13953
9	0.18532	0.13838
10	0.18588	0.13752
11	0.19747	0.11992
12	0.20907	0.10432
13	0.22066	0.090363
14	0.23226	0.077786
15	0.24386	0.066406
16	0.25546	0.056082
17	0.26706	0.046707
18	0.27866	0.038194
19	0.29026	0.030473
20	0.30186	0.023488
21	0.31346	0.017191
22	0.32506	0.011543
23	0.33667	0.0065094
24	0.34827	0.0020632
25	0.35987	-0.0018200
26	0.37147	-0.0051603
27	0.38308	-0.0079749
28	0.39468	-0.010278
29	0.40628	-0.012082
30	0.41789	-0.013396
31	0.42949	-0.014227
32	0.44109	-0.014583
33	0.45269	-0.014466
34	0.46430	-0.013880
35	0.47590	-0.012825
36	0.48750	-0.011300
37	0.49911	-0.0093034
38	0.51071	-0.0068301
39	0.52231	-0.0038744
40	0.53392	-0.00042857
41	0.54552	0.0035173
42	0.55712	0.0079753
43	0.56873	0.012960
44	0.58033	0.018489
45	0.59193	0.024584
46	0.60353	0.031268
47	0.61514	0.038571
48	0.62674	0.046529
49	0.63834	0.055183
50	0.64995	0.064584
51	0.66155	0.074794
52	0.67315	0.085889
53	0.68476	0.097967
54	0.69636	0.11116
55	0.70796	0.12560
56	0.71956	0.14120
57	0.73117	0.15788
58	0.74277	0.17563
59	0.75428	0.19430
60	0.76284	0.20889
61	0.77140	0.22401
62	0.77996	0.23958
63	0.78851	0.25556
64	0.79707	0.27189
65	0.80563	0.28854
66	0.81418	0.30549
67	0.82274	0.32269
68	0.83130	0.34014
69	0.83986	0.35780
70	0.84841	0.37567
71	0.85697	0.39373
72	0.86553	0.41197
73	0.87408	0.43037
74	0.88264	0.44893
75	0.89120	0.46763
76	0.89975	0.48647
77	0.90831	0.50544
78	0.91677	0.52432
79	0.91715	0.52530
80	0.91742	0.52631
81	0.91759	0.52735
82	0.91764	0.52839
83	0.91722	0.53127
84	0.91598	0.53391
85	0.91403	0.53608
86	0.91154	0.53760
87	0.90871	0.53833
88	0.90578	0.53822
89	0.90301	0.53725
90	0.90061	0.53550
91	0.89881	0.53307
92	0.88521	0.50815
93	0.87153	0.48428
94	0.85784	0.46148
95	0.84416	0.43968
96	0.83047	0.41879
97	0.81679	0.39876
98	0.80310	0.37956
99	0.78942	0.36116
100	0.77573	0.34353
101	0.76205	0.32665
102	0.74836	0.31053
103	0.73468	0.29513
104	0.72099	0.28046

105	0.70731	0.26652
106	0.69362	0.25330
107	0.67994	0.24079
108	0.66625	0.22899
109	0.65257	0.21790
110	0.63888	0.20751
111	0.62520	0.19783
112	0.61151	0.18884
113	0.59783	0.18053
114	0.58414	0.17291
115	0.57046	0.16596
116	0.55677	0.15967
117	0.54309	0.15404
118	0.52940	0.14905
119	0.51572	0.14468
120	0.50204	0.14094
121	0.48835	0.13781
122	0.47467	0.13527
123	0.46098	0.13331
124	0.44730	0.13193
125	0.43361	0.13111
126	0.41993	0.13085
127	0.40624	0.13113
128	0.39256	0.13194
129	0.37887	0.13328
130	0.36519	0.13515
131	0.35151	0.13754
132	0.33782	0.14044
133	0.32414	0.14387
134	0.31045	0.14782
135	0.29677	0.15230
136	0.28309	0.15731
137	0.26941	0.16288
138	0.25572	0.16900
139	0.24204	0.17572
140	0.22836	0.18304
141	0.22703	0.18375
142	0.22559	0.18445
143	0.22416	0.18507
144	0.22273	0.18564
145	0.22130	0.18614
146	0.21987	0.18658
147	0.21844	0.18696
148	0.21701	0.18728
149	0.21558	0.18754
150	0.21415	0.18775
151	0.21271	0.18790
152	0.21128	0.18799
153	0.20985	0.18802
154	0.20842	0.18799
155	0.20699	0.18790
156	0.20556	0.18775
157	0.20413	0.18753
158	0.20270	0.18724
159	0.20126	0.18689
160	0.19983	0.18645
161	0.19840	0.18594
162	0.19697	0.18535
163	0.19554	0.18466
164	0.19411	0.18387
165	0.19268	0.18297
166	0.19124	0.18194
167	0.18981	0.18077
168	0.18838	0.17943
169	0.18695	0.17787
170	0.18552	0.17605
171	0.18409	0.17386
172	0.18265	0.17113
173	0.18122	0.16736

First rotor, tip

	x [in]	y [in]
1	0.23860	0.086311
2	0.23945	0.078986
3	0.24030	0.076022
4	0.24115	0.073796
5	0.24200	0.071961
6	0.24285	0.070380
7	0.24370	0.068984
8	0.24455	0.067731
9	0.24540	0.066594
10	0.24609	0.065741
11	0.25639	0.054062
12	0.26670	0.043481
13	0.27700	0.033867
14	0.28731	0.025118
15	0.29762	0.017155
16	0.30792	0.0099103
17	0.31823	0.0033318
18	0.32853	-0.0026254
19	0.33884	-0.0079985
20	0.34914	-0.012819
21	0.35945	-0.017113
22	0.36975	-0.020902
23	0.38006	-0.024207
24	0.39036	-0.027043
25	0.40067	-0.029424
26	0.41098	-0.031360
27	0.42128	-0.032861
28	0.43159	-0.033935
29	0.44189	-0.034587
30	0.45220	-0.034822
31	0.46250	-0.034641
32	0.47281	-0.034047
33	0.48311	-0.033039
34	0.49342	-0.031615
35	0.50372	-0.029772
36	0.51403	-0.027506
37	0.52434	-0.024810
38	0.53464	-0.021675
39	0.54495	-0.018093
40	0.55525	-0.014051
41	0.56556	-0.0095350
42	0.57586	-0.0045274
43	0.58617	0.00099160
44	0.59647	0.0070458
45	0.60678	0.013663
46	0.61708	0.020877
47	0.62739	0.028727
48	0.63770	0.037260
49	0.64800	0.046534
50	0.65831	0.056619
51	0.66861	0.067602
52	0.67892	0.079595
53	0.68922	0.092741
54	0.69953	0.10724
55	0.70983	0.12330
56	0.72014	0.14063
57	0.73044	0.15898
58	0.74075	0.17816
59	0.75098	0.19790
60	0.75858	0.21295
61	0.76618	0.22830
62	0.77378	0.24392
63	0.78138	0.25979
64	0.78898	0.27588
65	0.79658	0.29217
66	0.80418	0.30866
67	0.81178	0.32532
68	0.81938	0.34215
69	0.82698	0.35913
70	0.83458	0.37626
71	0.84218	0.39353
72	0.84978	0.41092
73	0.85738	0.42844
74	0.86498	0.44607
75	0.87258	0.46381
76	0.88018	0.48165
77	0.88778	0.49959
78	0.89530	0.51744
79	0.89564	0.51837
80	0.89588	0.51933
81	0.89603	0.52032
82	0.89608	0.52131
83	0.89565	0.52421
84	0.89440	0.52685
85	0.89244	0.52903
86	0.88993	0.53054
87	0.88708	0.53126
88	0.88413	0.53112
89	0.88133	0.53011
90	0.87892	0.52829
91	0.87709	0.52569
92	0.86506	0.50124
93	0.85295	0.47709
94	0.84083	0.45343
95	0.82872	0.43028
96	0.81661	0.40767
97	0.80449	0.38564
98	0.79238	0.36419
99	0.78027	0.34338
100	0.76815	0.32321
101	0.75604	0.30373
102	0.74393	0.28494
103	0.73181	0.26689
104	0.71970	0.24960

105	0.70759	0.23308
106	0.69547	0.21736
107	0.68336	0.20245
108	0.67125	0.18837
109	0.65913	0.17513
110	0.64702	0.16274
111	0.63490	0.15119
112	0.62279	0.14051
113	0.61068	0.13067
114	0.59856	0.12168
115	0.58645	0.11352
116	0.57434	0.10618
117	0.56222	0.099647
118	0.55011	0.093900
119	0.53800	0.088917
120	0.52588	0.084676
121	0.51377	0.081152
122	0.50166	0.078319
123	0.48954	0.076149
124	0.47743	0.074617
125	0.46532	0.073693
126	0.45320	0.073351
127	0.44109	0.073563
128	0.42898	0.074301
129	0.41686	0.075540
130	0.40475	0.077254
131	0.39264	0.079418
132	0.38052	0.082008
133	0.36841	0.085002
134	0.35630	0.088377
135	0.34418	0.092112
136	0.33207	0.096189
137	0.31996	0.10059
138	0.30784	0.10529
139	0.29573	0.11028
140	0.28362	0.11554
141	0.28238	0.11607
142	0.28105	0.11656
143	0.27972	0.11698
144	0.27840	0.11735
145	0.27707	0.11765
146	0.27574	0.11789
147	0.27442	0.11808
148	0.27309	0.11821
149	0.27176	0.11829
150	0.27044	0.11831
151	0.26911	0.11828
152	0.26778	0.11819
153	0.26646	0.11804
154	0.26513	0.11784
155	0.26381	0.11758
156	0.26248	0.11726
157	0.26115	0.11688
158	0.25983	0.11644
159	0.25850	0.11593
160	0.25717	0.11536
161	0.25585	0.11471
162	0.25452	0.11398
163	0.25319	0.11316
164	0.25187	0.11225
165	0.25054	0.11124
166	0.24921	0.11011
167	0.24789	0.10885
168	0.24656	0.10743
169	0.24523	0.10582
170	0.24391	0.10396
171	0.24258	0.10177
172	0.24125	0.099068
173	0.23993	0.095429

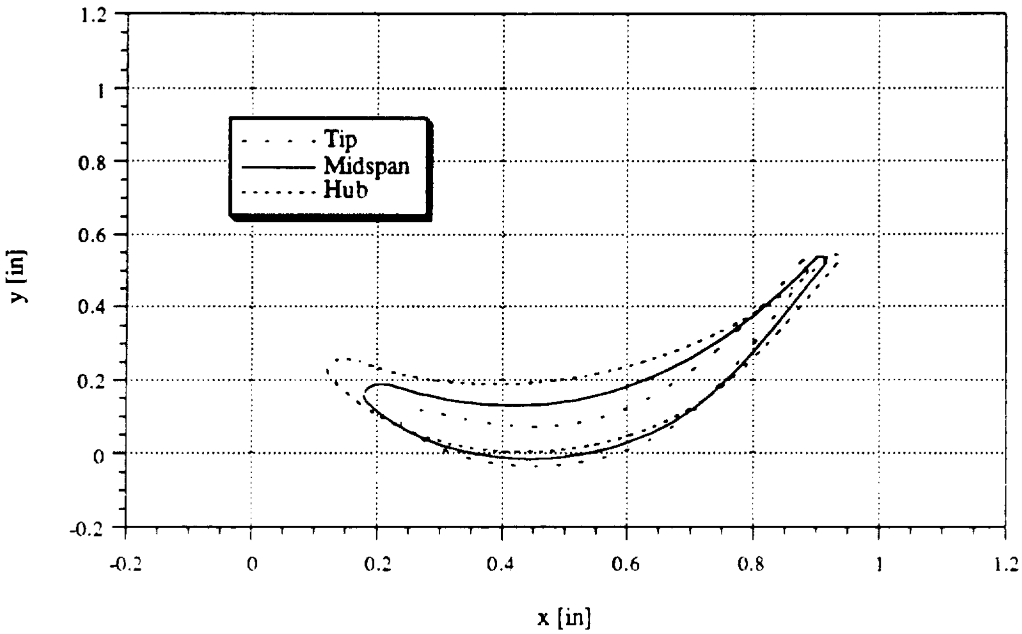

Figure A.1.2--First rotor: tip, midspan, hub.

A.1.3 Second Nozzle Coordinates

Second nozzle, hub

	x [in]	y[in]
1	0.067200	0.71990
2	0.067500	0.71690
3	0.068000	0.71390
4	0.068700	0.71100
5	0.069500	0.70800
6	0.070600	0.70520
7	0.071800	0.70240
8	0.073100	0.69970
9	0.074700	0.69710
10	0.076400	0.69460
11	0.078300	0.69220
12	0.080300	0.68990
13	0.082400	0.68780
14	0.084700	0.68580
15	0.087100	0.68390
16	0.089600	0.68220
17	0.092200	0.68070
18	0.094900	0.67930
19	0.097700	0.67810
20	0.10060	0.67710
21	0.10350	0.67630
22	0.10650	0.67560
23	0.10950	0.67520
24	0.11250	0.67490
25	0.11550	0.67480
26	0.11850	0.67490
27	0.12150	0.67520
28	0.12450	0.67570
29	0.12750	0.67640
30	0.14540	0.68050
31	0.16330	0.68380
32	0.18120	0.68620
33	0.19900	0.68770
34	0.21690	0.68850
35	0.23480	0.68850
36	0.25270	0.68780
37	0.27060	0.68630
38	0.28850	0.68410
39	0.30640	0.68130
40	0.32430	0.67780
41	0.34220	0.67360
42	0.36000	0.66880
43	0.37790	0.66340
44	0.39580	0.65730
45	0.41370	0.65070
46	0.43160	0.64340
47	0.44950	0.63550
48	0.46740	0.62690
49	0.48530	0.61780
50	0.50310	0.60810
51	0.52100	0.59770
52	0.53890	0.58670
53	0.55680	0.57510
54	0.57470	0.56290
55	0.59260	0.55000
56	0.61050	0.53650
57	0.62840	0.52230
58	0.64630	0.50740
59	0.66410	0.49180
60	0.68200	0.47560
61	0.69990	0.45860
62	0.71780	0.44080
63	0.73570	0.42220
64	0.75360	0.40290
65	0.77150	0.38260
66	0.78940	0.36150
67	0.80730	0.33940
68	0.82510	0.31630
69	0.84300	0.29210
70	0.86090	0.26680
71	0.87880	0.24020
72	0.89670	0.21230
73	0.91460	0.18290
74	0.93250	0.15180
75	0.95040	0.11890
76	0.96830	0.083800
77	0.98610	0.046300
78	1.0039	0.0060000
79	1.0046	0.0048000
80	1.0054	0.0036000
81	1.0064	0.0026000
82	1.0075	0.0017000
83	1.0087	0.0010000
84	1.0101	0.00050000
85	1.0115	1.0000e-04
86	1.0129	0.0000
87	1.0143	1.0000e-04
88	1.0157	0.00040000
89	1.0170	0.00080000
90	1.0183	0.0015000
91	1.0194	0.0024000
92	1.0205	0.0034000
93	1.0213	0.0045000
94	1.0220	0.0057000
95	1.0225	0.0071000
96	1.0228	0.0085000
97	1.0229	0.0099000
98	1.0229	0.010300
99	1.0229	0.010600
100	1.0229	0.011000
101	1.0228	0.011400

102	1.0227	0.011800
103	1.0227	0.012100
104	1.0226	0.012500
105	1.0225	0.012800
106	1.0223	0.013200
107	1.0047	0.062800
108	0.98700	0.11240
109	0.96930	0.16200
110	0.95160	0.21160
111	0.93400	0.26120
112	0.91630	0.31070
113	0.89860	0.36030
114	0.88090	0.40990
115	0.86320	0.45950
116	0.85820	0.47360
117	0.85300	0.48760
118	0.84790	0.50150
119	0.84280	0.51510
120	0.83760	0.52840
121	0.83250	0.54140
122	0.82730	0.55420
123	0.82220	0.56680
124	0.81700	0.57900
125	0.81190	0.59100
126	0.80670	0.60260
127	0.80160	0.61400
128	0.79640	0.62500
129	0.79130	0.63580
130	0.77680	0.66370
131	0.76210	0.68850
132	0.74750	0.71090
133	0.73290	0.73110
134	0.71830	0.74950
135	0.70360	0.76640
136	0.68900	0.78200
137	0.67440	0.79630
138	0.65980	0.80960
139	0.64520	0.82190
140	0.63050	0.83320
141	0.61590	0.84370
142	0.60130	0.85340
143	0.58670	0.86230
144	0.57210	0.87050
145	0.55740	0.87800
146	0.54280	0.88480
147	0.52820	0.89100
148	0.51360	0.89660
149	0.49900	0.90150
150	0.48430	0.90580
151	0.46970	0.90960
152	0.45510	0.91280
153	0.44050	0.91540
154	0.42580	0.91740
155	0.41120	0.91880
156	0.39660	0.91970
157	0.38200	0.92000
158	0.36740	0.91970
159	0.35270	0.91890
160	0.33810	0.91740
161	0.32350	0.91540
162	0.30890	0.91270
163	0.29430	0.90930
164	0.27960	0.90530
165	0.26500	0.90060
166	0.25040	0.89520
167	0.23580	0.88910
168	0.22110	0.88210
169	0.20650	0.87430
170	0.19190	0.86560
171	0.17730	0.85590
172	0.16270	0.84520
173	0.14800	0.83320
174	0.13340	0.82000
175	0.11880	0.80520
176	0.10420	0.78880
177	0.089600	0.77030
178	0.074900	0.74920
179	0.073300	0.74660
180	0.071900	0.74380
181	0.070700	0.74100
182	0.069600	0.73810
183	0.068700	0.73520
184	0.068000	0.73220
185	0.067500	0.72910
186	0.067200	0.72610
187	0.067100	0.72300

Second nozzle, midspan

	x [in]	y[in]
1	0.022600	0.81050
2	0.022900	0.80750
3	0.023300	0.80450
4	0.024000	0.80160
5	0.024800	0.79880
6	0.025800	0.79600
7	0.026900	0.79320
8	0.028300	0.79050
9	0.029800	0.78800
10	0.031400	0.78550
11	0.033200	0.78310
12	0.035200	0.78090
13	0.037300	0.77870
14	0.039500	0.77670
15	0.041800	0.77490
16	0.044200	0.77320
17	0.046800	0.77160
18	0.049400	0.77020
19	0.052100	0.76900
20	0.054800	0.76800
21	0.057700	0.76710
22	0.060500	0.76640
23	0.063400	0.76580
24	0.066300	0.76550
25	0.069300	0.76530
26	0.072200	0.76530
27	0.075100	0.76550
28	0.078000	0.76590
29	0.080900	0.76640
30	0.10060	0.77000
31	0.12040	0.77260
32	0.14010	0.77410
33	0.15990	0.77460
34	0.17960	0.77420
35	0.19940	0.77300
36	0.21910	0.77090
37	0.23890	0.76800
38	0.25860	0.76430
39	0.27840	0.75990
40	0.29820	0.75480
41	0.31790	0.74900
42	0.33770	0.74240
43	0.35740	0.73520
44	0.37720	0.72730
45	0.39690	0.71880
46	0.41670	0.70960
47	0.43640	0.69980
48	0.45620	0.68940
49	0.47590	0.67830
50	0.49570	0.66660
51	0.51540	0.65420
52	0.53520	0.64120
53	0.55490	0.62760
54	0.57470	0.61330
55	0.59450	0.59830
56	0.61420	0.58270
57	0.63400	0.56640
58	0.65370	0.54950
59	0.67350	0.53180
60	0.69320	0.51340
61	0.71300	0.49430
62	0.73270	0.47440
63	0.75250	0.45370
64	0.77220	0.43220
65	0.79200	0.40980
66	0.81170	0.38650
67	0.83150	0.36230
68	0.85120	0.33710
69	0.87100	0.31080
70	0.89080	0.28330
71	0.91050	0.25460
72	0.93030	0.22460
73	0.95000	0.19310
74	0.96980	0.15990
75	0.98950	0.12490
76	1.0093	0.087800
77	1.0290	0.048200
78	1.0487	0.0059000
79	1.0493	0.0046000
80	1.0501	0.0035000
81	1.0511	0.0025000
82	1.0522	0.0017000
83	1.0535	0.0010000
84	1.0548	0.00040000
85	1.0562	1.0000e-04
86	1.0576	0.0000
87	1.0590	1.0000e-04
88	1.0604	0.00040000
89	1.0617	0.00090000
90	1.0630	0.0015000
91	1.0641	0.0024000
92	1.0651	0.0034000
93	1.0660	0.0045000
94	1.0667	0.0057000
95	1.0672	0.0071000
96	1.0675	0.0085000
97	1.0676	0.0099000
98	1.0676	0.010300
99	1.0675	0.010700
100	1.0675	0.011100
101	1.0674	0.011500
102	1.0674	0.011900
103	1.0673	0.012400
104	1.0672	0.012800

105	1.0670	0.013100
106	1.0669	0.013500
107	1.0476	0.062100
108	1.0282	0.11070
109	1.0089	0.15930
110	0.98960	0.20780
111	0.97030	0.25640
112	0.95100	0.30500
113	0.93170	0.35350
114	0.91240	0.40210
115	0.89310	0.45070
116	0.88750	0.46450
117	0.88190	0.47850
118	0.87630	0.49230
119	0.87070	0.50610
120	0.86510	0.51970
121	0.85940	0.53320
122	0.85380	0.54660
123	0.84820	0.55980
124	0.84260	0.57290
125	0.83690	0.58570
126	0.83130	0.59830
127	0.82570	0.61070
128	0.82010	0.62290
129	0.81440	0.63480
130	0.79860	0.66660
131	0.78260	0.69630
132	0.76660	0.72370
133	0.75060	0.74880
134	0.73470	0.77190
135	0.71870	0.79310
136	0.70270	0.81280
137	0.68670	0.83110
138	0.67080	0.84800
139	0.65480	0.86380
140	0.63880	0.87850
141	0.62280	0.89210
142	0.60690	0.90480
143	0.59090	0.91660
144	0.57490	0.92760
145	0.55890	0.93770
146	0.54300	0.94700
147	0.52700	0.95560
148	0.51100	0.96340
149	0.49510	0.97050
150	0.47910	0.97680
151	0.46310	0.98250
152	0.44710	0.98750
153	0.43120	0.99180
154	0.41520	0.99540
155	0.39920	0.99840
156	0.38320	1.0007
157	0.36730	1.0023
158	0.35130	1.0033
159	0.33530	1.0036
160	0.31930	1.0032
161	0.30340	1.0021
162	0.28740	1.0002
163	0.27140	0.99770
164	0.25540	0.99440
165	0.23950	0.99030
166	0.22350	0.98540
167	0.20750	0.97970
168	0.19150	0.97310
169	0.17560	0.96560
170	0.15960	0.95710
171	0.14360	0.94750
172	0.12760	0.93690
173	0.11170	0.92500
174	0.095700	0.91180
175	0.079700	0.89710
176	0.063700	0.88070
177	0.047800	0.86240
178	0.031800	0.84180
179	0.029900	0.83900
180	0.028200	0.83610
181	0.026700	0.83310
182	0.025400	0.82990
183	0.024400	0.82670
184	0.023500	0.82350
185	0.023000	0.82020
186	0.022600	0.81680
187	0.022500	0.81350

Second nozzle, tip

	x [in]	y [in]
1	-0.022100	0.90100
2	-0.021800	0.89810
3	-0.021400	0.89520
4	-0.020800	0.89230
5	-0.020000	0.88950
6	-0.019000	0.88670
7	-0.017900	0.88400
8	-0.016600	0.88140
9	-0.015100	0.87880
10	-0.013500	0.87640
11	-0.011800	0.87400
12	-0.0099000	0.87180
13	-0.0079000	0.86970
14	-0.0058000	0.86770
15	-0.0035000	0.86580
16	-0.0012000	0.86410
17	0.0013000	0.86260
18	0.0038000	0.86120
19	0.0064000	0.85990
20	0.0091000	0.85880
21	0.011800	0.85790
22	0.014600	0.85710
23	0.017400	0.85650
24	0.020200	0.85610
25	0.023000	0.85580
26	0.025900	0.85570
27	0.028700	0.85580
28	0.031500	0.85600
29	0.034200	0.85640
30	0.055900	0.85950
31	0.077500	0.86130
32	0.099100	0.86190
33	0.12070	0.86140
34	0.14230	0.85990
35	0.16390	0.85740
36	0.18560	0.85400
37	0.20720	0.84970
38	0.22880	0.84450
39	0.25040	0.83850
40	0.27200	0.83180
41	0.29370	0.82430
42	0.31530	0.81600
43	0.33690	0.80700
44	0.35850	0.79740
45	0.38010	0.78700
46	0.40170	0.77590
47	0.42340	0.76420
48	0.44500	0.75180
49	0.46660	0.73880
50	0.48820	0.72510
51	0.50980	0.71070
52	0.53150	0.69570
53	0.55310	0.68000
54	0.57470	0.66370
55	0.59630	0.64660
56	0.61790	0.62900
57	0.63950	0.61060
58	0.66120	0.59150
59	0.68280	0.57170
60	0.70440	0.55120
61	0.72600	0.53000
62	0.74760	0.50790
63	0.76930	0.48510
64	0.79090	0.46150
65	0.81250	0.43700
66	0.83410	0.41150
67	0.85570	0.38250
68	0.87730	0.35780
69	0.89900	0.32940
70	0.92060	0.29980
71	0.94220	0.26900
72	0.96380	0.23680
73	0.98540	0.20320
74	1.0071	0.16800
75	1.0287	0.13090
76	1.0503	0.091700
77	1.0719	0.050000
78	1.0934	0.0057000
79	1.0941	0.0045000
80	1.0949	0.0034000
81	1.0958	0.0025000
82	1.0970	0.0016000
83	1.0982	0.00090000
84	1.0995	0.00040000
85	1.1009	1.0000e-04
86	1.1023	0.0000
87	1.1037	1.0000e-04
88	1.1051	0.00040000
89	1.1064	0.00090000
90	1.1077	0.0015000
91	1.1088	0.0024000
92	1.1098	0.0034000
93	1.1107	0.0045000
94	1.1113	0.0058000
95	1.1118	0.0071000
96	1.1121	0.0085000
97	1.1122	0.0099000
98	1.1122	0.010300
99	1.1122	0.010800
100	1.1122	0.011200
101	1.1121	0.011700
102	1.1120	0.012100
103	1.1119	0.012600
104	1.1117	0.013000

105	1.1116	0.013400
106	1.1114	0.013900
107	1.0905	0.061400
108	1.0695	0.10900
109	1.0486	0.15650
110	1.0276	0.20410
111	1.0067	0.25170
112	0.98570	0.29920
113	0.96480	0.34680
114	0.94380	0.39430
115	0.92290	0.44190
116	0.91690	0.45550
117	0.91080	0.46940
118	0.90470	0.48320
119	0.89860	0.49720
120	0.89250	0.51110
121	0.88640	0.52500
122	0.88030	0.53900
123	0.87420	0.55300
124	0.86810	0.56690
125	0.86200	0.58060
126	0.85590	0.59420
127	0.84980	0.60760
128	0.84370	0.62080
129	0.83760	0.63380
130	0.82040	0.66970
131	0.80300	0.70410
132	0.78570	0.73660
133	0.76840	0.76660
134	0.75110	0.79430
135	0.73370	0.81990
136	0.71640	0.84370
137	0.69910	0.86580
138	0.68170	0.88650
139	0.66440	0.90570
140	0.64710	0.92380
141	0.62980	0.94060
142	0.61240	0.95630
143	0.59510	0.97100
144	0.57780	0.98470
145	0.56050	0.99740
146	0.54310	1.0092
147	0.52580	1.0201
148	0.50850	1.0302
149	0.49120	1.0394
150	0.47380	1.0478
151	0.45650	1.0554
152	0.43920	1.0622
153	0.42180	1.0682
154	0.40450	1.0735
155	0.38720	1.0780
156	0.36990	1.0817
157	0.35250	1.0847
158	0.33520	1.0869
159	0.31790	1.0883
160	0.30060	1.0889
161	0.28320	1.0888
162	0.26590	1.0878
163	0.24860	1.0860
164	0.23120	1.0834
165	0.21390	1.0799
166	0.19660	1.0756
167	0.17930	1.0703
168	0.16190	1.0641
169	0.14460	1.0568
170	0.12730	1.0486
171	0.11000	1.0392
172	0.092600	1.0286
173	0.075300	1.0168
174	0.058000	1.0036
175	0.040600	0.98890
176	0.023300	0.97260
177	0.0060000	0.95450
178	-0.011300	0.93440
179	-0.013600	0.93150
180	-0.015500	0.92830
181	-0.017300	0.92510
182	-0.018800	0.92180
183	-0.020000	0.91830
184	-0.020900	0.91480
185	-0.021600	0.91120
186	-0.022000	0.90760
187	-0.022200	0.90390

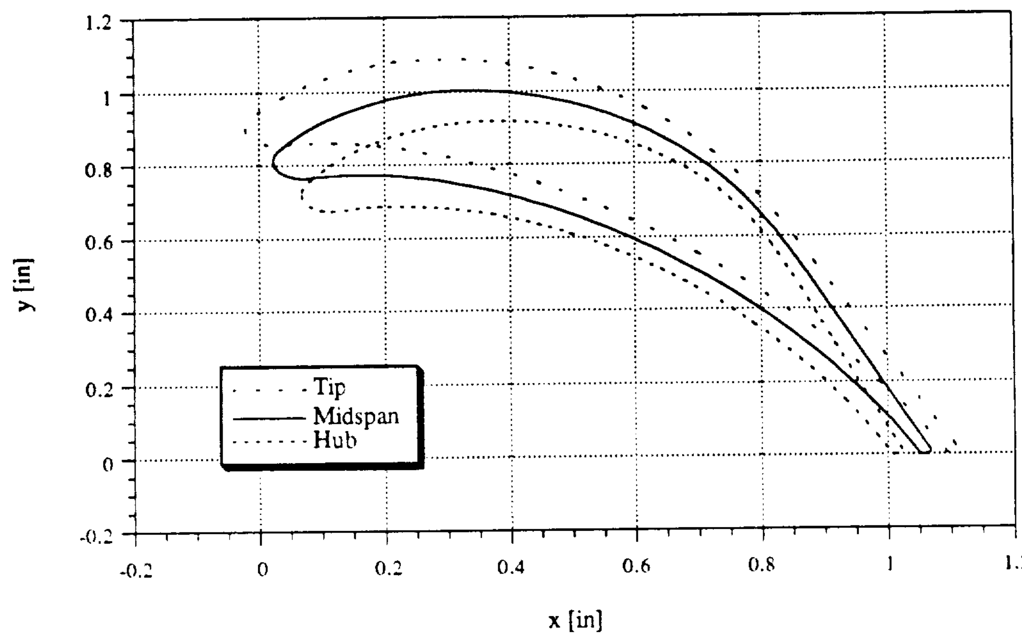

Figure A.1.3--Second nozzle, tip, midspan, hub.

A.2 Listing of Instrumentation Locations

Position No.	Location	Σ ℄/℄	% Wetted Distance
44	Pressure, 90%, S_T = 1.426	0.091	6.38
45	Pressure, 90%, S_T = 1.426	0.173	12.13
46	Pressure, 90%, S_T = 1.426	0.543	38.08
47	Pressure, 90%, S_T = 1.426	0.872	61.15
48	Pressure, 90%, S_T = 1.426	1.096	76.86
80	Pressure, 50%, S_T = 1.386	0	0
81	Pressure, 50%, S_T = 1.386	0.0385	2.78
49	Pressure, 50%, S_T = 1.386	0.070	5.05
82	Pressure, 50%, S_T = 1.386	0.123	8.87
50	Pressure, 50%, S_T = 1.386	0.125	9.02
83	Pressure, 50%, S_T = 1.386	0.173	12.48
84	Pressure, 50%, S_T = 1.386	0.244	17.61
85	Pressure, 50%, S_T = 1.386	0.3235	23.34
51	Pressure, 50%, S_T = 1.386	0.477	34.42
52	Pressure, 50%, S_T = 1.386	0.821	59.24
53	Pressure, 50%, S_T = 1.386	1.048	75.61
54	Pressure, 50%, S_T = 1.386	1.119	85.86
55	Pressure, 23%, S_T = 1.374	1.244	90.54
56	Pressure, 10%, S_T = 1.282	0.084	6.55
57	Pressure, 10%, S_T = 1.282	0.164	12.79
58	Pressure, 10%, S_T = 1.282	0.496	38.69
59	Pressure, 10%, S_T = 1.282	0.802	62.56
60	Pressure, 10%, S_T = 1.282	1.047	81.67
61	Pressure, 10%, S_T = 1.282	1.169	91.19

Table A.2.1--Heat flux instrumentation, first stage nozzle guide vane, pressure side.

Position No.	Location	Σ £/£	% Wetted Distance
62	Suction, 90%, S_T = 1.726	0.095	5.50
63	Suction, 90%, S_T = 1.726	0.376	21.78
64	Suction, 90%, S_T = 1.726	0.809	46.87
65	Suction, 90%, S_T = 1.726	1.127	65.30
66	Suction, 90%, S_T = 1.726	1.435	83.20
80	Suction, 50%, S_T = 1.706	0.000	0
86	Suction, 50%, S_T = 1.706	0.0585	3.43
67	Suction, 50%, S_T = 1.706	0.060	3.52
87	Suction, 50%, S_T = 1.706	0.1385	8.12
88	Suction, 50%, S_T = 1.706	0.215	12.60
89	Suction, 50%, S_T = 1.706	0.285	16.71
90	Suction, 50%, S_T = 1.706	0.363	21.28
68	Suction, 50%, S_T = 1.706	0.381	22.33
69	Suction, 50%, S_T = 1.706	0.603	35.35
70	Suction, 50%, S_T = 1.706	0.857	50.23
71	Suction, 50%, S_T = 1.706	1.090	63.89
72	Suction, 50%, S_T = 1.706	1.385	81.18
73	Suction, 31%, S_T = 1.685	1.579	93.71
74	Suction, 19%, S_T = 1.609	1.489	92.54
75	Suction, 10%, S_T = 1.580	0.085	5.38
76	Suction, 10%, S_T = 1.580	0.367	23.23
77	Suction, 10%, S_T = 1.580	0.567	35.87
78	Suction, 10%, S_T = 1.580	1.177	74.49
79	Suction, 10%, S_T = 1.580	1.357	85.89

Table A.2.2--Heat flux instrumenatation, first stage nozzle guide vane, suction side.

Position No.	Location	Σ £/£	% Wetted Distance
33	Tip, S_T = 0.985	0.1665	16.9
34	Tip, S_T = 0.985	0.379	38.48
35	Tip, S_T = 0.985	0.563	57.16
36	Tip, S_T = 0.985	0.702	71.27
12	Suction, 90%, S_T = 1.101	0.075	6.81
13	Suction, 90%, S_T = 1.101	0.509	46.23
37	Suction, 90%, S_T = 1.101	0.632	57.40
38	Suction, 90%, S_T = 1.101	0.767	69.66
14	Suction, 90%, S_T = 1.101	0.900	81.74
39	Suction, 90%, S_T = 1.101	0.991	90.01
1	Pressure, 90%, S_T = 0.898	0.043	4.79
2	Pressure, 90%, S_T = 0.898	0.406	45.21
3	Pressure, 90%, S_T = 0.898	0.561	62.47
20	Suction, 10%, S_T = 1.232	0.090	7.31
21	Suction, 10%, S_T = 1.232	0.198	16.07
22	Suction, 10%, S_T = 1.232	0.636	51.62
23	Suction, 10%, S_T = 1.232	0.988	80.19
9	Pressure, 10%, S_T = 0.955	0.052	5.45
10	Pressure, 10%, S_T = 0.955	0.464	48.59
11	Pressure, 10%, S_T = 0.955	0.622	65.13

Table A.2.3a--Heat flux instrumentation, first stage rotor.

Position No.	Location	Σ £/£	% Wetted Distance
24	Platform	0.222	22.05
25	Platform	0.595	59.09
26	Suction 50%, S_T = 1.158	0	0
30	Suction 50%, S_T = 1.158	0.067	5.79
31	Suction 50%, S_T = 1.158	0.137	11.83
32	Suction 50%, S_T = 1.158	0.205	17.71
15	Suction 50%, S_T = 1.158	0.330	28.51
16	Suction 50%, S_T = 1.158	0.560	48.38
17	Suction 50%, S_T = 1.158	0.742	64.10
18	Suction 50%, S_T = 1.158	0.949	81.99
19	Suction 50%, S_T = 1.158	1.074	92.79
27	Pressure, 50%, S_T = 0.919	0.080	8.71
28	Pressure, 50%, S_T = 0.919	0.148	16.10
29	Pressure, 50%, S_T = 0.919	0.201	21.87
4	Pressure, 50%, S_T = 0.919	0.217	23.61
5	Pressure, 50%, S_T = 0.919	0.409	44.50
6	Pressure, 50%, S_T = 0.919	0.556	60.50
7	Pressure, 50%, S_T = 0.919	0.669	72.80
8	Pressure, 50%, S_T = 0.919	0.806	87.70

Table A.2.3b--Heat flux instrumentation, first stage rotor (cont'd).

Position No.	Location	Σ £/£	% Wetted Distance
91	Pressure, 50%, S_T = 1.392	0.016	1.15
92	Pressure, 50%, S_T = 1.392	0.101	7.26
93	Pressure, 50%, S_T = 1.392	0.168	12.07
94	Pressure, 50%, S_T = 1.392	0.514	36.93
95	Pressure, 50%, S_T = 1.392	0.707	50.79
96	Pressure, 50%, S_T = 1.392	0.855	61.42
97	Pressure, 50%, S_T = 1.392	1.071	76.94
98	Suction, 50%, S_T = 1.729	0.00	0
99	Suction, 50%, S_T = 1.729	0.137	7.92
100	Suction, 50%, S_T = 1.729	0.375	21.69
101	Suction, 50%, S_T = 1.729	0.545	31.52
102	Suction, 50%, S_T = 1.729	0.893	51.65
103	Suction, 50%, S_T = 1.729	0.975	56.39
104	Suction, 50%, S_T = 1.729	1.155	66.80
105	Suction, 50%, S_T = 1.729	1.302	75.30
106	Suction, 50%, S_T = 1.729	1.369	79.18
107	Suction, 50%, S_T = 1.729	1.546	89.42

Table A.2.3c--Heat flux instrumentation, first stage rotor (cont'd).

Position No.	Location	$\Sigma \mathcal{L}/\mathcal{L}$	% Wetted Distance
P1	Pressure, 90%, S_T = 0.891	0.044	4.94
P2	Pressure, 90%, S_T = 0.891	0.403	45.23
P3	Pressure, 90%, S_T = 0.891	0.563	63.19
P4	Suction, 90%, S_T = 1.125	0.068	6.00
P5	Suction, 90%, S_T = 1.125	0.187	16.62
P6	Suction, 90%, S_T = 1.125	0.875	77.78
P7	Pressure, 50%, S_T = 0.921	0.040	4.34
P8	Pressure, 50%, S_T = 0.921	0.125	13.57
P9	Pressure, 50%, S_T = 0.921	0.402	43.65
P10	Pressure, 50%, S_T = 0.921	0.670	72.75
P11	Suction, 50%, S_T = 1.165	0.065	5.54
P12	Suction, 50%, S_T = 1.165	0.141	12.06
P13	Suction, 50%, S_T = 1.165	0.214	18.37
P14	Suction, 50%, S_T = 1.165	0.296	25.41
P15	Suction, 50%, S_T = 1.165	0.534	45.84
P16	Suction, 50%, S_T = 1.165	0.702	60.26
P17	Suction, 50%, S_T = 1.165	0.925	79.40

Table A.2.4a--Pressure Instrumentation, first stage rotor.

P18	Pressure, 10%, S_T = 0.948	0.047	4.96
P19	Pressure, 10%, S_T = 0.948	0.445	46.94
P20	Pressure, 10%, S_T = 0.948	0.593	62.55
P21	Suction, 10%, S_T = 1.215	0.083	6.83
P22	Suction, 10%, S_T = 1.215	0.231	19.01
P23	Suction, 10%, S_T = 1.215	0.594	48.89
P24	Suction, 10%, S_T = 1.215	0.896	73.74

Table A.2.4b--Pressure Instrumentation, first stage rotor (cont'd).

Position No.	Location	Σ £/£	% Wetted Distance
P25	Pressure, 90%, S_T = 1.433	0.068	4.75
P26	Pressure, 90%, S_T = 1.433	0.528	36.85
P30	Pressure, 90%, S_T = 1.433	1.064	74.25
P33	Pressure, 50%, S_T = 1.425	0.108	7.58
P34	Pressure, 50%, S_T = 1.425	0.218	15.30
P35	Pressure, 50%, S_T = 1.425	0.518	36.35
P36	Pressure, 50%, S_T = 1.425	0.860	60.35
P37	Pressure, 50%, S_T = 1.425	1.031	72.35
P45	Pressure, 10%, S_T = 1.241	0.061	4.92
P46	Pressure, 10%, S_T = 1.241	0.480	38.68
P47	Pressure, 10%, S_T = 1.241	1.023	82.43

Table A.2.5a--Pressure Instrumentation, first stage vane.

Position No.	Location	Σ £/£	% Wetted Distance
P28	Suction, 90%, S_T = 1.662	0.100	6.02
P29	Suction, 90%, S_T = 1.662	0.367	22.08
P30	Suction, 90%, S_T = 1.662	0.775	46.63
P31	Suction, 90%, S_T = 1.662	1.088	65.46
P32	Suction, 90%, S_T = 1.662	1.359	81.77
P38	Suction, 50%, S_T = 1.728	0.114	6.60
P39	Suction, 50%, S_T = 1.728	0.252	14.58
P40	Suction, 50%, S_T = 1.728	0.400	23.15
P41	Suction, 50%, S_T = 1.728	0.592	34.26
P42	Suction, 50%, S_T = 1.728	0.847	49.02
P43	Suction, 50%, S_T = 1.728	1.108	64.12
P44	Suction, 50%, S_T = 1.728	1.491	86.28
P48	Suction, 10%, S_T = 1.568	0.091	5.80
P49	Suction, 10%, S_T = 1.568	0.354	22.58
P50	Suction, 10%, S_T = 1.568	0.563	35.91
P51	Suction, 10%, S_T = 1.568	1.148	73.21
P52	Suction, 10%, S_T = 1.568	1.333	85.01

Table A.2.5b--Pressure Instrumentation, first stage vane (cont'd).

Position No.	Location
P53	Hub wall, near midpassage, 0.062 aft of leading edge
P54	Hub wall, 0.145 from suction surface, 0.062 aft of leading edge
P55	Hub wall, 0.604 from leading edge, near pressure surface of vane #1
P56	Hub wall, 0.575 from leading edge, near pressure surface of vane #7
P57	Hub wall, 0.086 from trailing edge, near pressure surface of vane #7 (in region where vane trailing edge has been removed

Table A.2.5c--Pressure Instrumentation, first stage vane (cont'd).

A.3 Listing of Data: Pressure and Stanton numbers

% wetted distance	Run 5	Run 6	Run 7	Run 8	Run 11	Run 12	Run 13
-82.4	0.88276	0.86732	0.90313	0.91504	0.90972	0.82652	0.79142
-38.7	1.0000	1.0000	0.94244	0.96289	1.0049	1.0000	1.0000
-4.9000	0.96158	0.92878	0.99996	1.0000	1.0000	0.95414	0.94347
5.8000	0.95961	0.93366	0.98175	0.99316	0.98234	0.93519	0.93470
22.600	0.91330	0.88780	0.93381	0.94922	0.93719	0.90828	0.89376
73.200	0.78621	0.77951	0.86190	0.87598	0.85672	0.74576	0.78070
85.000	0.77438	0.74829	0.77274	0.78320	0.79293	0.75972	0.77778

Table A.3.1--Pressure ratio distribution, first vane, 10% span. % wetted distances less than zero are on pressure surface, % wetted distances greater than zero are on suction surface.

% wetted distance	Run 5	Run 6	Run 7	Run 8	Run 11	Run 12	Run 13
-72.400	0.86831	0.83445	0.89595	0.89234	0.88943	0.85020	0.84981
-60.400	0.85767	0.83254	0.85645	0.87585	0.87378	0.83929	0.83624
-36.400	0.99996	1.0000	1.0000	1.0000	1.0000	1.0000	1.0000
-15.300	0.99319	0.96172	0.98844	1.0000	0.99804	0.98611	0.99031
-7.6000	0.95931	0.93971	0.94798	0.94277	0.94423		
34.300							
64.100	0.77442	0.76364	0.75723	0.76431	0.77397	0.75099	0.78488
74.700	0.81410	0.85742	0.79094	0.80213	0.83659	0.79663	0.85659

Table A.3.2--Pressure ratio distribution, first vane, 50% span. % wetted distances less than zero are on pressure surface, % wetted distances greater than zero are on suction surface.

% wetted distance	Run 5	Run 6	Run 7	Run 8	Run 11	Run 12	Run 13
-36.800	1.0000	1.0000	0.99998	1.0000	1.0000		
-4.7000	0.89197	0.85129	0.93754	0.92958	0.91932	0.93100	0.83100
6.0000	0.86042	0.74738		0.88826	0.87242	0.68900	0.70700
22.100	0.72753	0.72164	0.74183	0.73709	0.72889	0.74900	0.76500
46.600	0.62141	0.62726	0.60763	0.61502	0.62101	0.64200	0.68600
65.500	0.78967	0.78646	0.76420	0.76526	0.77205	0.77000	
81.800	0.97514	0.89609	0.99718	0.99624	0.98030		

Table A.3.3--Pressure ratio distribution, first vane, 90% span. % wetted distances less than zero are on pressure surface, % wetted distances greater than zero are on suction surface.

% wetted distance	Run 5	Run 6	Run 7	Run 8	Run 11	Run 12	Run 13
-62.600	0.91500	0.89200	0.75936	0.82600	0.83500	0.79187	0.82190
-46.900	0.91000	0.93600		0.97700	0.95800	0.92170	0.90000
-5.0000					0.97900	0.99823	0.99978
6.8000	0.98300	0.95300	1.00103	0.97000	0.96500	0.87711	0.90190
19.000	0.81900	0.82500	0.72097	0.78800	0.80000	0.74628	0.77429
48.900	0.81100	0.81200	0.77809	0.83600	0.83000	0.78989	0.77714

Table A.3.4--Pressure ratio distribution, first blade, 10% span. % wetted distances less than zero are on pressure surface, % wetted distances greater than zero are on suction surface.

% wetted distance	Run 5	Run 6	Run 7	Run 8	Run 11	Run 12	Run 13
-72.700	0.83400	0.88400	0.90100	0.89000	0.89900	0.86200	0.88500
-13.600	0.83200	0.85100		0.73400	0.76500	0.87200	0.79600
5.6000	0.72000	0.74000	0.70000	0.70200	0.71300		
12.100	0.81800	0.82500	0.89800	0.90700	0.91800	0.81900	0.84500
18.400	0.76000	0.78500	0.71100	0.68100	0.67400	0.75200	0.70900
25.400	0.79600	0.81800	0.79200	0.79100	0.76800	0.80700	0.76300
45.800	0.78300	0.77900	0.79200	0.79100	0.79700	0.76700	0.77800
60.300	0.67200	0.70300	0.63200	0.68600	0.71700	0.69000	0.72200
79.400	0.79000	0.80800	0.77400	0.82000	0.82500	0.77600	0.79500

Table A.3.5--Pressure ratio distribution, first blade, 50% span. % wetted distances less than zero are on pressure surface, % wetted distances greater than zero are on suction surface.

% wetted distance	Run 5	Run 6	Run 7	Run 8	Run 11	Run 12	Run 13
-45.200	0.91200						
-4.9000	0.89400	0.86700	0.90700	0.88200	0.88500	0.87600	0.88100
6.0000	0.91700	0.96700	0.85700	0.87600	0.91100	0.84100	0.87900
16.600	0.80500	0.82300	0.77400	0.77500	0.79900	0.75700	0.78600
77.800	0.80300	0.79400	0.75200	0.78900	0.85300	0.72700	0.75400

Table A.3.6--Pressure ratio distribution, first blade, 90% span. % wetted distances less than zero are on pressure surface, % wetted distances greater than zero are on suction surface.

% wetted distance	Run 1	Run 5	Run 6	Run 7	Run 8	Run 11	Run 12	Run 13
-91.190	0.013191	0.015026	0.015452	0.013966	0.014661	0.016170	0.015130	0.014617
-81.670			0.022809	0.025479	0.025560	0.027150	0.023096	0.021765
-62.560	0.0079545	0.0082174	0.0083739	0.0084706	0.0087706	0.0092800	0.0086087	0.0079565
-38.690	0.0055909	0.0040957	0.0040435	0.0063529	0.0064862	0.0068700	0.0039043	0.0035913
-12.790	0.0070364	0.0058348	0.0057652	0.0069832	0.0073486	0.0073000	0.0057043	0.0053565
-6.5500	0.0088909	0.0070870	0.0070870	0.0079160	0.0082569	0.0082500	0.0072000	0.0068783
5.3800	0.0075000	0.0067043	0.0066957	0.0077983	0.0076147	0.0079500	0.0058870	0.0056783
23.230								
35.870	0.010964	0.011009	0.010870	0.010866	0.010798	0.011440	0.010800	0.0093739
74.490	0.0060455	0.0056522	0.0058435	0.0052941	0.0050550	0.0051300	0.0058000	0.0056609
85.890	0.0063000	0.0058870	0.0059913	0.0056050	0.0055229	0.0056800	0.0060609	0.0057565

Table A.3.7--Stanton number distribution, first vane, 10% span. % wetted distances less than zero are on pressure surface, % wetted distances greater than zero are on suction surface.

% wetted distance	Run 1	Run 5	Run 6	Run 7	Run 8	Run 11	Run 12	Run 13
-75.610	0.010036	0.010365	0.010522	0.0096639	0.010037	0.010320	0.010200	0.010252
-59.240	0.0095000	0.0088522	0.0091304	0.0093697	0.0096789	0.010020	0.0090087	0.0088348
-34.420	0.0061182	0.0050174	0.0054000	0.0054622	0.0059725	0.0063300	0.0049304	0.0044348
-23.020		0.0032087	0.0032696	0.0052941	0.0056239	0.0057500	0.0035304	0.0035826
-17.360		0.0036522	0.0038609	0.0055210	0.0058073	0.0061600	0.0039478	0.0039304
-12.300	0.0054545	0.0041652	0.0041565	0.0056555	0.0058624	0.0063000	0.0042957	0.0042696
-9.0200	0.0081182	0.0078870	0.0076696	0.0076975	0.0080092	0.0081100	0.0068870	0.0063130
-8.7500	0.0054636	0.0047478	0.0047391	0.0050420	0.0059174	0.0063300	0.0048174	0.0048348
-5.0500	0.0099091	0.0067565	0.0068870	0.0086555	0.0085780	0.0089400	0.0068087	0.0064261
-2.7400	0.0076636	0.0099739	0.0098783	0.0097647	0.010385	0.010960	0.010078	0.0100000
0.0000		0.014504	0.014522					
3.4100	0.0086273	0.0097826	0.0097652	0.0092773	0.010780	0.0091400	0.010217	0.010191
3.5200	0.0092818	0.0091391	0.0092087	0.0090336	0.0092661		0.0093739	0.0087826
8.0700	0.0057818	0.0057913	0.0057043	0.0058235	0.0068440	0.0065700	0.0059217	0.0059217
12.520	0.0053909	0.0042870	0.0042435	0.0055462	0.0060826	0.0063300	0.0043913	0.0043652
16.600		0.0036522	0.0041130	0.0067143	0.0070917	0.0075300	0.0043130	0.0042696
22.330	0.010345	0.0070435	0.0068348	0.010151	0.010275	0.010620	0.0077913	
35.350	0.0084727	0.0070435	0.0072348	0.0082941	0.0089633	0.0089500	0.0075304	0.0068174
50.230	0.0088273	0.0096000	0.0098174	0.0082017	0.0087156	0.0088200	0.0098435	0.0097217
63.890	0.0080727	0.0085217	0.0086696	0.0076134	0.0082018	0.0083600	0.0089565	0.0088696
81.180	0.0078091	0.0084609	0.0086957	0.0074538	0.0080459	0.0083100	0.0087826	0.0086609

Table A.3.8--Stanton number distribution, first vane, 50% span. % wetted distances less than zero are on pressure surface, % wetted distances greater than zero are on suction surface.

% wetted distance	Run 1	Run 5	Run 6	Run 7	Run 8	Run 11	Run 12	Run 13
-76.860	0.0081364	0.0082087	0.0084957	0.0093277	0.0088991	0.0080100	0.0085739	0.0085130
-61.150	0.0092545	0.0086435	0.0088783	0.0094958	0.010303	0.0083200	0.0096435	0.0089652
-38.080	0.0070545	0.0056087	0.0058696	0.0073445	0.0071101	0.0063900	0.0061913	0.0060435
-12.130	0.0076909	0.0048870	0.0039304	0.0056723	0.0059083	0.0055500	0.0055304	0.0050435
-6.3800	0.010009	0.0055565	0.0058174	0.0075882	0.0081284	0.0077900	0.0075391	0.0059217
5.5000	0.0090727	0.0075826	0.0081478	0.0091933	0.0098440	0.010710	0.0080783	0.0078783
21.780		0.0079565	0.0081217	0.0096975	0.010009	0.010340	0.0092261	0.0085043
46.870	0.0060000	0.0062087	0.0062696	0.0054706	0.0054954	0.0061600	0.0061565	0.0059391
65.300	0.0054545	0.0046522	0.0048696	0.0048487	0.0049817	0.0074000	0.0048609	0.0030174
83.200	0.0073909	0.0062522	0.0061739	0.0063361	0.0070367	0.0079000	0.0073739	0.0044522

Table A.3.9--Stanton number distribution, first vane, 90% span. % wetted distances less than zero are on pressure surface, % wetted distances greater than zero are on suction surface.

% wetted distance	Run 1	Run 5	Run 6	Run 7	Run 8	Run 11	Run 12	Run 13
-65.130	0.0071273	0.0068261	0.0071739	0.0091597	0.011275	0.0069300	0.0069652	0.0067391
-48.590	0.0066455	0.0060522	0.0065913	0.0067815	0.0071376	0.0066600	0.0063304	0.0058870
-5.4500	0.010309	0.0089739	0.0098870	0.010588	0.011028	0.0090900	0.0099913	0.0089826
7.3100	0.010482	0.0053304	0.0046870	0.0035882	0.0044128	0.0048500	0.0041304	0.0036696
16.070	0.0074091	0.0050870	0.0046000	0.0035714	0.0047431	0.0047400	0.0052783	0.0051739
51.620		0.0065652	0.0064348	0.0072353	0.0077064	0.0070000	0.0065913	0.0064261
80.170	0.0068727	0.0069391	0.0063130	0.0066387	0.0067982	0.0060300	0.0069478	0.0067043

Table A.3.10--Stanton number distribution, first blade, 10% span. % wetted distances less than zero are on pressure surface, % wetted distances greater than zero are on suction surface.

% wetted distance	Run 1	Run 5	Run 6	Run 7	Run 8	Run 11	Run 12	Run 13
-87.700	0.0076000	0.0077739	0.0079739	0.0081008	0.0087431	0.0078200	0.0080957	0.0079652
-72.800	0.0075455	0.0068348	0.0070087	0.0071513	0.0076514	0.0067000	0.0070435	0.0067652
-60.500	0.0070455	0.0066174	0.0066348	0.0071092	0.0076697	0.0068300	0.0067043	0.0065217
-44.500	0.0056727	0.0052522	0.0051652	0.0056471	0.0058440	0.0051700	0.0052783	0.0051391
-23.610	0.0059000	0.0055478	0.0058609	0.0059580	0.0058899	0.0053900	0.0058087	0.0055217
-21.870	0.0060364	0.0053217	0.0055043	0.0059832	0.0062202	0.0057100	0.0054261	0.0054261
-20.200	0.0064182	0.0056435	0.0057043	0.0057059	0.0061284	0.0054600	0.0057652	0.0058957
-16.100	0.0062182	0.0051826	0.0059304	0.0061345	0.0064679	0.0062100	0.0053739	0.0055391
-12.300	0.0087909	0.0048000	0.0052087				0.0080348	0.0045739
-8.7100	0.0065909	0.0051217	0.0050522	0.0055378	0.0058349	0.0056100	0.0053043	0.0050609
0.0000	0.015782	0.016539	0.016365	0.014429	0.015321	0.013980	0.016800	0.016478
5.7000	0.0061545	0.0053565	0.0053739	0.0070420	0.0084954	0.0073300	0.0069217	0.0060957
11.830	0.010255	0.0037478	0.0028522	0.0040504	0.0049541	0.0055900	0.0060348	0.0059652
15.000	0.0080182							
17.710	0.0080364	0.0065130	0.0057478	0.0065378	0.0072936	0.0072700	0.0088870	0.0088870
24.200	0.0065455							
28.510	0.0054636	0.0078957	0.0080522	0.0073109	0.0074587	0.0071800	0.0078174	0.0076609
48.380	0.0087273	0.0072957	0.0072870	0.0066471	0.0071009	0.0066600	0.0072522	0.0070870
64.100	0.0062182	0.0056435	0.0056609	0.0052689	0.0056422	0.0052900	0.0058870	0.0057652
81.990	0.0054091	0.0049130	0.0050522	0.0045882	0.0048624	0.0044600	0.0052000	0.0049826
92.790	0.0053273	0.0047652	0.0048348	0.0045546	0.0047431	0.0044500	0.0050870	0.0048261

Table A.3.11--Stanton number distribution, first blade, 50% span. % wetted distances less than zero are on pressure surface, % wetted distances greater than zero are on suction surface.

% wetted distance	Run 1	Run 5	Run 6	Run 7	Run 8	Run 11	Run 12	Run 13
-62.470	0.0073455	0.0066696	0.0065217	0.0070084	0.0075413	0.0062500	0.0066348	0.0064087
-40.420		0.0053913	0.0054174	0.0055294	0.0058165	0.0050300	0.0054522	0.0054087
-4.7900	0.0099545	0.0086522	0.0085391		0.0085505	0.0074300	0.0086174	0.0084783
6.8100	0.0077818	0.0093478	0.0090609	0.0098151	0.010606	0.0085800	0.0083391	0.0079826
46.230	0.0084364	0.0080087	0.0077391	0.0082017	0.0086147	0.0070200	0.0080348	0.0076000
57.400	0.0074545							
69.660	0.010464							
81.740	0.0088545	0.0098783	0.0098783	0.0094118	0.0099358	0.0088400	0.010017	0.0098609
90.010	0.0079000	0.0080696	0.0081913	0.0076891	0.0081743	0.0071200	0.0085391	0.0081913

Table A.3.12--Stanton number distribution, first blade, 90% span. % wetted distances less than zero are on pressure surface, % wetted distances greater than zero are on suction surface.